SAPIENZA
UNIVERSITÀ DI ROMA

Development of a prototype for ET-LF's cryostat: model and tests of heat links

Faculty of Mathematical, Physical, and Natural Sciences
Physics

Marco Ricci
ID number 1812406

Advisor
Prof. E. Majorana

Co-Advisor
Prof. A. Cruciani

Academic Year 2021/2022

Thesis not yet defended

This thesis has been typeset by LaTeX and the Sapthesis class.

Author's email: ricci.1812406@studenti.uniroma1.it

To my family
and to Maria

Abstract

Gravitational Waves (GWs) are ripples of space-time caused by high mass accelerating objects with a certain degree of asymmetry. After the first observations of GWs, multi-messenger astronomy became one of the most powerful instruments to go deeper into the understanding of the Universe. This motivated further efforts to enhance the detectors' sensitivity.

Einstein Telescope (ET) is a next-generation GWs observatory characterized by an enhancement in the sensitivity and frequency range for observations. The thesis will focus on one of the two Michelson interferometers that will compose ET: the cryogenic one, designed to have optimal operation at low frequencies.

Finite element thermal simulations on the first prototype of the cooling line of the mirrors for such interferometer need to be performed before real tests. Simulations are useful to understand the asymptotic limits of the temperature of the model with respect to all its different parts. Particular attention will be paid to the heat links, connections located throughout the cooling line useful to reduce vibrations while efficiently transferring heat. Two different types of simulations can be performed with ANSYS Mechanical: steady-state and transient simulations. The former are useful to study the equilibrium temperature while the latter the variation with time of the temperature gradient.

At last, experimental measurement of thermal conductivity of high purity material (Al 6N) is presented. Residual Resistivity Ratio (RRR) measurement is performed, this can be used to obtain the thermal conductivity through the Wiedemann-Franz law that holds in the low-temperature region. A value of $RRR = 1427.8 \pm 18.4$ at $16.69K$ is obtained, this correspond to a thermal conductivity of $18216 \pm 235 W/m/K$, in good agreement with the value in literature.

Acknowledgements

First of all, I would like to thank my supervisor Professor E. Majorana, he gave me the opportunity to work with the Virgo group at Sapienza University, and my co-advisor A. Cruciani. They supported and helped me in my thesis work both in the simulation activities and experimental ones, always giving me advice and new ideas for the thesis.

I want to thank all the members and researchers of the Virgo group, they always helped me whenever possible with kindness.

I would like to express my gratitude to all the people who helped me in the experimental measurement, without which I would not have been able to complete my activity. First of all, I want to thank A. Girardi for helping me in the design and manufacturing of the electrical components and G. Amico for the manufacturing of the mechanical parts of the experimental setup. Then, I would like to thank A. Rezaei for the help in the comprehension of the basics of technical drawing. Last but not least, I want to thank S. Pirro for all the help and advice he gave me in the laboratory work.

On a personal front, I would like to express my sincere gratitude to my family for their support in the everyday life. I want to thank all my university colleagues for the years spent together; I shared anxieties and successes with them. Last but not least, I want to thank my girlfriend Maria for always being by my side. I would like to thank her for the support received in the past years but, especially, I want to thank her to believe in me when neither I do.

Contents

Introduction

After the first observations of Gravitational Waves (GWs), multi-messenger astronomy became one of the most powerful instruments to go deeper into the comprehension of physics in all of its branches. Better GWs observations are, then, indispensable for this purpose.

Nowadays, different GWs observatories are operating, each with particular features that allow better observations. The challenge in the next years is the design of new generation GWs observatories that will enhance the frequency and sensitivity range for the detection. Einstein Telescope (ET) is a proposed underground infrastructure that will host a third-generation GW observatory. ET, such as the existing observatories, will be based upon the typical Michelson interferometer (with Fabry-Pérot (FP) cavities) but its innovative triangular shape, in which the interferometers will have the arms at $60°$ one from the other, will allow ET to observe both the possible GWs' polarizations ($+$ and $\times$) at the same time. The enhancement in the frequency range for observations will be guaranteed by the combination of two interferometers, located at each vertex of the triangle: one that will work at room temperature, optimized for high frequencies, and the other at cryogenic temperature, optimized for low frequencies.

The thesis is based on the cryogenic interferometers of ET. The mirrors in such types of interferometers need to be cooled to $10 - 15K$ and typical mechanical cryocoolers can be used for this purpose. Vibrations coming from the refrigeration cycles cannot reach the mirrors because they would prevent GWs' observations. A cooling line can, then, be designed to locate the cryocoolers away from the mirrors maintaining an efficient heat transfer. To better reduce the vibrations, the cooling line will be composed of different parts connected together with soft heat links characterized by high thermal conductivity: typical materials used are high purity aluminum and copper. Soon a first prototype of this cooling line will be tested in the Amaldi Research Center, a laboratory located at Sapienza University, Rome. Before the tests, thermal simulations with ANSYS Mechanical can be performed to understand the relevance, in the expected temperature gradient, of the choice of the materials' parameters such as thermal conductivity, emissivity and specific heat. The thesis will show the results for variations in the number of heat links too: this may be one of the crucial points in the entire design of the cooling line because we need both to reduce the vibrations (so a low number of heat links is required) and to transfer heat efficiently (high number of heat links is required). The cooling time of the simulated model will, also, be studied for different parameter configurations.

The thesis is organized as follows.

Chapter 1 will introduce GWs from a mathematical point of view. The derivation of the standard d'Alembert equation for GWs will be presented through a perturbative approach focusing on the possible polarizations of the wave. After the mathematical derivation of GWs' emission, the four different types of GWs will be described.

Chapter 2 will describe the fundamental concepts of GWs' observations and the particular characteristics of the GWs' observatories (optics and noises). Particular attention will be paid to the description of the features of the existing cryogenic interferometer Kamioka Gravitational Wave Detector (KAGRA).

Chapter 3 will introduce the next generation GWs' observatory ET with its scientific targets and characteristics. The Amaldi Research Center will be presented in this Chapter with some sketches of the facility.

Chapter 4 will explain the theory of heat transfer introducing, then, the real model that can be tested in the Amaldi Research Center and a simplified model used in the simulations.

Chapter 5 will be the main chapter of the thesis on the simulative point of view. It will show all the different types of simulations performed with different conditions and models making comparisons between them.

Chapter 6 will present an experimental measurement of thermal conductivity of high purity (99.9999% purity (6N)) aluminum. Such type of measurement has a crucial role in the complete characterization of the model: high purity materials, such as aluminum, have a high thermal conductivity value in the low-temperature regime but the value depends upon the history of the material itself (different treatments performed). The direct measurement of a sample of the material used in the real application is necessary to perform adequate simulations.

Chapter 1

Gravitational Waves

Gravitational Waves (GWs) are ripples of spacetime caused by high mass accelerating objects with a certain degree of asymmetry. They were predicted by Albert Einstein in 1916 on the basis of his General Theory of Relativity but the first, indirect, evidence of their existence was only in 1974, 20 years after Einstein's death. In that year Hulse and Taylor discovered the binary star system composed of a neutron star and a pulsar, known as PSR 1913+16, exactly the system that, according to General Relativity, could cause the perturbations of spacetime. After some years of observations, they determined that the star were getting closer to each other at the same rate predicted in Einstein's theory. The first direct observation of GWs occurred on September 14, 2015 when the signal (GW150914), generated by the merger of two black holes, was revealed by the Laser Interferometry Gravitational-Wave Detector (LIGO), GWs detectors in Livingston (Washington) and Hanford (Louisiana).
Similarly to Electromagnetic Waves, GWs propagate at the speed of light but they have a distinctive feature: they aren't waves that propagate in the spacetime, they actually are waves of the spacetime.

1.1 Derivation of GWs

Gravitational waves can be derived in different ways. [10]

1. "Exact" approach: consist in the search for an analytical solution of Einstein's equations imposing particular symmetries;

2. perturbative approach: far from the source, GWs can be described as small perturbations on a given background;

3. numerical approach: when GWs cannot be considered small or it's impossible to exploit symmetries, numerical integration of the full, non-linear, Einstein's equations is required.

Let's go into the details of the perturbative approach.
We can consider the background spacetime as the Minkowski flat spacetime defined

with the metric $g^0_{\mu\nu} = \eta_{\mu\nu}$:

$$\eta_{\mu\nu} = \begin{pmatrix} -1 & 0 & 0 & 0 \\ 0 & 1 & 0 & 0 \\ 0 & 0 & 1 & 0 \\ 0 & 0 & 0 & 1 \end{pmatrix} \tag{1.1}$$

Let's consider a small perturbation of $g^0_{\mu\nu}$ caused by some source that can be described with $h_{\mu\nu}$ with the condition $|h_{\mu\nu}| << \left|g^0_{\mu\nu}\right|$, i.e. the weak-field approximation. Thus the metric becomes:

$$g_{\mu\nu} = g^0_{\mu\nu} + h_{\mu\nu}. \tag{1.2}$$

The inverse metric is

$$g^{\mu\nu} = g^{0\,\mu\nu} - h^{\mu\nu} + \mathcal{O}(h^2) \tag{1.3}$$

where the indices of $h^{\mu\nu}$ have been raised with the unperturbed metric[1]:

$$h^{\mu\nu} = g^{0\,\mu\alpha}g^{0\,\nu\beta}h_{\alpha\beta}. \tag{1.4}$$

We can compute the equations governing the dynamic of $h_{\mu\nu}$ starting with Einstein's equations that can be written in the form:

$$R_{\mu\nu} = \frac{8\pi G}{c^4}(T_{\mu\nu} - \frac{1}{2}g_{\mu\nu}T) \tag{1.5}$$

where $T_{\mu\nu}$ is the stress-energy tensor which is composed of two terms: one, $T^0_{\mu\nu}$, associated with the source that generates the background metric $g^0_{\mu\nu}$ and another, $\delta T_{\mu\nu}$, associated with the perturbation $h_{\mu\nu}$, hence $\delta T_{\mu\nu} \sim \mathcal{O}(h)$. Since the considered background is flat, $T^0_{\mu\nu} = 0$.
T is the trace of stress-energy tensor obtained by contracting it with the inverse metric 1.3:

$$T = g^{\mu\nu}T_{\mu\nu} = (g^{0\,\mu\nu} - h^{\mu\nu})\delta T_{\mu\nu} + \mathcal{O}(h^2) = g^{0\,\mu\nu}\delta T_{\mu\nu} + \mathcal{O}(h^2) = \delta T. \tag{1.6}$$

Consequently:

$$(T_{\mu\nu} - \frac{1}{2}g_{\mu\nu}T) = (\delta T_{\mu\nu} - \frac{1}{2}(g^0_{\mu\nu} + h_{\mu\nu})\delta T) = (\delta T_{\mu\nu} - \frac{1}{2}g^0_{\mu\nu}\delta T) + \mathcal{O}(h^2). \tag{1.7}$$

$R_{\mu\nu}$ in Equation 1.5 is the Ricci tensor which can be written by means of Christoffel symbol $\Gamma^\gamma_{\beta\mu}$ and its derivatives [2]:

$$\Gamma^\lambda_{\mu\nu} = \frac{1}{2}g^{\lambda\rho}(g_{\rho\mu,\nu} + g_{\rho\nu,\mu} - g_{\mu\nu,\rho}) \tag{1.8}$$

$$R_{\mu\nu} = \Gamma^\alpha_{\mu\nu,\alpha} - \Gamma^\alpha_{\mu\alpha,\nu} + \Gamma^\alpha_{\sigma\alpha}\Gamma^\sigma_{\mu\nu} - \Gamma^\alpha_{\sigma\nu}\Gamma^\sigma_{\mu\alpha}. \tag{1.9}$$

---

[1]Greek indices (μ, ν, ...) takes values 0, 1, 2, 3. The 0 represents the time coordinate ($x^0 = ct$) and 1,2,3 are the spatial coordinates of the usual three-dimensional space. If they appear superscript and subscript simultaneously in the same term, they are summed $x^\mu x_\mu \equiv \sum_{\mu=0}^{3} x^\mu x_\mu$.

[2]The notation $"\,,\mu\,"$ indicates the derivative of the left-side member in respect of the right-side indices: $g_{\alpha\beta,\mu} \equiv \frac{\partial g_{\alpha\beta}}{\partial x^\mu}$

We can compute the Christoffel symbol in Equation 1.8 in the flat background, using the metric 1.2:

$$g_{\alpha\beta,\mu} = \frac{\partial(g^0_{\alpha\beta} + h_{\alpha\beta})}{\partial x^\mu} = h_{\alpha\beta,\mu} \tag{1.10}$$

hence

$$\Gamma^\lambda_{\mu\nu} = \frac{1}{2}g^{0\,\lambda\rho}(h_{\rho\mu,\nu} + h_{\rho\nu,\mu} - h_{\mu\nu,\rho}) + \mathcal{O}(h^2). \tag{1.11}$$

The Ricci tensor can then be reduced to:

$$R_{\mu\nu} = \Gamma^\alpha_{\mu\nu,\alpha} - \Gamma^\alpha_{\mu\alpha,\nu} + \mathcal{O}(h^2) = \frac{1}{2}g^{0\,\alpha\rho}[h_{\rho\mu,\nu\alpha} + h_{\rho\nu,\mu\alpha} - h_{\mu\nu,\rho\alpha} - h_{\rho\mu,\alpha\nu} - h_{\rho\alpha,\mu\nu} +$$
$$+ h_{\mu\alpha,\rho\nu}] + \mathcal{O}(h^2) = \frac{1}{2}g^{0\,\alpha\rho}[h_{\rho\nu,\mu\alpha} - h_{\mu\nu,\rho\alpha} - h_{\rho\alpha,\mu\nu} + h_{\mu\alpha,\rho\nu}] + \mathcal{O}(h^2). \tag{1.12}$$

Let's define the d'Alembertian in flat spacetime $\Box_F$:

$$\Box_F = g^{0\,\alpha\beta}\frac{\partial^2}{\partial x^\alpha \partial x^\beta} \equiv -\frac{1}{c^2}\frac{\partial^2}{\partial t^2} + \nabla^2. \tag{1.13}$$

Thus, the Ricci tensor becomes:

$$R_{\mu\nu} = \frac{1}{2}[-\Box_F h_{\mu\nu} + (h^\alpha_{\ \nu,\mu\alpha} - h_{,\mu\nu} + h_\mu^{\ \rho}_{,\rho\nu})] \tag{1.14}$$

in which perturbations were contracted with the inverse background metric $g^{0\,\alpha\rho}$ and is used

$$g^{0\,\alpha\rho}h_{\rho\alpha,\mu\nu} = (g^{0\,\alpha\rho}h_{\rho\alpha})_{,\mu\nu} = (h^\alpha_{\ \alpha})_{,\mu\nu} = h_{,\mu\nu} \tag{1.15}$$

in which h is the perturbation tensor's trace.

Finally, Einstein's equations 1.5 can be written as:

$$\Box_F h_{\mu\nu} - (h^\alpha_{\ \nu,\mu\alpha} - h_{,\mu\nu} + h_\mu^{\ \rho}_{,\rho\nu}) = -\frac{16\pi G}{c^4}(\delta T_{\mu\nu} - \frac{1}{2}g^0_{\mu\nu}\delta T). \tag{1.16}$$

Choosing the Harmonic gauge $\Gamma^\lambda = g^{\mu\nu}\Gamma^\lambda_{\mu\nu} = 0$, we can further reduce these equations:

$$g^{\mu\nu}\Gamma^\lambda_{\mu\nu} = \frac{1}{2}g^{0\,\mu\nu}g^{0\,\lambda\rho}(h_{\rho\mu,\nu} + h_{\rho\nu,\mu} - h_{\mu\nu,\rho}) = \frac{1}{2}g^{0\,\lambda\rho}(h^\nu_{\ \rho,\nu} + h^\mu_{\ \rho,\mu} - h_{,\rho}), \quad (1.17)$$

since the first two terms in brackets are equal, in the Harmonic gauge we can consider:

$$h^\mu_{\ \rho,\mu} = \frac{1}{2}h_{,\rho} \tag{1.18}$$

Using 1.18, brackets in the left-side term in Equation 1.16 vanish.
Hence Einstein's equations reduce to simple wave equations with the gauge condition 1.18,

$$\begin{cases} \Box_F h_{\mu\nu} = -\frac{16\pi G}{c^4}(\delta T_{\mu\nu} - \frac{1}{2}g^0_{\mu\nu}\delta T) \\ h^\mu_{\ \nu,\mu} = \frac{1}{2}h_{,\nu} \end{cases} \tag{1.19}$$

If we introduce the trace-reversed perturbation tensor $\bar{h}_{\mu\nu}$,

$$\bar{h}_{\mu\nu} \equiv h_{\mu\nu} - \frac{1}{2}g^0_{\mu\nu}h \tag{1.20}$$

which has its trace $\bar{h}$

$$\bar{h} = g^{0\,\mu\nu}\bar{h}_{\mu\nu} = -h, \tag{1.21}$$

Einstein's equations become:

$$\begin{cases} \Box_F \bar{h}_{\mu\nu} = -\frac{16\pi G}{c^4}\delta T_{\mu\nu} \\ \bar{h}^\mu_{\ \nu,\mu} = 0. \end{cases} \tag{1.22}$$

Away from the source, where the stress-energy tensor is null,

$$\begin{cases} \Box_F \bar{h}_{\mu\nu} = 0 \\ \bar{h}^\mu_{\ \nu,\mu} = 0. \end{cases} \tag{1.23}$$

Since the first of Equations 1.23 is the standard d'Alembert equation, Einstein's theory of gravity predicts the existence of gravitational waves in the form of perturbation of a flat spacetime propagating as a wave traveling at the speed of light.

1.2 Gravitational waves polarization

It can be shown that the general solution of Equations 1.23 is a linear superposition of monochromatic plane waves of the form:

$$\bar{h}_{\mu\nu} = \Re\left[A_{\mu\nu}e^{ik_\alpha x^\alpha}\right] \tag{1.24}$$

where $A_{\mu\nu}$ is the polarization tensor, i.e. the wave amplitude, k^α is the wave four-vector and $\Re(z)$ indicates the real part of any complex number z, which hereafter will be omitted for simplicity.
By direct substitution of Equation 1.24 in 1.23, we can find two conditions that have to be satisfied:

$$\begin{cases} k_\mu k^\mu = 0 \\ k_\mu A^\mu_{\ \nu} = 0. \end{cases} \tag{1.25}$$

The former condition indicates that k^α is a null vector, hence the gravitational wave propagates at the speed of light; the latter shows that the plane wave is orthogonal to the wave four-vector.
Conventionally $k^0 = \frac{\omega}{c}$, in which ω is the wave pulsation, and the three remaining components $(k^1,\,k^2,\,k^3)$ are the wave three-vector $\vec{k}$,

$$k^\alpha = (\frac{\omega}{c},\vec{k}). \tag{1.26}$$

Since $\bar{h}_{\mu\nu}$ is a symmetric tensor, it has 10 free components that represent the degrees of freedom of the wave: these can be reduced by imposing the Transverse-Traceless (TT) gauge. In this gauge, $h_{\mu\nu}$ and $\bar{h}_{\mu\nu}$ coincide and are traceless. Choosing the propagating direction along the x-axis, the propagation tensor can be written as:

$$h_{\mu\nu}^{TT} = \begin{pmatrix} 0 & 0 & 0 & 0 \\ 0 & 0 & 0 & 0 \\ 0 & 0 & h_{yy} & h_{yz} \\ 0 & 0 & h_{yz} & -h_{yy} \end{pmatrix}. \tag{1.27}$$

Figure 1.1. In the upper panels are shown the relative positions of two test particles (or ring of test particles in the lower panels) due to the passage of a GW propagating along the x-axis with polarization " + ". The different panels in the row are taken in fixed times that are a fraction of the wave's period.

A gravitational wave has only two physical degrees of freedom which correspond to two polarization states. As a typical wave solution, there will be a progressive solution $\sim(t - \frac{x}{c})$ and a regressive one $\sim(t + \frac{x}{c})$. Focusing on the former, we can obtain, studying the geodesic deviation:

$$\begin{cases} h_{yy}^{TT} = -h_{zz}^{TT} = 2\,A_+ e^{i\omega(t-\frac{x}{c})} \\ h_{yz}^{TT} = h_{zy}^{TT} = 2\,A_\times e^{i\omega(t-\frac{x}{c})} \end{cases} \tag{1.28}$$

where, in general, A_+ and $A_\times$ are complex constant, e.g. $A_+ = |A_+|e^{i\Phi_0}$.
We can study the effects on two test particles (initially at rest) or a ring of test particles considering 1.28 in the case that, alternatively, only one polarization takes place. We can visualize the TT coordinate frame as a grid of massive particles initially at rest: at the passage of a gravitational wave, the grid stretches but the coordinate positions of test particles remain, by definition, constant. The wave with pulsation ω will have a period $P = \frac{2\pi}{\omega}$ and we can observe the relative positions of the two particles (or ring) under the effects of a wave of polarization " + " (or " × ") in Figure 1.1 (or 1.2). The different panels in the rows are obtained at fixed times that are fractions of the GW's period: they represent the extremal deformations that particles' positions undergo. GW's passage changes the proper distance between bodies, i.e. a scalar quantity invariant under coordinate transformations. If two particles are on the y-axis,

$$\Delta l \;=\; \int ds \;=\; \int_{y_A}^{y_B} |g_{yy}|^{\frac{1}{2}} dy \;\sim\; \left[1 + \frac{1}{2} h_{yy}^{TT}\left(t - \frac{x}{c}\right)\right] \;\neq\; const \tag{1.29}$$
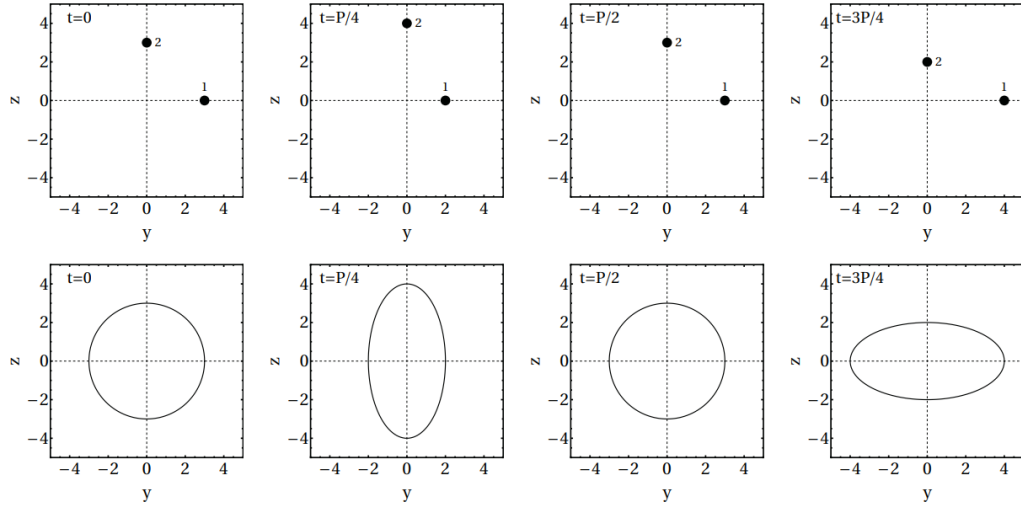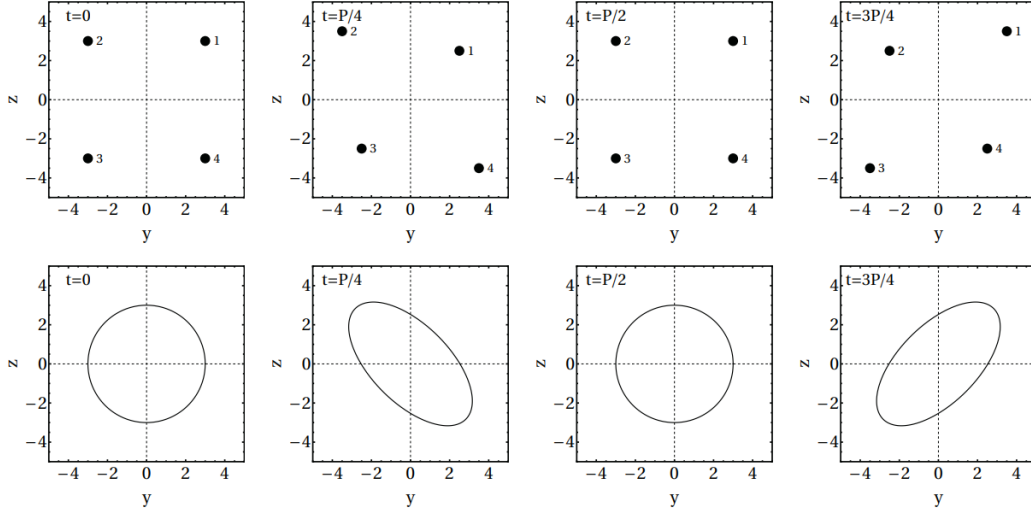
Figure 1.2. In the upper panels are shown the relative positions of two test particles (or ring of test particles in the lower panels) due to the passage of a GW propagating along the x-axis with polarization " × ". The different panels in the row are taken in fixed times that are a fraction of the wave's period.

1.3   Gravitational waves emission

A general solution of Equation 1.22, considering a source described through $\delta T_{\mu\nu}$, can be derived by assuming another approximation: the slow-motion approximation. Considering the source confined in a region of size ϵ, namely:

$$T_{\mu\nu} \begin{cases} \neq 0 & if \quad |x^i| < \epsilon \\ = 0 & otherwise \end{cases}$$
(1.30)

we have to impose that this typical length ϵ is much smaller than the wavelength of the emitted GW, $\lambda_{GW} = \frac{2\pi c}{\omega}$, hence:

$$\frac{2\pi c}{\omega} >> \epsilon \quad \rightarrow \quad \epsilon\omega << c \quad \rightarrow \quad v_{typical} << c.$$
(1.31)

We are then assuming that typical velocities of the source are much smaller than the speed of light, which explain the name of this approximation.
It can be shown that the solution of the inhomogeneous d'Alembertian Equation 1.22 can be written in terms of retarded potentials,

$$\bar{h}_{\mu\nu}(t,x) = \frac{4G}{c^4} \int_V \frac{T_{\mu\nu}(t - \frac{|x-x'|}{c}, x')}{|x - x'|} d^3x'$$
(1.32)

where $t - \frac{|x-x'|}{c}$ is the retarded time and $\frac{|x-x'|}{c}$ is the time that the wave takes to travel from the element at x' on the source to the observer located at x (see Figure 1.3); the volume V over which the integral is performed is the entire three-dimensional
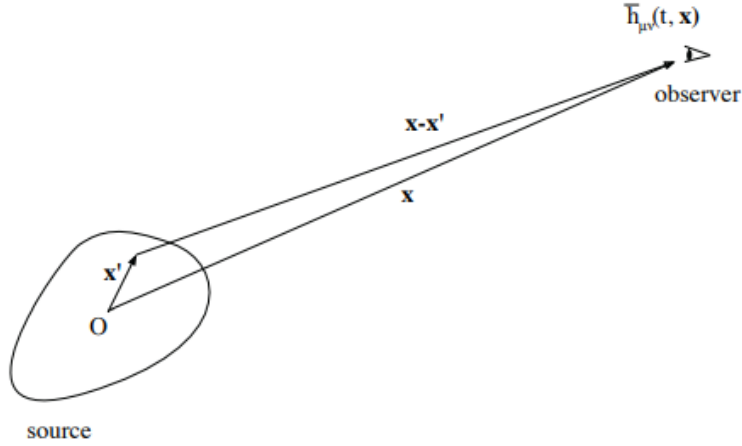
Figure 1.3. An observer at a distance x from the source receives a wave $\bar{h}(t,x)$ at the time t which is the sum of contributions emitted from each source element located in x' at the retarded time $t - \frac{x-x'}{c}$.

source's volume.

In the weak-field, slow-motion approximation, Equation 1.32 can be reduced to

$$\bar{h}_{\mu\nu}(t,r) = \frac{4G}{c^4 r} \int_V T_{\mu\nu}(t - \frac{r}{c}, x')d^3x' \tag{1.33}$$

where $r = |x|$ is the distance between the observer and the point-like source $(|x - x'| \sim |x|)$.

Equation 1.33 can be further simplified using the tensor-virial theorem and by the introduction of the quadrupole moment tensor of a dynamical system

$$q^{ij}(t) = \frac{1}{c^2} \int_V T^{00}(t,x)x^i x^j d^3x. \tag{1.34}$$

The perturbation tensor can then be written as:

$$\begin{cases} \bar{h}^{\mu 0} = 0 \\ \bar{h}^{ij}(t,r) = \frac{2G}{c^4 r} \frac{d^2}{dt^2} q^{ij}(t - \frac{r}{c}) \end{cases} \tag{1.35}$$

which is called quadrupole formula and describes GWs emitted by a gravitational system evolving in time.

General Relativity predicts that GWs do not have monopolar or dipolar contributions. We can explain the absence of the dipolar contribution by comparing the gravitational case with the electromagnetic one: a system of accelerating charges emits dipole radiation with a flux that depends on the second time derivative of the electric dipole moment

$$\vec{d}_{EM} = \sum_i q_i \vec{r}_i \tag{1.36}$$

where q_i and $\vec{r}_i$ are, respectively, the charge and the position of the i-th particle. If $\frac{d^2}{dt^2}\vec{d}_{EM} = 0$, the system does not emit electromagnetic waves.

In the gravitational scenario, a similar gravitational dipole moment is

$$\vec{d}_G = \sum_i m_i \vec{r}_i, \tag{1.37}$$

its time derivative, actually, is the total momentum of the system that, in the case of an isolated object, is conserved:

$$\frac{d}{dt}\vec{d}_G = \vec{0} \quad \rightarrow \quad \frac{d^2}{dt^2}\vec{d}_G = \vec{0}. \tag{1.38}$$

Similarly, the conservation of energy leads to the absence of a monopolar component (which holds also in the electromagnetic case).
Equation 1.35 gives us information about the different sources that can emit GWs, at least in the regime settled by the approximations imposed. The only non-zero terms are the spatial ones that depend on the second time derivative of the quadrupole moment tensor; hence, any form of mass and energy can be a GW's source as long as its quadrupole moment tensor's second time derivative is non-vanishing. For a spherical or axisymmetric, stationary distribution of matter (or energy), the quadrupole moment is constant, even if the body is rotating. Also stars that collapse, explode or radially pulsate, maintaining a spherical symmetric shape, do not emit gravitational waves. A source can only emit GWs if it has a certain degree of asymmetry.
The quadrupole formula 1.35 describes a spherical wave far from the emitting source that, locally, looks like a plane wave propagating in the direction settled by the unit vector n:

$$n^\alpha = (0, n^i) \quad with \quad n^i = \frac{x^i}{r}. \tag{1.39}$$

We can express the perturbation tensor in the TT gauge by projecting the Equation 1.35 in the plane orthogonal to the direction of n and with the condition of being traceless. Let's introduce the transverse-traceless projector:

$$\mathcal{P}_{jkmn} \equiv P_{jm}P_{kn} - \frac{1}{2}P_{jk}Pmn$$
$$P_{jk} \equiv \delta_{jk} - n_j n_k. \tag{1.40}$$

The quadrupole formula in the TT gauge can then be written

$$\begin{cases} h_{\mu 0}^{TT} = 0 \\ h_{jk}^{TT}(t, r) = \frac{2G}{c^4 r}\frac{d^2}{dt^2}Q_{jk}^{TT}\left(t - \frac{r}{c}\right) \end{cases} \tag{1.41}$$

with the definition of the transverse-traceless part of the quadrupole moment Q_{jk}^{TT}:

$$Q_{jk}^{TT} \equiv \mathcal{P}_{jkmn}q_{mn}. \tag{1.42}$$

In order to evaluate how much energy and momentum are radiated in gravitational waves, we need a tensor that describes these quantities; such a tensor does not exist. We can, however, introduce a pseudo-tensor, i.e. a quantity which behaves like a tensor only under specific transformations, which carries information on the energy and momentum of the gravitational field: the Landau-Lifshitz stress-energy pseudo-tensor $t^{\mu\nu}$.

It can be demonstrated that with this pseudo-tensor, the energy flux of a gravitational wave can be described with:[3]

$$\frac{dE_{GW}}{dtdS} = \frac{c^3}{32\pi G} \left\langle \sum_{jk} (\dot{h}_{jk}^{TT}(t,r))^2 \right\rangle \tag{1.43}$$

where the $\langle\,.\,\rangle$ is the Brill-Hartle average which is performed over several GW wavelengths. Using Equation 1.41 in 1.43 we find

$$\frac{dE_{GW}}{dtdS} = \frac{G}{8\pi c^5 r^2} \left\langle \sum_{jk} (\dddot{Q}_{jk}^{TT}(t-\frac{r}{c}))^2 \right\rangle. \tag{1.44}$$

Integrating 1.44 with the surface element $dS = r^2 d\Omega$ and exploiting the properties of $\mathcal{P}_{jkmn}$, we obtain the luminosity quadrupole formula

$$L_{GW}(t) = \frac{G}{5c^5} \left\langle \dddot{Q}_{jk}(t-\frac{r}{c})\dddot{Q}_{jk}(t-\frac{r}{c}) \right\rangle \tag{1.45}$$

which describes the energy emitted by a source per unit time. Q_{jk} that appears in Equation 1.45 is the reduced quadrupole moment tensor

$$Q_{jk} \equiv q_{jk} - \frac{1}{3}\delta_{jk}q^m{}_m \tag{1.46}$$

that is traceless by definition.

1.4   Gravitational waves types and relative sources

As already mentioned in Section 1.3, any form of matter and energy with a certain degree of asymmetry can be a GWs source. We can divide GWs into four different categories based on what generates them:[19], [25]

1. compact binary inspiral GWs,

2. continuous GWs,

3. stochastic GWs,

4. burst GWs.

Compact Binary Inspiral Gravitational Waves   These types of gravitational waves are produced by orbiting pairs of massive and dense objects. The term compact refers to the compactness $C = \frac{GM}{Rc^2}$ of bodies, this quantity is useful to compute the importance of General Relativity effects near the surface of an object with mass M and radius R. We refer to a compact object in this case because we need very massive bodies to produce observable GWs. For these reasons, we can identify three different subclasses of compact binary system: Binary Neutron Star (

---

[3]The notation $\dot{h}$ indicates the time derivative of h, $\dot{h} = \frac{d}{dt}h$. We can extend this notation also for the successive derivatives, $\ddot{h} = \frac{d^2}{dt^2}h$ and $\dddot{h} = \frac{d^3}{dt^3}h$.
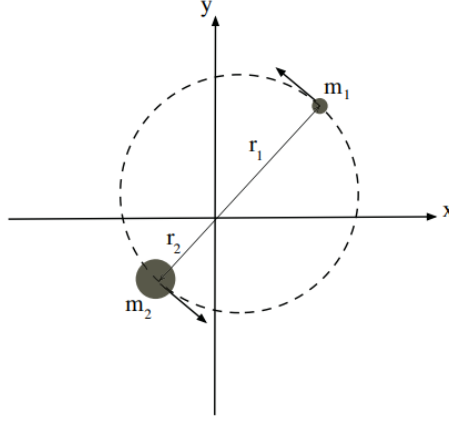
Figure 1.4. Two point-like masses in a circular orbit around the common center of mass.

NS-NS), Binary Black Holes (BH-BH) and Neutron Star - Black Hole Binary (NS - BH). All three of them create a unique pattern of GWs but they share the same mechanism of wave generation which is called coalescence.

Coalescence occurs over millions of years as pairs of dense compact objects revolve around each other: as they orbit, they emit GWs that carry away some orbital energy. As a consequence, objects start to get closer and closer over eons. This leads them to orbit faster losing more energy: objects are then doomed to continue this process until the final merger of the two.

We can mathematically describe this scenario using a simple case [10]. Let's consider two point-like masses m_1 and m_2 moving in a circular orbit around their center of mass. Let l_0 be their orbital separation, $M = m_1 + m_2$ their total mass and μ the reduced mass:

$$\mu = \frac{m_1 m_2}{M}. \tag{1.47}$$

Let's place the origin of the coordinate frame at the center of mass as indicated in Figure 1.4 so:

$$l_0 = r_1 + r_2, \quad r_1 = \frac{m_2 l_0}{M}, \quad r_2 = \frac{m_1 l_0}{M}. \tag{1.48}$$

We can derive the Keplerian frequency of the system ω_K:

$$\omega_K = \sqrt{\frac{GM}{l_0^3}}. \tag{1.49}$$

Referring to the quadrupole moment tensor 1.34, we need the 00-component of the stress-energy tensor which is:

$$T^{00} = c^2 \sum_{n=1}^{2} m_n \delta(x - x_n)\delta(y - y_n)\delta(z). \tag{1.50}$$

We can then compute all the 9 terms of q_{ij} using the relative position x_1, x_2, y_1, y_2

of the two bodies on a simple circular orbit. The only non-vanishing terms are:

$$
\begin{cases}
q_{xx} = \frac{\mu}{2}l_0^2 cos(2\omega_K t) + const_1 \\
q_{yy} = -\frac{\mu}{2}l_0^2 cos(2\omega_K t) + const_2 \\
q_{xx} = \frac{\mu}{2}l_0^2 sin(2\omega_K t).
\end{cases}
\tag{1.51}
$$

Defining a matrix A_{ij} as

$$
A_{ij}(t) = \begin{pmatrix} cos(2\omega_K t) & sin(2\omega_K t) & 0 \\ sin(2\omega_K t) & -cos(2\omega_K t) & 0 \\ 0 & 0 & 0 \end{pmatrix}
\tag{1.52}
$$

we can write

$$
q_{ij} = \frac{\mu}{2}l_0^2 A_{ij} + const.
\tag{1.53}
$$

Using Equation 1.41, we can find the perturbation tensor in the TT-gauge

$$
h_{ij}^{TT}(t,r) = -\frac{4\mu M G^2}{r l_0 c^4}\mathcal{P}_{ijkl}A_{kl}\left(t - \frac{r}{c}\right).
\tag{1.54}
$$

From Equation 1.54 it is possible to obtain the different wave polarizations that depend upon the unit vector considered in the projector.
We can now estimate the time variation of the orbit parameters due to the emission. Let's consider the adiabatic regime, i.e. the condition in which the energy lost by the GW emission is compensated by the system changing its orbital energy,

$$
\frac{dE_{orb}}{dt} + L_{GW} = 0.
\tag{1.55}
$$

Using the typical E_{orb} of a simple circular orbit

$$
E_{orb} = -\frac{1}{2}\frac{G\mu M}{l_0}
\tag{1.56}
$$

and Equation 1.45 computed with Equation 1.53, we find the evolution of orbital separation $l_0(t)$

$$
l_0^4(t) = (l_0^{in})^4 - \frac{256}{5}\frac{G^3}{c^5}\mu M^2 t.
\tag{1.57}
$$

Defining

$$
t_c \equiv \frac{5}{256}\frac{c^5}{G^3}\frac{(l_0^{in})^4}{\mu M^2}
\tag{1.58}
$$

we obtain

$$
l_0(t) = l_0^{in}\left(1 - \frac{t}{t_c}\right)^{1/4}
\tag{1.59}
$$

which shows that the orbital separation decreases with time and becomes zero when $t = t_c$. This is a consequence of point-like sources' assumption: stars and black holes have finite sizes so they merge before that time. In addition, during the last cycles of the inspiral, both the assumption of weak-field and slow-motion fail, so the strong field effect should be considered. However, these last phases are faster than the adiabatic period so t_c provides a good estimate of the coalescence time of binary

systems.

Using Equation 1.59 we can also find the evolution of the frequency ω_K and period P during the inspiral:

$$\omega_K(t) = \sqrt{\frac{GM}{(l_0^{in})^3}}\left(1 - \frac{t}{t_c}\right)^{-3/8} \tag{1.60}$$

and since $\omega_K = 2\pi P^{-1}$

$$P(t) = P^{in}\left(1 - \frac{t}{t_c}\right)^{3/8} \tag{1.61}$$

which shows that as $t \to t_c$, the orbital frequency increases and the period decreases. The first indirect evidence of GWs precisely relies on Equation 1.61: Hulse and Taylor's result of the shift in time of periastron passage for PSR 1913+16 is in agreement with Equation 1.61 corrected for eccentricity, the kinematic of the center of mass and other effects.

Furthermore, the perturbation tensor can be evaluated during the evolution using Equation 1.59 in 1.54. We can express the GW frequency using the fact that it is emitted at twice the Keplerian frequency i.e. $\nu_{GW} = 2\nu_K = \frac{\omega_K}{\pi}$, so

$$\nu_{GW}(t) = \nu_{GW}^{in}\left(1 - \frac{t}{t_c}\right)^{-3/8} \quad with \quad \nu_{GW}^{in} \equiv \frac{1}{\pi}\sqrt{\frac{GM}{(l_0^{in})^3}}. \tag{1.62}$$

The signal can then be expressed as

$$h_{ij}^{TT}(t,r) = -h_0\left(t - \frac{r}{c}\right)\mathcal{P}_{ijkl}A_{kl}\left(t - \frac{r}{c}\right) \tag{1.63}$$

where

$$h_0(t) = \frac{4\pi^{2/3}G^{5/3}}{c^4}\frac{\mathcal{M}}{r}(\mathcal{M}\nu_{GW}(t))^{2/3}. \tag{1.64}$$

In Equation 1.64 is exploited the chirp mass $\mathcal{M}$:

$$\mathcal{M} = \mu^{3/5}M^{2/5} = \frac{(m_1 m_2)^{3/5}}{M^{1/5}}. \tag{1.65}$$

Both amplitude and frequency of the signal emitted during the inspiral increase with time: this feature is typical of the chirp of a singing bird and for this reason, this part of the signal is called chirp and $\mathcal{M}$ chirp mass.

These types of GWs are one of the most important ones because, until now, they are the only ones that we achieved to observe. Indeed, the first observation, the already mentioned GW150914, was of this sort: it was the signal related to the last phase of the inspiral between two black holes with masses $m_1 = 35.6^{+4.8}_{-3.0}M_\odot$ and $m_2 = 30.6^{+3.0}_{-4.4}M_\odot$.

Continuous Gravitational Waves Continuous GWs refer to signals generated by a single spinning massive object, neutron stars are the perfect example. As already mentioned in Section 1.3 axisymmetric stars can't emit GWs so, for this type of signal, we have to search for bumps or imperfections in the spherical shape of neutron stars: these can be produced from crustal deformation (e.g. from cooling
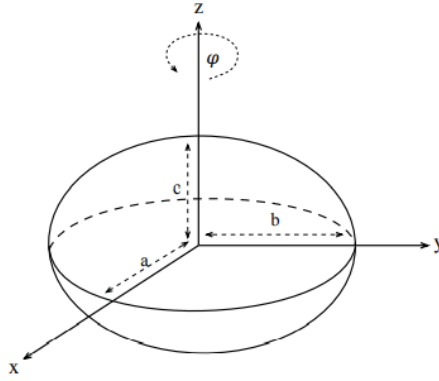
Figure 1.5. Ellipsoidal star rotating around the principal axis z.

and cracking of the crust) or from non-axisymmetric distribution of magnetic field energy trapped beneath the crust. Gravitational waves produced by this mechanism are usually much longer than observation time, with an approximately constant frequency that depends upon the star rotation rate.

We can refer to the same quadrupole formalism already introduced to mathematically describe a simple example of this emission[10]. Let's consider an ellipsoidal star with uniform density ρ, rigidly rotating around an axis with angular velocity Ω (see Figure 1.5).

We can compute the quadrupole moment tensor of the star referring to Equation 1.34 with the 00-component of the stress-energy tensor which is $T^{00} = \frac{\rho}{c^2}$:

$$q_{ij} = \int_V \rho x_i x_j d^3 x. \tag{1.66}$$

We can also define the inertia tensor

$$I_{ij} = \int_V \rho(r^2 \delta_{ij} - x_i x_j) d^3 x. \tag{1.67}$$

The two are then related by

$$q_{ij} = -I_{ij} + \delta_{ij} q^k{}_k. \tag{1.68}$$

Computing the inertia tensor referring to the ellipsoid with Equation:

$$\left(\frac{x^1}{a}\right)^2 + \left(\frac{x^2}{b}\right)^2 + \left(\frac{x^3}{c}\right)^2 = 1 \tag{1.69}$$

we obtain:

$$I_{ij}(t) = \frac{M}{5} \begin{pmatrix} b^2 + c^2 & 0 & 0 \\ 0 & c^2 + a^2 & 0 \\ 0 & 0 & a^2 + b^2 \end{pmatrix} = \begin{pmatrix} I_1 & 0 & 0 \\ 0 & I_2 & 0 \\ 0 & 0 & I_3 \end{pmatrix}. \tag{1.70}$$

Considering a generic rotation matrix R_{ij} which depends on $\varphi = \Omega t$, we can obtain the inertia tensor in the inertial frame

$$I_{ij} = (RI'R^T)_{ij} \tag{1.71}$$

this lead to

$$Q_{ij} = \frac{I_2 - I_1}{2} \begin{pmatrix} cos(2\varphi) & sin(2\varphi) & 0 \\ sin(2\varphi) & -cos(2\varphi) & 0 \\ 0 & 0 & 0 \end{pmatrix} + const. \tag{1.72}$$

Since $I_1 \propto (b^2 + c^2)$ and $I_2 \propto (c^2 + a^2)$, if $a = b$, i.e. the star is axisymmetric, the reduced quadrupole moment is constant and its second time derivative is null: this type of star does not emit GWs.

If the star is triaxial ellipsoid, i.e. all the semiaxes are different, we expect emission but, since the difference $a - b$ is expected to be small, it is convenient to introduce the oblateness ϵ, or ellipticity, which expresses the deviation from axisymmetry

$$\epsilon \equiv \frac{a - b}{(a + b)/2}. \tag{1.73}$$

Consequently,

$$Q_{ij} = \frac{\epsilon I_3}{2} \begin{pmatrix} cos(2\varphi) & sin(2\varphi) & 0 \\ sin(2\varphi) & -cos(2\varphi) & 0 \\ 0 & 0 & 0 \end{pmatrix} + const. \tag{1.74}$$

Using Equation 1.41, the signal can be expressed as

$$h_{ij}^{TT}(t, r) = h_0 \mathcal{P}_{ijkl} A_{kl} \left(t - \frac{r}{c} \right) \tag{1.75}$$

where

$$A_{kl} = \begin{pmatrix} -cos(2\varphi_{ret}) & -sin(2\varphi_{ret}) & 0 \\ -sin(2\varphi_{ret}) & cos(2\varphi_{ret}) & 0 \\ 0 & 0 & 0 \end{pmatrix}, \qquad \varphi_{ret} = \Omega \left(t - \frac{r}{c} \right) \tag{1.76}$$

and

$$h_0 = \frac{4G\Omega^2}{c^4 r} I_3 \epsilon. \tag{1.77}$$

The detection of continuous gravitational waves from a spinning neutron star should yield precious informations on neutron stars' structure and the equation of state of nuclear matter at extreme pressures when combined with electromagnetic measurements of the same stars.

Stochastic Gravitational Waves   Stochastic gravitational waves arise from a superposition of incoherent sources which create a pattern that can be studied statistically but not predicted precisely. The most relevant component of this type of GWs is the Gravitational Wave Background (GWB) which is composed of primordial GWs created in the Big Bang and during the following phases such as inflation and the different phase transition in the early Universe. Other possible contributions for stochastic GWs are pulsars, very distant mergers of compact binary or cosmic strings, i.e. possible defects remaining from electroweak (or earlier) phase transition or primordial superstrings redshifted to enormous distances.

The possible observation of this type of gravitational wave will allow us to see further back into the history of the Universe and would have a strong impact on early Universe cosmology and high-energy physics.

Burst Gravitational Waves This last type of GWs include all the poorly known or unknown sources that can be imagined. Some remarkable examples are supernovae events with a non-spherical collapse, the sudden release of energy from highly magnetized neutron stars (magnetar) or cosmic strings that could also be detected individually.

Summary of signals In GW astronomy there are different conventions commonly used when signal, noise and sensitivities have to be compared.[20] [10]

The perturbation tensor amplitude h_0 that appears in the previous Sections is a dimensionless quantity: the most frequently used quantity, however, is the square root of the Power Spectral Density (PSD) or strain amplitude of the signal, which has units of $\frac{1}{\sqrt{Hz}}$. It is given by the Fourier transform of the gravitational waveform multiplied by the square root of the wave frequency

$$\sqrt{PSD(\nu)} = \tilde{h}_0 \sqrt{\nu_{GW}}. \tag{1.78}$$
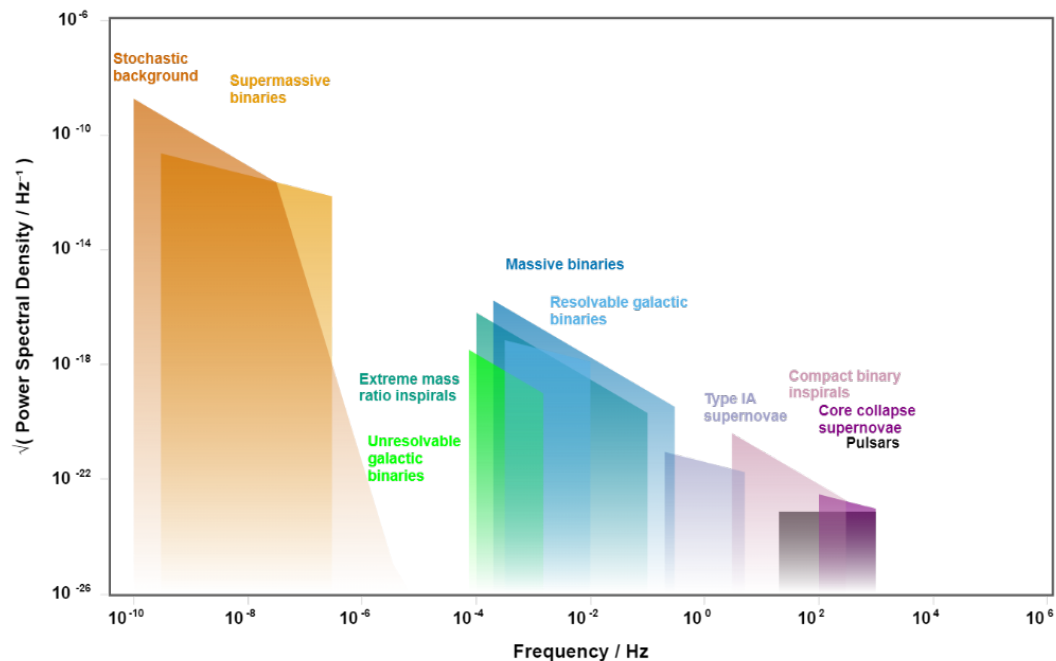
Figure 1.6. Summary of different ranges of $\sqrt{PSD}$ and frequency of the signals described in Section 1.4.[5]

A brief summary of different signal ranges is represented in Figure 1.6. For each source, the square root of PSD is reported in a different color: the thickness of the colored boxes represents instead the typical frequency range of the source's signal. Upon these emission ranges, we have to overlap the sensitivity curves of our detection instruments: in this way, we can understand which of them we are able to observe. The main features of observation techniques and instruments will be the main topic of the next Chapter.

Chapter 2

Gravitational Wave Detectors

As already discussed in Section 1.2, the proper distance between test particles changes under the effect of a GW's passage: this property can be exploited as the basic concept of gravitational wave detectors. Typical detectors, indeed, utilize the principle of laser interferometry. Such detectors work by taking a monochromatic light and splitting it into two beams traveling in optical cavities: their length changes, due to GW's passage, are measured. We can divide these instruments into three different categories each with a particular frequency range for observation: ground-based detectors, space-based detectors and Pulse Timing Arrays (PTAs). We will go into detail about the ground-based ones starting first with the description of the typical Michelson interferometer.

2.1 Michelson interferometer

A classic Michelson interferometer can be easily described by means of the sketch in Figure 2.1.
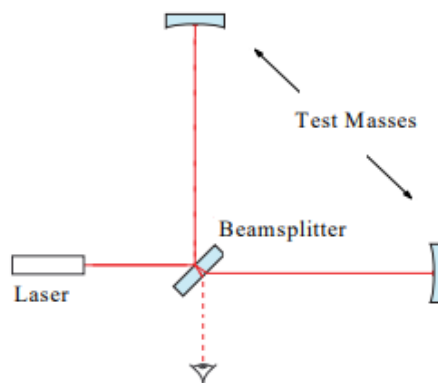

Figure 2.1. Simple sketch of Michelson interferometer.

Let's consider a "+" polarized GW propagating in the z-axis and let the two interferometer's arms be along the x and y-axis. A laser beam enters the interfer-

ometer and it is split in two by a Beam Splitter (BS). The two resulting beams travel along the arms until they are reflected back by two end mirrors (test masses). Reflected beams recombine at the BS to produce interference: when a GW passes through the detector, the proper distances of the two arms change in anti-phase. Therefore, a typical interference pattern will be created at the BS which can be used to detect the GW.

When the wave is entering the interferometer, the generic distance can be written as[10][34]

$$ds^2 = -c^2 dt^2 + (1 + h_+(t))dx^2 + (1 - h_+(t))dy^2 + dz^2. \qquad (2.1)$$

Since $ds^2 = 0$ for light,

$$dx = \pm \frac{cdt}{\sqrt{1 + h_+(t)}} \sim \pm \left(1 - \frac{1}{2}h_+(t)\right) cdt \qquad (2.2)$$

similarly stand for the y-axis. If we consider τ_x (τ_y) as the time the beam takes to travel back and forth the arm,

$$\tau_x = \frac{2L_x}{c} = \int_{t-\tau_x}^{t} \left(1 - \frac{1}{2}h_+(t)\right) dt \qquad (2.3)$$

where L_x (L_y) is the length of the x-arm (y-arm). Let Ω be the angular frequency of the laser, then

$$\phi_x = \Omega\tau_x \sim \Omega\frac{2L_x}{c} + \frac{\Omega}{2}\int_{t-\frac{2L_x}{c}}^{t} h_+(t)dt$$
$$\phi_y = \Omega\tau_y \sim \Omega\frac{2L_y}{c} + \frac{\Omega}{2}\int_{t-\frac{2L_y}{c}}^{t} h_+(t)dt. \qquad (2.4)$$

The total phase difference can then be written as

$$\Delta\phi = \Omega\frac{2(L_x - L_y)}{c} + \frac{\Omega}{2}\int_{t-\frac{2L_x}{c}}^{t} h_+(t)dt + \frac{\Omega}{2}\int_{t-\frac{2L_y}{c}}^{t} h_+(t)dt$$
$$= \Omega\frac{2(L_x - L_y)}{c} + \Delta\phi_{GW}. \qquad (2.5)$$

When $L_x \sim L_y \sim L$ is assumed, the total phase difference is

$$\Delta\phi = \Delta\phi_{GW} = \int_{t-\frac{2L}{c}} h_+(t)dt. \qquad (2.6)$$

If we compute the frequency response of the interferometer, we obtain the simple relation that maximizes this quantity

$$\frac{L\omega_{GW}}{c} = \frac{\pi}{2}. \qquad (2.7)$$

Using Equation 2.7 we understand that, if we consider a GW of $100Hz$, we need an interferometer with an arms' length of $750km$.
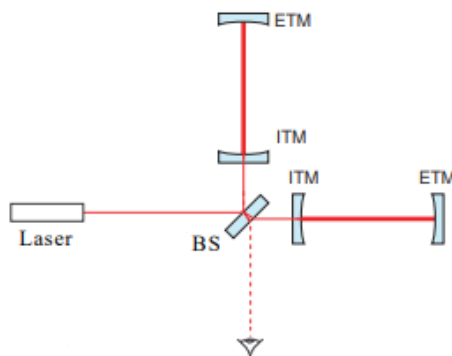
Figure 2.2. Simple sketch of FP Michelson interferometer.

2.1.1 Fabry-Pérot Michelson interferometer

It is almost impossible to construct such a large interferometer: therefore, a Fabry-Pérot (FP) cavity is constructed in each arm to increase their effective length.

In Figure 2.2, we can see the modified sketch of the interferometer with the FP cavity in the arms. Following the beam in one arm, it crosses first a mirror positioned in the middle of the arm, the Input Test Mass (ITM). It is then reflected back by the End Test Mass (ETM). There is a high-reflection coating on the cavity-side of the ITM, so the light is reflected towards the ETM again. The reflectivity of the ITM is slightly lower than the ETM's: therefore the light in the cavity reaches the BS little by little.

We can define some parameters useful to characterize a FP cavity[24]. Let's start from the reflectivities of the cavity-side of the two test masses (in each arm) that we can refer to as r_i for the ITM and r_e for the ETM. We can then define the finesse

$$\mathcal{F} = \frac{\pi\sqrt{r_i r_e}}{1 - r_i r_e} >> 1. \tag{2.8}$$

As already said we want the condition $r_i < r_e$ so that the light gets trapped in the cavity extending its path. We can then compute the storage time τ_s

$$\tau_s = \frac{2L}{\pi c}\mathcal{F} \tag{2.9}$$

that has to be compared with the previous time τ_x (or τ_y):

$$\frac{\tau_s}{\tau_x} = \frac{\mathcal{F}}{\pi} \tag{2.10}$$

so, for a value of $\mathcal{F} >> 1$, the time that light takes to go back to BS significantly rises. The optical path length is then modified from the value of $2L$ to $\frac{8\mathcal{F}L}{\pi}$ which, depending on the value of the finesse, crucially reduces the required length of arms to detect a GW whose frequency is $100Hz$.

2.2 Noise sources

In order to detect tiny signals, as GWs are, every noise sources have to be carefully considered. Whilst space-based detectors could have only a few types of noise (but

obviously other practical issues), the ground-based ones have different types: [24], [23], [9]

1. seismic noise;

2. gravity gradient (Newtonian) noise;

3. shot noise;

4. radiation pressure noise;

5. thermal noise.

Let's briefly discuss each of them.

Seismic noise   Ground is always vibrating not by only earthquakes but also by human activities and natural phenomena (like wind, sea, etc). The easiest way to reduce such a vibration is to choose a quiet place on Earth away from urban areas. Even in this way seismic noise level will be too large for GWs detection. The typical spectrum of seismic noise, for a frequency $f \geq 1Hz$, follows $\sim 10^{-7}\nu^{-2}\frac{m}{Hz^{1/2}}$ (that changes according to places). In the low-frequency range, i.e. below $10Hz$, the sensitivity of detectors would be limited by this noise: the strategy to fight these vibrations is to use the property of harmonic oscillators to attenuate all disturbances above their resonance. Therefore, each test mass is suspended by a chain of several stages in series, each composed of a pendulum, and connected by vertical springs. This setup is called superattenuator and it is the system that suspends all the mirrors in Virgo, the italian interferometer (see Figure 2.3). Seismic noise can be divided into the horizontal and vertical components: the horizontal one can be attenuated by the series of pendulum whilst the vertical are reduced by means of cantilever springs used in the connections of pendulum wire. The pendulum suspension chain itself is supported by a platform resting on an inverted pendulum which provides additional horizontal attenuation.

Gravity Gradient (Newtonian) noise   Seismic waves produce density perturbations in the ground next to test masses which in turn produce fluctuating gravitational forces on them (see Figure 2.4). As a result, the so-called gravity noise is induced in the mirrors: it can't be easily reduced, so what is important is the right choice of site. The location has to be found where the seismic motion is minimal and the surrounding soil as homogeneous as possible. Studies show that underground location (depth of $200m$ to $300m$) in a remote site provides sufficiently low seismic motion. The continuous monitoring of seismic motion and the use of a gravity gradient model, based on that results, can compute the Newtonian noise that can be then subtracted from the interferometer output signal.

Shot noise   Shot noise is caused by statistical fluctuation in the number of photons at the output of the interferometer, i.e. the photodetector at the end of the laser path. We can consider that photons entering the photodetector follow the Poisson
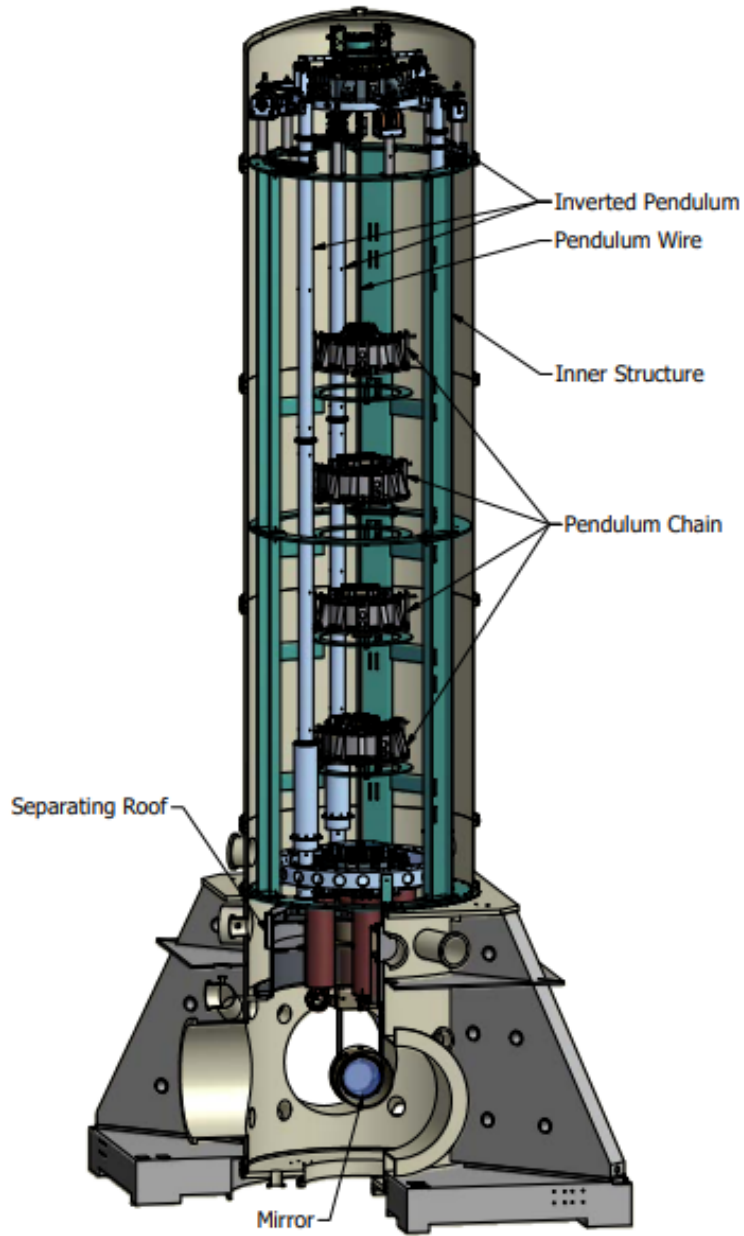
Figure 2.3. Schematic view of a Virgo superattenuator.

statistic so, from statistical calculations, we can compute the total amount of shot noise as

$$\sqrt{PSD_{shot}}(\nu) = \frac{1}{L}\sqrt{\frac{\lambda h c}{4\pi^2 \eta P_{eff}}} \tag{2.11}$$

where L is the length of the interferometer, h is Planck's constant and η is the interferometer's quantum efficiency. We can see that noise depends on the level of laser power P_{eff} (in a FP interferometer $P_{eff} = \mathcal{F}P_{in}$) and its wavelength λ: to reach an acceptable level of noise to detect GWs, a laser operating at a wavelength
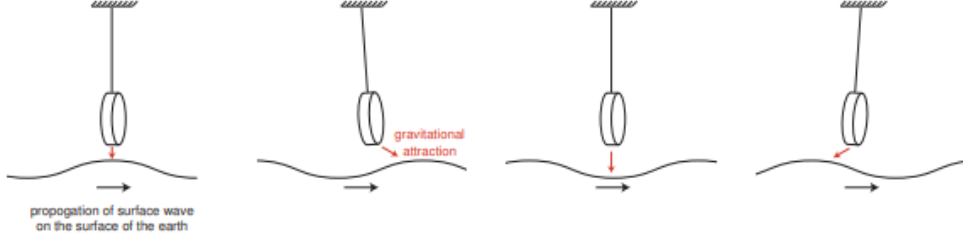
Figure 2.4. Time-lapsed fluctuating gravitational force on a suspended mass by the propagation of a surface wave on the ground.

of $\lambda \sim 10^{-6} m$ is required.

It's useful to report noise in h's unit $(\frac{1}{\sqrt{Hz}})$, in this way we can overlap noises curves to GW sources spectrum to understand our observational limits.

Radiation pressure noise Quantum fluctuation of light results also in fluctuations in the radiation pressure of the light beam and in the impulse transferred to mirrors. We can estimate this effect in a FP interferometer with a laser whose power is $P_{eff} = \mathcal{F} P_{in}$ and with a wavelength λ,

$$\sqrt{PSD_{rp}}(\nu) = \frac{1}{M\nu^2 L}\sqrt{\frac{hP_{eff}}{4\pi^4 c\lambda}} \tag{2.12}$$

where h is Planck's constant, L is the length of the interferometer and M is the mirror's mass. Note that to reduce this type of noise we can increase the mass of the mirrors or decrease the input power of the laser beam: this is an opposite request with respect to the one which allows us to reduce the shot noise.

Standard quantum limit The two previous noises are both related to the quantum nature of electromagnetic radiation. As already mentioned, the two have opposite reducing conditions: therefore, there will be an optimum value for the beam power that balances the two contributions. Let's consider a generic observational frequency ν_*, then the optimal power P_{opt} such that $PSD_{shot}(\nu_*) = PSD_{rp}(\nu_*)$ will be (considering $\eta \sim 1$)

$$P_{opt} = \pi c\lambda M\nu_*^2. \tag{2.13}$$

Therefore, using the value mentioned for the wavelength of $\lambda \sim 10^{-6} m$ and typical mirror mass of the order of $M \sim 100 kg$, we obtain a value of $P_{opt} \sim MW$ which is not too far from the power in LIGO and Virgo interferometers.

Thermal noise Thermal noise is one of the fundamental noise sources limiting interferometers over a considerable frequency range (mainly at mid-band $\nu \sim 50Hz$ to $200Hz$). It has two main contributions: normal modes of the mirror and vibration modes of the suspension fibers, i.e. the wire connecting the mirror to the last stage of the pendulum. Each mode (both for oscillation and vibration) has associated fluctuation energy equal to $k_B T$ where k_B is the Boltzmann constant and T the

equilibrium temperature of the mirror. The geometry of the whole apparatus is usually chosen in each interferometer to keep high the fiber transverse mode frequency (over the observation frequency range) and to keep low the vertical stretching mode frequency (below the observation frequency range). Some vibration modes have a displacement field extending over the region of the mirror hit by the laser beam which implies displacement noise in the detection.

About the mirror thermal noise, we can say that sources of dissipation are located in the mirror substrate and coating.[2] For both, two types of dissipation take place: structure damping and thermoelastic damping. The former is empirically known to be almost independent of frequency and can be also called Brownian noise; the latter is caused by heat relaxation in the inhomogeneous strain and is commonly called thermoelastic noise. The power spectral densities for the substrate are given by

$$PSD_{Mir\,sub\,Brown}(\Omega) = \left(\frac{2}{L}\right)^2 \frac{4k_B T(1 - \sigma_{sub}^2)\phi_{sub}}{\sqrt{\pi}E_{sub}\mathrm{w}_0\omega} \tag{2.14}$$

$$PSD_{Mir\,sub\,thermo}(\Omega) = \left(\frac{2}{L}\right)^2 \frac{16k_B T^2 \alpha_{sub}^2(1 + \sigma_{sub})^2 \mathrm{w}_0 J_{sub}(\Omega_c)}{\sqrt{\pi}\kappa_{sub}} \tag{2.15}$$

$$J_{sub}(\Omega_c) = \frac{\sqrt{2}}{\pi^{3/2}} \int_0^\infty du \int_{-\infty}^\infty dv \frac{u^3 e^{-u^2/2}}{(u^2 + v^2)[(u^2 + v^2)^2 + \Omega_c^2]} \tag{2.16}$$

$$\Omega_c = \frac{\Omega \rho_{sub} C_{sub} \mathrm{w}_0^2}{2\kappa_{sub}}. \tag{2.17}$$

The parameters σ_{sub}, E_{sub}, ϕ_{sub}, α_{sub}, κ_{sub}, ρ_{sub} and C_{sub} represent, respectively, the Poisson ratio, Young's modulus, loss angle, thermal expansion coefficient, thermal conductivity, density and specific heat of mirror substrate. The parameters w_0 and L are the beam radius at the mirror and the arm length whilst ω represents the angular frequency of the laser and Ω is the general observation angular frequency. Although the reflective coating of mirrors is several orders of magnitude thinner than the substrate, their contributions to thermal noise can't be ignored. The power spectral densities for the coating are then,

$$PSD_{Mir\,coat\,Brown}(\Omega) = \left(\frac{2}{L}\right)^2 \frac{8k_B T(1 + \sigma_{sub})(1 - 2\sigma_{sub})d_{coat}\phi_{coat}}{\sqrt{\pi}E_{sub}\mathrm{w}_0^2\omega} \tag{2.18}$$

$$PSD_{Mir\,coat\,thermo}(\Omega) = \left(\frac{2}{L}\right)^2 \frac{2k_B T^2[2\alpha_{eff}d_{coat}(1 + \sigma_{sub}) - \beta_{eff}\lambda]^2 J_{coat}(\Omega_c)}{\pi \mathrm{w}_0 \kappa_{sub}} \tag{2.19}$$

$$J_{coat}(\Omega_c) = \frac{2\sqrt{2}}{\pi} \int_0^\infty du \int_{-\infty}^\infty dv \frac{u(u^2 + v^2)e^{-u^2/2}}{(u^2 + v^2)^2 + \Omega_c^2} \tag{2.20}$$

where d_{coat} and ϕ_{coat} are the thickness and loss angle of the coating, α_{eff} and β_{eff} the effective thermal expansion and effective temperature dependence of the refractive index of the coating and λ is the laser wavelength. As we can see from

Equations, thermal noise strictly depend upon material's specific characteristics: this is the reason why the choice of materials, depending on the working temperature of mirrors, is one of the most important preliminary studies before projecting an interferometer.

For the suspension thermal noise, we can focus on the bottom stage of the pendulum because the upper stages will have negligible contributions. A simplified expression for the power spectral density is given by:

$$PSD_{therm\,pend}(\Omega) = \left(\frac{2}{L}\right)^2 \frac{4k_B T g}{m\Omega^5 l_{fib}}(\phi_{fib} + \phi_{therm\,fib})\sqrt{\frac{4\pi E_{fib}}{mgl_{fib}^2}}\left(\frac{d_{fib}}{4}\right)^2 \quad (2.21)$$

where g is the gravitational acceleration and l_{fib}, E_{fib} and d_{fib} are, respectively, the length, Young's modulus and diameter of the fiber. Therefore, ϕ_{fib} and $\phi_{therm\,fib}$ are the loss angles by structure damping and thermoelastic damping of the fiber.

As we can see from Equations, thermal noise has different complex contributions and until now we haven't taken into account the connections. The dissipations at the connection points of the suspensions were found to influence the overall noise of both mirror and suspensions. However, with a careful selection of materials and design, thermal noise can be reduced. In addition, for crystalline materials, typical properties to reduce thermal noise become better at low temperatures: this is one of the reasons to support the use of cryogenic techniques for Kamioka Gravitational Wave Detector (KAGRA) (the japanese interferometer) and future-generation detectors such as Einstein Telescope (ET).

2.3   Gravitational waves observation

Throughout this dissertation, different interferometers' names have appeared. Each of them has been useful to better understand and detect GWs signals. GWs observations are divided into runs which are characterized by different interferometers and sensitivities.[1]

First observing run O1   The First Observing Run (O1) began on September 12, 2015 and ended on January 19, 2016. The run involved the Hanford and Livingston LIGO interferometers: they detected a total of three BH-BH events including the first GW detection GW150914.

Second observing run O2   The Second Observing Run (O2) started on November 30, 2016 and ended on August 25, 2017. For the first period of observation there were only the two LIGO interferometers but on August 1, 2017, Virgo interferometer joined O2 and enabled the first three-interferometers observation of GW's signal. O2 found eight events including the first NS-NS merger GW170817. Five of them were observed with the three-interferometers configuration that enhanced the accuracy of the detection allowing a better localization of GWs' sources.

Third observing run O3   The Third Observing Run (O3) is divided into three phases: O3a was carried out from April, 1 2019 to October 1, 2019; O3b was done

from November 1, 2019 to March 27, 2020 (both of them refer to Virgo and the two LIGO interferometers); the last, O3GK started on April 7, 2020 and ended on April 21, 2020. This run involved only GEO600 (an interferometer in Germany) and KAGRA.

Future observation Fourth Observing Run (O4) and Fifth Observing Run (O5) are already under study to enhance interferometers' sensibilities. However, due to COVID-related delays, the next run (O4) wouldn't start until late 2022.

2.4 Sensitivity curves

We achieve to detect a GW's signal when the strain amplitude lies above the so-called sensitivity curve, i.e. the curve that takes into account all the different contributions of noise described previously. Each interferometer has a unique pattern of seismic (and Newtonian) noise due to different locations but they have also distinct quantum and thermal noises due to different geometries and materials for the entire setup.
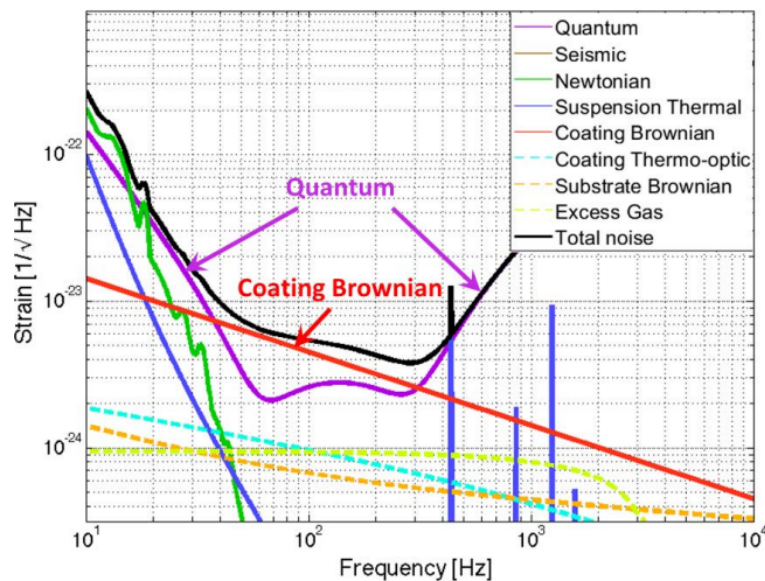
Figure 2.5. Typical sensitivity curve that includes various types of noise. The Figure represents the design noise budget for Virgo interferometer for the next observation run O4.

Figure 2.5 represents a typical sensitivity curve that takes into account all the different noise sources described in Section 2.2.
We can overlap the sensitivity curves for every interferometer (ground-based, space-based and PTA) in Figure 1.6 to understand which detector type allows us to detect which type of GW.
We can see in Figure 2.6 that the different types of detectors have a typical frequency range: this is mainly limited by geometry and materials used.

Figure 2.6. Summary of different ranges of $\sqrt{PSD}$ and frequency for different GWs sources with sensitivity curves of various types of detector.

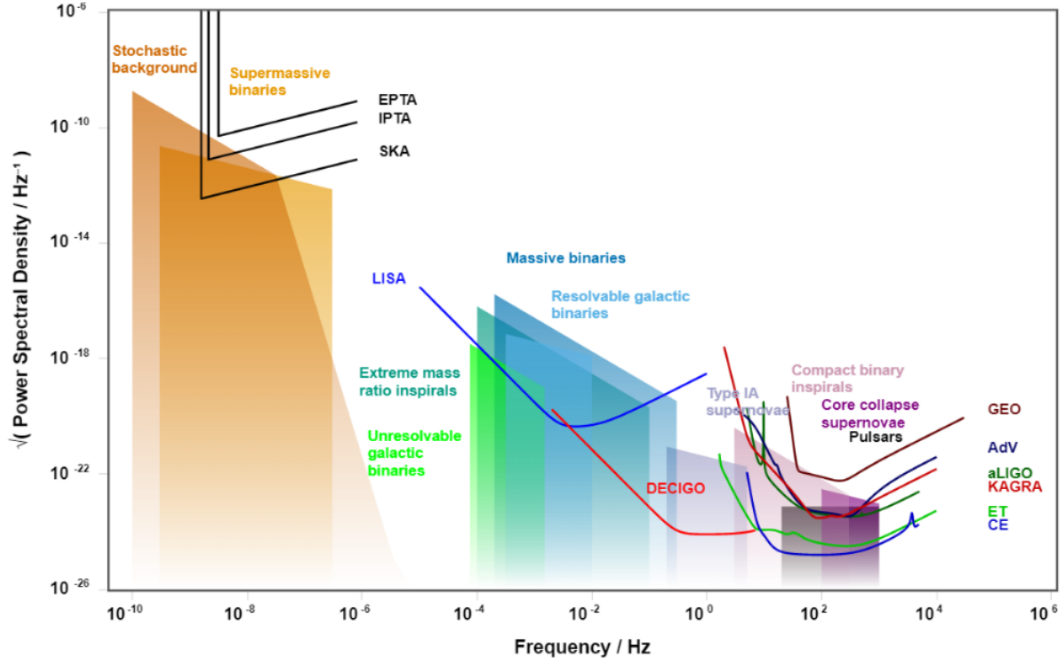The ground-based interferometers have a sensitivity curve with a frequency range above the $\sim Hz$ until $10^3 \div 10^4 Hz$: we can see that with technological upgrades during the years, the curves of the modern interferometer have better sensitivity than the previous versions. Virgo and LIGO are reported in their advanced configurations (Advanced Virgo (AdV) and Advanced LIGO (aLIGO)) which are a complete redesign of the previous interferometers with enhanced sensitivity. In the Figure, two sensitivity curves of future generation interferometers such as ET and Cosmic Explorer (CE) are also represented.

The other types of interferometers have, instead, another typical frequency range for observations: the space-based ones will observe in the range $10^{-4} \div 10 Hz$ (two examples are represented, Laser Interferometer Space Antenna (LISA) and DECi-Hertz Interferometer Gravitational-wave Observatory (DECIGO)); PTAs will work in the range $10^{-9} \div 10^{-7} Hz$ and three remarkable examples are Square Kilometer Array (SKA), European Pulsar Timing Array (EPTA) and International Pulsar Timing Array (IPTA).

2.5 Cryogenic interferometers

As already mentioned in Section 2.2, in principle, thermal noise can be reduced using crystalline materials for the mirrors at cryogenic temperatures. The first example of an interferometer that uses such a technique is KAGRA: it uses sapphire mirrors and suspensions.[2] The choice of such material is not only due to a reduction of thermal noise but it is also chosen to reduce thermal lensing on the mirror[30]. Thermal

lensing is an effect of wavefront distortion of a laser beam caused by refractive index distribution in the mirrors which have temperature distribution due to optical absorption. Since the refractive index depends on temperature, it won't be uniform over the whole of the mirror: so the wavefront distortion takes place. At cryogenic temperature, this effect is lowered mainly due to higher thermal conductivity and lower dependence of refractive index on temperature.

Another important aspect that we have to take into account is the whole suspension apparatus and its cooling system.

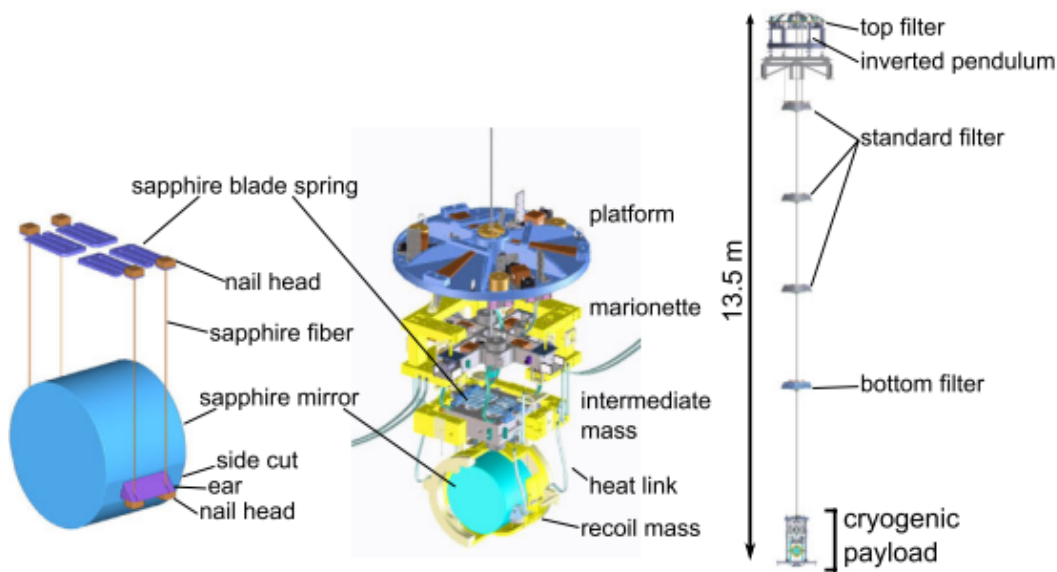## 2.5.1 Cryogenic mirror suspension

Figure 2.7. Left: sapphire suspension. Center: cryogenic payload. The recoil masses for each stage are drawn in yellow. Right: seismic isolation payload.

Because it is difficult to maintain cryogenic temperatures, only the last stages of the seismic attenuation system are cooled down: mirror, suspensions and seismic attenuation stages at cryogenic temperature are called cryogenic payload. Sapphire mirrors are suspended as shown in the left-hand panel of Figure 2.7. Fibers are made of sapphire and they are connected to the mirror by means of ears which can be seen in the Figure. These ears are attached to a flat area on the mirror via the hydro-catalysis bonding technique, i.e. a bonding technique particularly suitable for cryogenic temperatures. Each mirror is suspended with four fibers which have a cubic nail head at each end. The upper surface of the nail head at the bottom of the fiber is attached to the bottom of the ear with a gallium foil, which is used for bonding. On the upper side of the fiber, the lower surface of the nail head is attached to sapphire blade springs. These springs are fixed to the intermediate mass and they allow to reduce further the resonant frequency of the vertical stretching modes. Sapphire blade springs complete the bottom part of the 4-stage cryogenic payload: it can be considered a monolithic sapphire system because all of its parts are made

of sapphire and connections are realized with appropriate bonding techniques. This allows for reducing dissipations in connection points which, as already mentioned in Section 2.2, would be crucial noise sources.

Intermediate mass is attached to the marionette which has a "+" shape and allows for adjusting the position and alignment of the sapphire mirror. The top stage of the cryogenic payload is the platform, it is connected to the bottom filter, i.e. the last stage of the room temperature part, and, by means of cantilever springs, allows attenuating vertical vibrations (see the central panel in Figure 2.7).

The room temperature seismic attenuation system is similar to superattenuator mechanism in Virgo: KAGRA's attenuation is composed of five filters in series supported by an inverted pendulum, as we can see in the right-side panel of the Figure. The main difference compared to Virgo's is that KAGRA has an underground facility so it isn't necessary to build a tall support structure for the inverted pendulum: tunnels are excavated above each mirror's position so, exploiting the site, shorter and more rigid support structures can be used.

2.5.2 Pulse Tube

A refrigerator used to reach cryogenic temperatures is often called cryocooler. Among the various types of cryocoolers that have been invented, the Pulse Tube (PT) cryocoolers are usually used in vibration-limited applications because they can be made without moving parts on the low-temperature side of the device. There are many variants of PTs, the fundamental mechanism of many of them can, however, be described starting from the Stirling-type single-orifice PT, i.e. one of the simplest types[6]. Figure 2.8 shows a simple schematic diagram of this cryocooler.
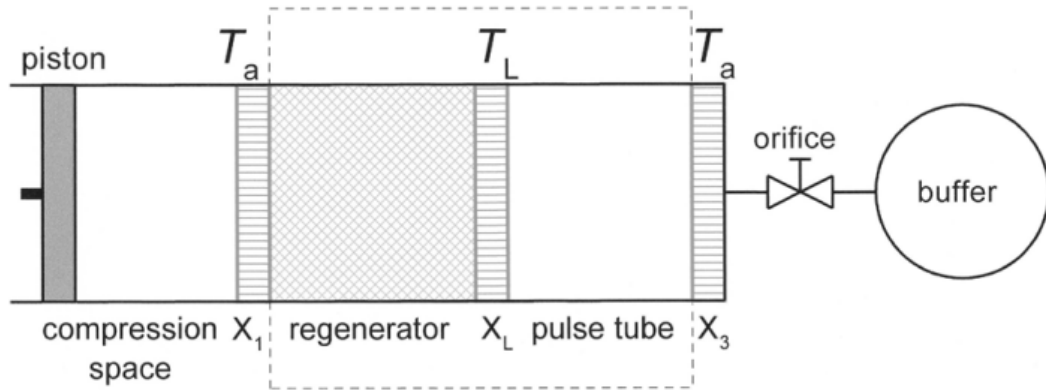
Figure 2.8. Schematic diagram of a Stirling-type single-orifice PT. From left to right: piston, after cooler (X1), regenerator, low-temperature heat exchanger (XL), pulse tube, second room temperature heat exchanger (X3), orifice, buffer. The dotted rectangle represents thermal (vacuum) insulation.

Driven by the piston, the gas moves back and forth and the pressure in the pulse tube varies. The working fluid is helium at 10 to 30 bar. In the pulse tube, we can distinguish three types of particles. Particles that, during the cycle, move in and out

through the cold heat exchanger (at low-temperature T_L); particles that move in and out via the hot heat exchanger (at room temperature T_a); particles that never leave the pulse tube. The buffer on the right side of the Figure is characterized by gas at constant pressure: when the pressure in the pulse tube varies, the orifice controls the gas exchanging between the buffer and pulse tube. On the left side of the vacuum insulation, the gas flowing through the regenerator is controlled by the piston and the two heat exchangers at T_a and T_L. The cooling power is determined by the dissipation in the orifice-side of the setup.

Other types of PT are the Gifford-McMahon (GM) PTs: they have the piston and compression space uncoupled from the remaining parts and connected via a rotating valve that controls the pressure and gas exchange. The disadvantage of both the design described is that the cold spot is in the middle of the cooler. Many applications require cooling produced at the end of the cooler: this is the case of the U-shaped cooler obtained by bending the PT design. Moreover, a common shape of PTs is the cylindrical geometry: the PT can be constructed in a coaxial way so that the regenerator becomes a ring-shaped space surrounding the tube.

The lowest temperature reached with a single-stage PT is usually $\sim 10K$. However, we can use a PT to precool one another: we can, then, create a multi-stage PT that can reach a temperature below $2K$.

2.5.3 Cooling system
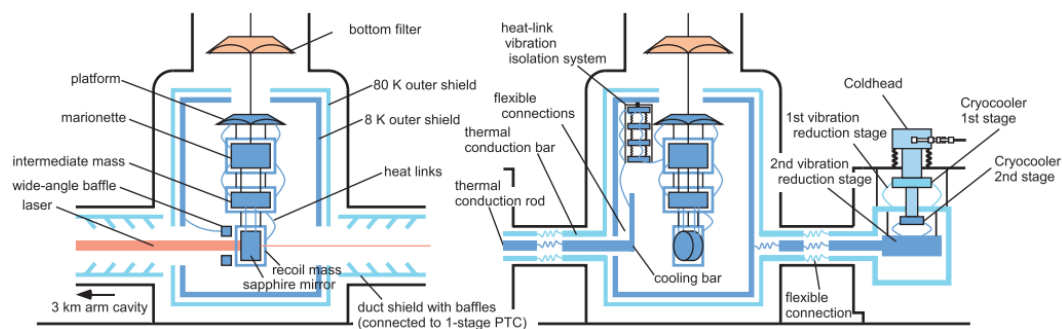
Figure 2.9. Schematic of the cooling system. In the left-hand panel, a side view of the cryostat from the direction orthogonal to the arm is represented. On the right-hand side, the view is at an angle of 30° from the direction of the left-hand side panel. There is another (omitted) cryocooler on the left-hand side of the right-hand panel that cools down the cooling bar.

To cool down a single cryogenic payload, four 2-stage PT cryocoolers are used. Thanks to a particular mechanical design adopted for the cooling units, the vibrations injected by the cryocoolers into the cryostat can be greatly reduced. Moreover, this cryogenics implementation in the underground environment is significantly easier with respect to cryofluid cooling.

Figure 2.9 describes typical features that allow the cooling of each KAGRA's mirror. The cryogenic payload is inside a cryostat, i.e. the vacuum chamber that covers all the cryogenic parts. Inside the cryostat, two radiation shields are accommodated to

isolate the payload from the $300K$ environment's radiation. The outer shield is the $80K$ one, whilst the inner is the $8K$ one (these temperatures refer to the average temperature of shields): the former is connected to the first stage of all the four PTs, the latter, instead, is connected to the second stage of two PTs. The second stage of the two remaining PTs is used to extract heat from the cryogenic payload by means of two cooling bars. The right-hand side of Figure 2.9 represents a view of the cryostat with an angle of 30° from the direction orthogonal to the arms. With that perspective we can see two of the four PTs: one with the second stage connected to the inner shield and the other (omitted in the Figure) connected to the cooling bar used to cool down the payload.

To let the laser beam enter, the cryostat and the shields need holes situated along the arms' directions: $300K$ radiation will enter from there. Additional shields, duct shields, are then inserted inside the vacuum chamber that will be present also along the laser path to maintain the vacuum condition. A black coating is applied to the inner surface of the duct shield to increase the absorption of $300K$ radiation; several baffles with the same coating are further equipped inside to efficiently block the propagation of the same radiation. The baffles also help in reducing the influence of the laser light scattered from the sapphire mirror. Additional single-stage PTs are used to cool the duct shields.

All the PTs are mounted on a vibration reduction system which is rigidly connected to the ground to isolate vibrations of the cold heads. However, to further reduce this vibrational noise, 99.9999% purity (6N) aluminum heat links are used in various connection points. T. Yamada[35], [34] reports a full characterization of these types of heat links. The single heat link is formed by seven secondary twists in parallel gathered by two terminals made of 99.999% purity (5N) aluminum at both ends. Each secondary twist is made by seven primary twists which consist of seven 6N aluminum (Al) thin wires twisted together (see Figure 2.10).

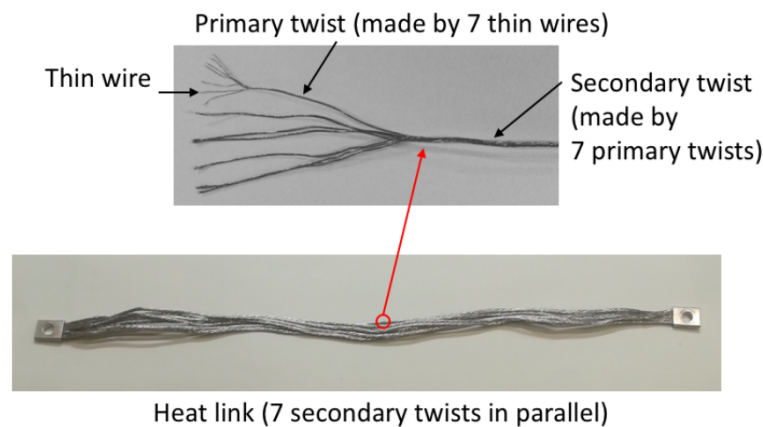**Figure 2.10.** Detail of the heat link[34]. A single heat link is composed by $7 \times 7 \times 7$ 6N aluminum thin wires. End terminals are made of 5N aluminum.

Heat links are one of the crucial parts of the whole cryogenic apparatus because they have to efficiently conduct heat and reduce vibrations in the payload. The choice of the material is just forced by these problems: heat links require to be

soft and with high conductivity. 6N aluminum has a low Young's modulus (e.g. compared to copper's) and very high thermal conductivity, especially at cryogenic temperatures. In Figure 2.9 we can see that such heat links are used in all the four PTs to isolate each radiation shield and also the cooling bar: the same heat links are also used as heat connection between the cooling bar and the payload itself, that is connected in the marionette stage. Additional heat link vibration isolation systems are used in this last connection.

KAGRA has also another important feature: it is an underground interferometer. This will reduce seismic and Newtonian noise.

For all these reasons, KAGRA is a good starting point to settle the basic characteristics of future-generation detectors such as ET.

The next Chapter will introduce ET with its characteristic structure and science cases that will be achieved with an enhanced design noise curve. Similarities and differences to KAGRA will also be described in detail.

Chapter 3

Einstein Telescope

ET is a proposed underground infrastructure to host a third-generation GW observatory. ET will be a third-generation telescope because it will have particular characteristics that will enhance its sensitivity and which will distinguish it from first-generation (such as LIGO and Virgo) and second-generation (such as aLIGO, AdV and KAGRA).

3.1 Scientific targets for ET observatory

The importance of third-generation interferometers can be valued considering the observation targets that can be achieved due to the enhancement of sensitivity and extension of the frequency range. We can divide possible ET observation targets into two main categories which include various items[9]:

- Astrophysics

  - black hole properties: origin (stellar or primordial), evolution and demography;

  - neutron star properties: interior structure and demography;

  - detection of new astrophysical sources of GWs: core-collapse supernovae and isolated neutron stars.

- Fundamental physics and cosmology

  - Nature of compact objects: near-horizon physics, test of no-hair theorem, exotic compact objects

  - dark matter: primordial BHs, axion clouds;

  - dark energy and modified gravity on cosmological scales;

  - stochastic backgrounds of cosmological origin and high-energy physics (inflation, phase transitions, cosmic strings).

Let's briefly discuss why all these goals could be achieved with ET.

3.1.1 Astrophysics

Black hole binaries   Section 2.3 describes all the remarkable observations that the existing interferometers have made during the various observation runs. ET will crucially extend the observable range of BHs: for a total mass of the system between a few tens to a few hundred solar masses, i.e. the mass range of BH binaries revealed by existing detectors, ET will be able to detect their coalescence up to redshift $z \sim 20$ and beyond. The corresponding rates will be in the order of $10^5 - 10^6$ events per year which yield to a census of the population of BHs across the whole epoch of star formation and beyond. This would lead to the determination of features such as masses of the first metal-poor progenitor stars. ET will also extend the mentioned BH mass range: sources of several hundreds of solar masses could be detected up to redshift of order $z \sim 10$ or more, whilst sources of several thousand solar masses could be detected up to $z \sim 1 - 5$. This could provide the first clear evidence for the existence of BHs in this mass range and would allow us to study the possibility that they are the seeds of supermassive BHs in the center of galaxies. ET would extend the observing mass range also on the low-mass side. It could detect up to $z \sim 0.5 - 1$, the coalescence of hypothetical binary BHs with a total mass of one solar mass order.
This wide range of possible observations with such a high rate would be useful to disentangle the contribution of BHs of stellar origin from that of possible primordial ones.

Neutron stars   In NSs, intense gravity compresses matter to several times the density of an atomic nucleus. Near the surface of a NS, neutron-rich nuclei and free electrons dominate, while at higher densities towards the interior, the nuclear structure dissolves into a uniform liquid of neutrons. In the cores of NSs yet more exotic states of matter may emerge, such as condensates of particles containing strange quarks. Properties of the transition between nuclear and quark matter have been a key question in subatomic physics. The signal GW170817 demonstrated that useful limits on the NS's tidal deformability, i.e. a characteristic parameter that depends on the properties of matter in their interior, could be extracted from the inspiral part of the GW signal. To determine in detail the nature of the matter in NS interiors, tidal deformability with an order of magnitude higher accuracy is required. In addition, these measurements must be obtained for a population of NSs spanning a wide range of masses. Both can be achieved with ET which will detect NS-NS coalescences up to a rate of 7×10^4 per year.

New astrophysical sources   With the enhancements in sensitivity and frequency range, brand new GW sources could be detected.
The possible GW signal emitted in a core-collapse supernova would be extremely weak, e.g. its energy would be of the order of $10^{-9} M_\odot c^2$ compared to $\sim 3 M_\odot c^2$ released in GW150914. In addition, the galactic rate of these types of supernovae is small (~ 1 event per 30 years); ET will extend the reach to our galactic neighborhood so that the expected rate can be increased. The enhanced frequency range of ET design is further very well suited for detecting this type of signal using promising

neural network algorithms, which could recognize particular features of the signal. The detection of GWs emitted in the core-collapse and post-collapse would reveal the inner mechanism of supernovae explosions.

A spinning NS, isolated or in a binary system, can emit continuous GWs if it has a certain degree of asymmetry (see Section 1.4). No continuous GWs signals have so far been observed by existing interferometers. The maximum degree of deformation that NS can sustain depends on the equation of state. The maximum value for ellipticity is $\epsilon_{MAX} \sim 10^{-6}$ for a standard equation of state whilst it goes up to $\epsilon_{MAX} \sim 10^{-4} - 10^{-3}$ for exotic objects. Simulations for two proposed ET configurations with $5yr$ of observing time show that ET will be sensitive to ellipticities of the order of a few times 10^{-10} for the nearest millisecond pulsars and $10^{-6} - 10^{-7}$ for young pulsars.

Possible burst signals from NSs could also be observed.

3.1.2 Fundamental physics and cosmology

A third-generation detector will allow us to measure the strong-field dynamics at the source with higher accuracy than existing interferometers. One of the main reasons for that is the much larger detection rate: informations from multiple sources can often be combined and the accuracy of common observables tends to improve with the square root of the number of detections.

Test of General Relativity Black holes are one of the most extraordinary predictions of General Relativity. It gives detailed and specific predictions on the nature of BHs that interferometers such as ET will be able to test. The no-hair theorem states that, in a stationary situation, a BH is determined by just two numbers: its mass and its spin (plus the electric charge, which however is not relevant in an astrophysical context because it is quickly neutralized). When a BH is perturbed, it reacts relaxing to its stationary configuration by oscillating in a superposition of Quasi-Normal Modes (QNMs), which are damped by the emission of GWs. Since the whole spectrum of frequency and damping time of the QNMs depends only on the two parameters, a stringent test of General Relativity can be performed by measuring independently at least three modes. ET will detect a number of BHs binaries of $\sim 10^5 - 10^6$ per year, out of these a large fraction will have a detectable final inspiral signal. If we request this type of signal sufficiently strong to be able to disentangle the different modes, we can obtain a value of $20 - 50$ events per year with a redshift up to $z \sim 2$.

The observation of QNM could also potentially lead to the discovery of different types of compact bodies; various exotic objects have been proposed so far such as boson stars, stars composed of dark matter particles, etc. Their hypothetical inspiral will generate a GW with particular characteristics.

Nature of dark matter From cosmological observations we know that about 25% of our Universe is made of Dark Matter (DM), i.e. matter that does not have electromagnetic interactions and whose existence is only inferred through gravitational attraction. Because we don't have a clear understanding of DM nature, ET's observations will be useful in different ways. Dark matter could be, indeed,

composed, at least in part, of primordial black holes: these could be seeded by fluctuations generated during the last stages of inflation, which then collapsed in later epochs during transition phases. The possibility of ET observing stellar-mass BHs mergers at a redshift of $z \sim 10 - 20$, before any stellar formation, would be crucial to distinguish a primordial origin.

Ultralight bosons have been proposed in various extensions as dark matter candidates. If their Compton wavelength [1] is comparable to the horizon size of BH, they can extract rotational kinetic energy from the BH to feed the formation of bosonic clouds. These clouds annihilate over a much longer timescale than their formation, through the emission of GWs which could be detected either directly or as a stochastic background.

Nature of dark energy   Besides the 25% of the Universe composed of dark energy, we can consider that visible matter is only 5%: the remaining 70% is currently attributed to Dark Energy (DE), i.e. a form of energy that formally produces a negative pressure and therefore cannot be identified with any known or unknown type of matter. Informations about dark energy directly derive from cosmological parameters such as H_0 or ρ_0 which are the Hubble parameter and the closure energy density. These parameters are related to the luminosity distance d_L and redshift of the sources. Observations performed with electromagnetic waves can infer the redshift of a source but the information about luminosity distance would be more difficult to obtain: ideally, it is required the existence of standard candles, i.e. a class of sources whose intrinsic luminosity is known.

GW of inspirals directly carries the information on the luminosity distance: in this context, coalescing binaries are called standard sirens (GW analog of standard candles). An ideal situation is a joint GW-electromagnetic detection as was the case of GW170817.

For a third-generation interferometer, given the expected huge number of detections, very high accuracy on cosmological parameters could be achieved. ET will also have access to standard sirens at a much larger redshift. This information can be also used to test the possible effect of modified gravity at cosmological distances, which would change the standard cosmological model.

Stochastic background   GWs were decoupled from the primordial plasma before the Planck epoch characterized by an energy of the order $E \sim 10^{19} GeV$: this corresponds to energy far exceeding that accessible to particle accelerators. The weakness of the gravitational interaction implies that the detection of GWs of the GWB would provide us an uncorrupted snapshot of the earliest Universe.

While signals generated during the inflationary expansion are expected to be too low to be detected by ET, other inflation-related mechanisms could have produced observable signals. First-order phase transitions and cosmic strings are also other potential sources that could be detected by ET at least by means of their strongest signals which could fall within the sensitivity curve.

---

[1]Compton wavelength is a quantum mechanical property of a particle. It is equal to the wavelength of a photon whose energy is the same as the mass of the particle. $\lambda = \frac{h}{mc}$ where h is the Planck constant.

3.2 ET structure

In order to achieve the sensitivity that the ET project aims for, it will be necessary to exploit all state-of-the-art technologies and drive them to their technical limits [9]. The first upgrade to sensitivity will be reached by increasing the size of the arms beyond the size of currently available instruments: in their final configuration, the arms will have a length of $10km$, way more than $3km$ or $4km$ respectively of AdV (or KAGRA) and aLIGO.

The angle between the arms will be changed too. ET will consist of three nested detectors with an angle between arms of $60°$ compared to the $90°$ of the typical L-shaped ones.
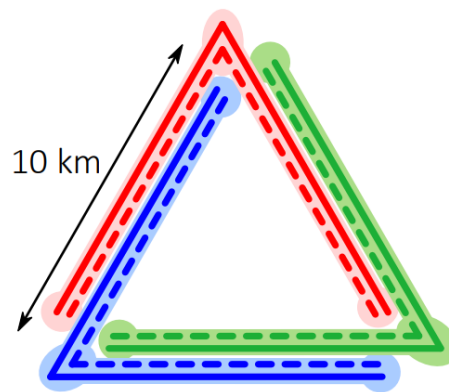

Figure 3.1. Final geometry of ET with three nested detectors with arm length of $10km$.

The final configuration will be like the one represented in Figure 3.1. In contrast to the traditional L-shaped geometry, this arrangement is equally sensitive to both GW's polarization.

Each detector will then have two specific interferometers, one specialized for detecting low-frequency GWs (ET Low Frequency (ET-LF)) and the other for high-frequency range (ET High Frequency (ET-HF)). The overall frequency range covered will be from $3Hz$ to several kHz. Each interferometer will be the simple FP Michelson. This setup will simplify also the choice of the parameters for the construction.

To achieve better sensitivity at high frequencies, the light power in the arms needs to be increased (shot noise will be reduced) but this will increase radiation pressure noise that will limit the observation at low frequencies: with two interferometers, observing at different frequency ranges, we can choose parameters independently for the two to optimize their sensitivity. We will not be limited by the quantum limit and we can consider individually the two noises. This configuration which split every single detector into two complementary interferometers is called xylophone arrangement and leads to a sensitivity curve represented in Figure 3.2. The Figure report in red the global sensitivity curve for a single detector with $10km$ arm length and an angle of $90°$ between the arms. Such a curve is represented to better compare the existing and planned detectors. ET will have an angle of $60°$ and its resulting sensitivity will depend on the source location in the sky and its orientation: on average, the sensitivity of the triple $60°$ detector is slightly better than a single,
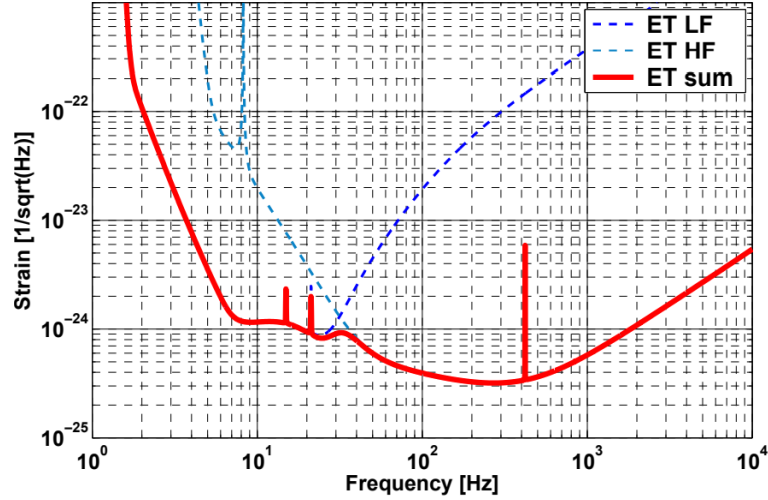
optimally oriented 90° one.

Figure 3.2. Sensitivity of ET in the xylophone configuration. The sensitivity of the ET-LF
is shown in the dashed dark blue curve, the ET-HF one in light blue color. The sum of
the two is represented in red. This sensitivity curve is for a single detector with $10km$
arm length and an angle of 90°.

ET-HF will contribute to the total sensitivity curve in the frequency range from
about $30Hz$ to several kHz. It will operate at room temperature and will use fused
silica mirrors and suspensions: it will have a light power of about $3MW$ in the
interferometer arms.
ET-LF aims to extend the frequency range from $3Hz$ to $30Hz$ which will open the
search for brand new GW sources compared to existing interferometers. To reach
such a low frequency, it will operate at cryogenic temperatures of $10K - 20K$. The
mirror and the suspensions of the interferometer will be made of silicon: it has
excellent mechanical and thermal properties at cryogenic temperatures and is easily
available in relatively high quality due to the large market of semiconductors. This
choice necessitates moving to a longer laser wavelength of $1550nm$ because silicon is
not transparent at the wavelength of $1064nm$, i.e. the laser wavelength used in the
existing L-shape interferometers. The light power in the arms will be $18kW$ which
is two orders of magnitude lower than that of the ET-HF: this drastically reduces
the contribution of radiation pressure noise.
The enhancement of the arm length is crucially to increase the sensitivity but it will
have a strong impact on the construction cost: ET will be an underground facility,
so also excavation cost of such long arms needs to be considered. However, due
to their similar design, ET-HF and ET-LF will share common tunnels. The full
layout of the central part of the two interferometers of a single detector is reported
in Figure 3.3.
Whilst the two interferometers share the same arm cavity, they have different
locations, named caverns, where BSs, ITMs and other optical parts are situated.
The Figure represents in blue the components of the low-frequency interferometer
(in cavern A) while in red are reported the high-frequency ones (in cavern B). ETMs
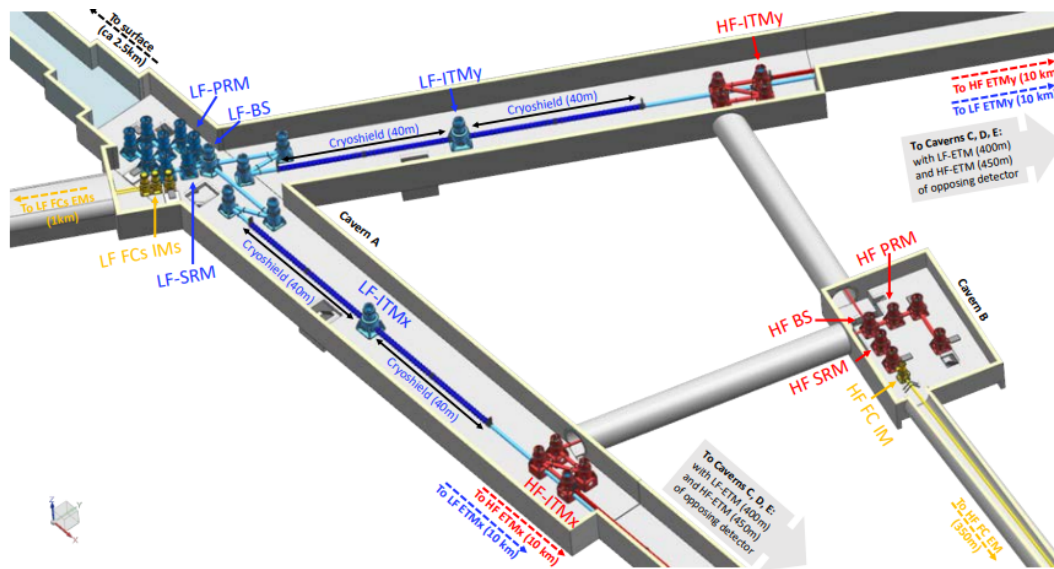
Figure 3.3. Schematic view of the central part of the two interferometers of a single detector in ET. In blue are reported the components of the ET-LF interferometer while in red the ET-HF ones. Dashed arrows indicate the directions where end test masses are located.

of the two interferometers described are at $10km$ of distance as reported by the dashed arrows in the representation. Informations about ETMs of the other two detectors are also present in the Figure.

The extension of the detection bandwidth of ET to the low-frequency region starting from $3Hz$ requires improved seismic attenuation than existing detectors. The underground facility helps in lowering such type of noise, as it applies for KAGRA, but also the system of filter above each mirror needs some improvements. Detailed studies have been made and the conclusion was that a viable solution would be a longer ($17m$ instead of $\sim 10m$) version of the current Virgo superattenuator (see Figure 2.3) with the same number of passive isolation stages. It is expected that this structure can be reduced in height by introducing an improved seismic platform at the top and removing some filters. As already mentioned for KAGRA, a shorter structure would be more rigid and would reduce the cost.

3.3 Cryogenics

Let's now focus only on ET-LF describing its cooling system and particularities that will differentiate it from KAGRA.

In order to limit thermal noise, it is necessary to cool at cryogenic temperature the four test masses of each interferometer. The heat will be mainly extracted from the mirror via the suspension fibers, mostly when temperatures are already low that radiation would become ineffective. In the same way as KAGRA, heat links used to cool down the payload would be attached to the marionette. The whole payload is suspended from the superattenuator which will attenuate seismic noise up to a few

Hz (allowing ET-LF to have a frequency range for observation starting from $3Hz$). Connection via these heat links would be therefore crucial to preserve mechanical isolation between the mirror and cooling system but also to guarantee an efficient thermal link to cool down the payload.

The payload is housed in the cryostat which has two thermal shields: the inner that will have an average temperature of $4K$ while the outer of $40K$. On the upper side of the cryostat, there will be an aperture to allow the $Ti - 6Al - 4V$ thin rod to connect the payload to the superattenuation system above. The base of the main tower that includes the cryostat with the payload and the superattenuator is connected to a couple of ancillary cryostats as shown in Figure 3.4.

The right-side cryostat in the Figure will host a sufficient number of pairs of pulse tubes which will provide the refrigeration power to keep the mirror and the inner shields at cryogenic temperature. A large fraction of the heat extraction path is through a 99.9995% purity (5N5) Al bar. The heat extraction path will be of the order of $\sim 20m$ in length and to reduce vibrations of the PTs units, particular heat links will be used to complete the heat path as it was done for KAGRA (see Section 2.5.3). Additional attenuation systems will be present in the innermost shield of the payload cryostat and will be connected between the marionette and the cooling bar. Although KAGRA's heat link design is well suited for such heat extraction, ET's design is still under study to create something easier but with the same efficiency: a prototype will be presented in the next Chapters of this dissertation.

The main heat inputs into the cold mirror are the thermal radiation coming from the inner surface of the cryostat and heat load due to the absorption of a small fraction of the laser light resonating in the FP cavities. The former will be reduced with shields and typical multi-layer insulation, e.g. multi-layer of porous (self-vented) Mylar sheets aluminized on one side; the latter can be, instead, estimated considering the laser power for ET-LF of $18kW$ and a reference value for the absorption coefficient of the mirror coating, an approximate value of $0.1W$ will be absorbed from laser light.

About the payload design, different models are still under study to choose the design that better satisfies all the requirements both optical (geometrical constraints due to beam size and power) and thermal (constraints for the mass and suspensions). One of the possible schemes is that represented in Figure 3.5.

This design is similar to that used in AdV[3]. In this particular arrangement, the cryogenic payload is suspended to the room temperature superattenuator by means of the steering filter. Below there's the typical marionette used to hold the monolithic structure composed of the mirror and the suspensions. The whole payload is surrounded by a cage, suspended itself to the steering filter, which is designed to serve as a reaction mass. It is used to apply control onto the payload by means of suitable actuators.

3.3.1 Amaldi Research Center

Amaldi Research Center, located at Sapienza University in Rome, will be a facility to test and optimize cryogenic configurations for ET-LF: it's currently under construction but it will be completed within the end of 2022. It will host a real-size test payload with thermal inputs from thermal shields and laser tubes. There will
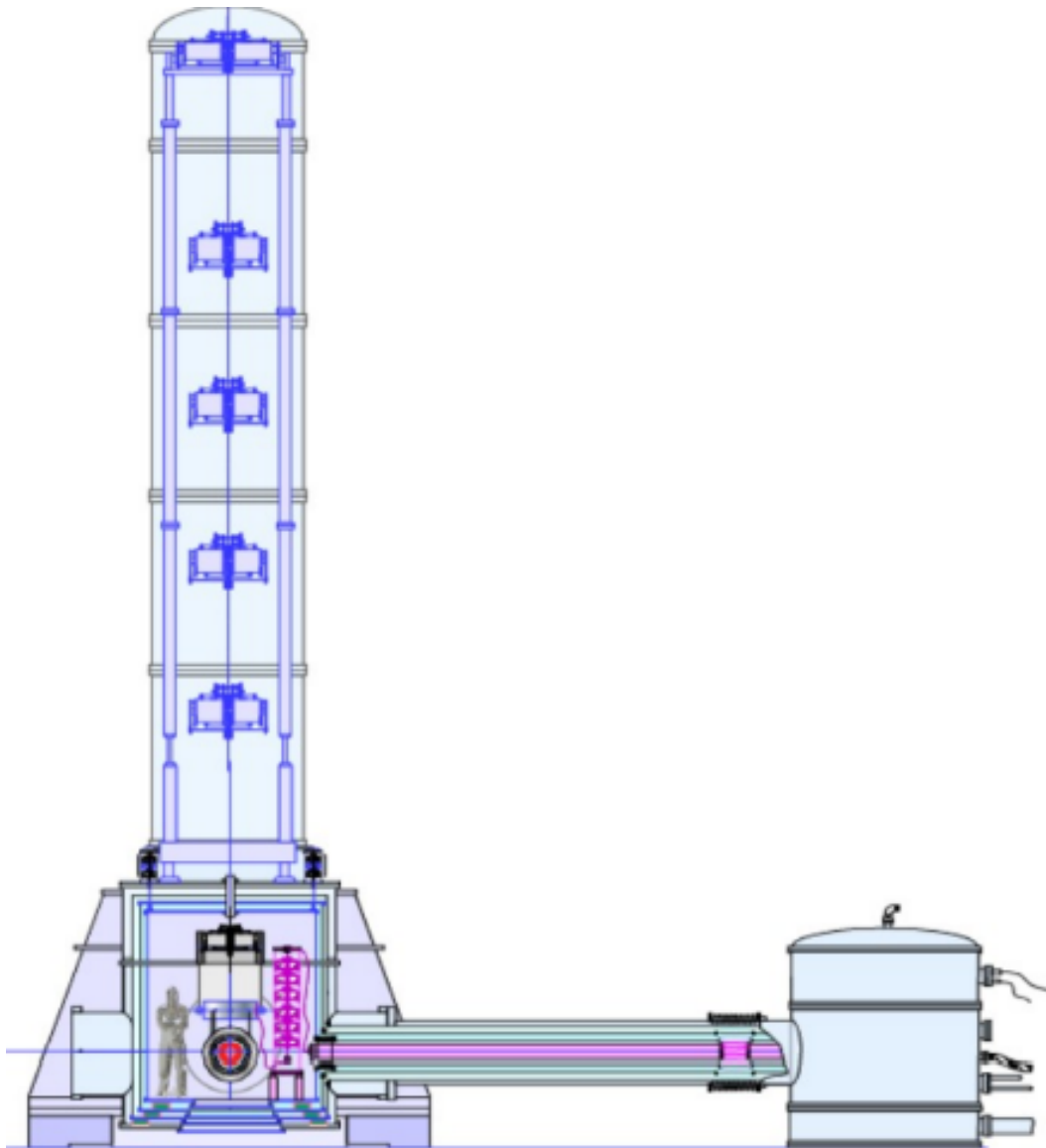
Figure 3.4. Scheme of the cryostats and heat link needed to cool down each test mass in ET-LF. Inside the inner cryogenic shield, an ancillary mechanical attenuation system has to be installed to further reduce the vibrations coming from the ground and from the cryogenic line.

be the possibility to test various radiation cooling with different coating for shields or hypothetically super insulation schemes. The project for the test cryostat and payload is represented in Figure 3.6.

We can recognize the same payload structure reported in Figure 3.5. It will be hung to a suspension gear that is a high torque stepper motor similar to the ones already used in Virgo (at the top of the superattenuator). Inside the cryostat, there will be three different shields to reduce radiation from room temperature surfaces: these can also be changed or adapted to test different cooling schemes, e.g. with
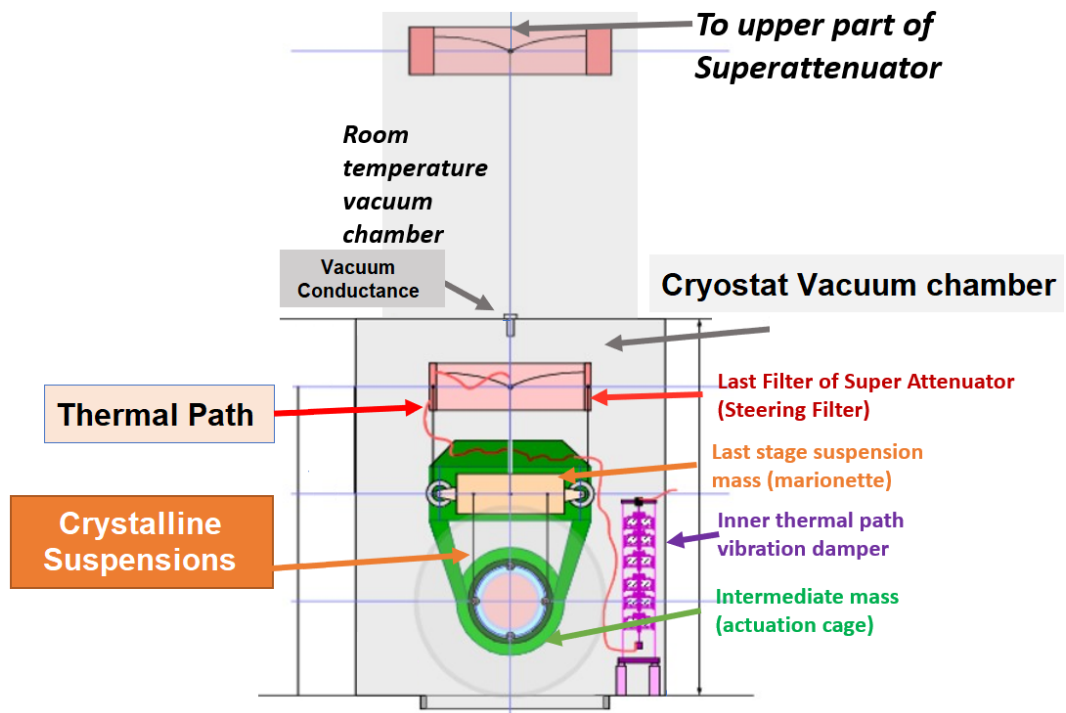
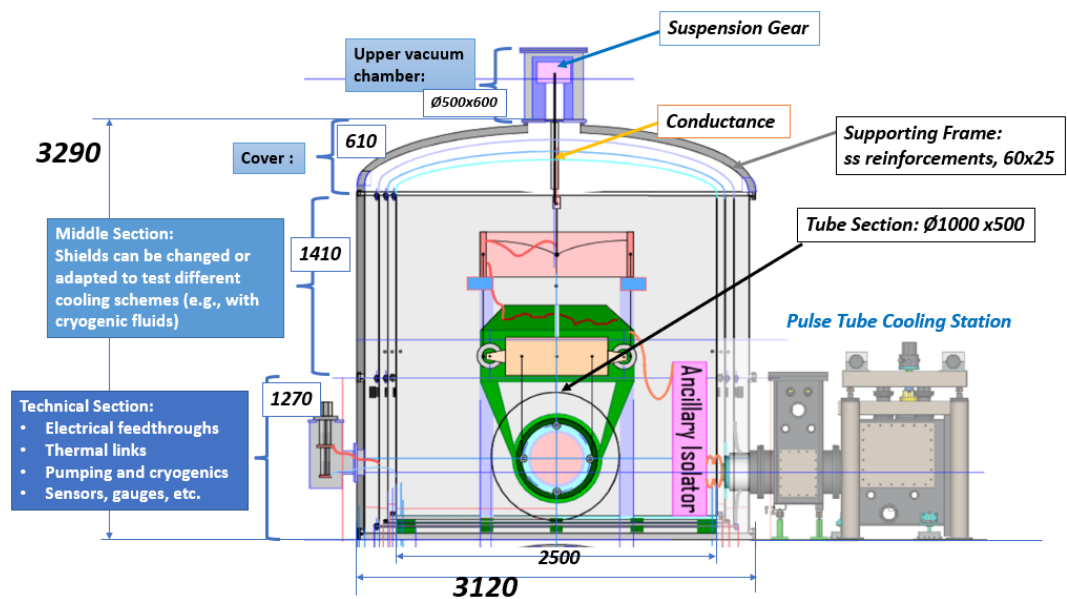**Figure 3.5.** Scheme of a possible design of ET's payload.(Courtesy of Prof. P. Rapagnani.)

Figure 3.6. Project of test cryostat, payload and cooling station which will be hosted in Amaldi Research Center, Rome. All the measures are in mm.(Courtesy of Prof. P. Rapagnani.)

cryogenic fluids. The ancillary isolator reported in the Figure will be inspired to

the heat link attenuation system, already present in KAGRA [34]. However, it has to be significantly revised because, in the case of KAGRA, the attenuator is used to reduce only general vibrations above $10Hz$ while in ET it has to attenuate them starting from $0.5Hz$. The pulse tube cooling station will be constituted by two PTs connected to a cooling bar, whose vibrations will be damped by heat links that will connect also the payload.

Thermal simulations of the whole PT cooling station and heat links will be discussed in the next Chapter and will have fundamental importance to set the last bases for the construction of the whole test cryostat and payload.

Chapter 4

Pulse tube cooling station

The fundamental part of the whole cryogenic system is the PT cooling station which has to generate sufficient refrigeration power to cool down the payload through the heat path. Amaldi Research Center will have the possibility to test this cooling station on a test payload. It has been planned to study the first prototype of the cooling line to validate the design and to go further towards the development of the ET's cryostat where four units of such a kind could be adopted. Before the end of the facility's construction, thermal simulations can, then, be performed on the whole cooling station to test the relevance of heat links. This Chapter will introduce in detail the scheme of all the parts of the cooling station and the software used to perform the simulations, after a first introduction on the heat transfer.

4.1 Theory of heat transfer

Let's briefly discuss fundamental laws that govern heat transfer. Three different mechanisms can take place to transport heat, namely conduction, convection and radiation[22]. Conduction and radiation are the main mechanisms of heat transfer that we have to consider to study the cooling of the whole cryogenic facility; conversely, due to the ultra-high vacuum condition inside the cryostat, convection is not significant. Convection, indeed, occurs when heat is transferred between a solid surface and a fluid, or between different fluid regions, due to bulk fluid movement.
The exact comprehension of conduction and radiation can also let us understand the crucial role that the choice of materials for heat links will have, especially in the low-temperature regime.

4.1.1 Conduction

Conduction is the heat transfer mechanism that occurs from one part of a solid body (or fluid) to another, or between bodies in contact, without any movement on a macroscopic level.
In a one-dimensional case, considering heat flowing along the x-axis, the conduction heat transfer rate is governed by Fourier's law,

$$P_{cond} = \frac{dQ}{dt} = -\kappa(T)A(x)\frac{\partial T}{\partial x} \tag{4.1}$$

where $\kappa(T)$ is the thermal conductivity of the material, $A(x)$ is the cross-sectional area through which heat (Q) is transferred per unit time and P_{cond} is the heat flow rate, in terms of power (units of W). In multidimensional problems, the partial derivative in Equation 4.1 becomes a gradient of temperature and P_{cond} a vector of the three components in the x, y and z directions.

The negative sign in the Equation refers to the fact that the heat is transferred from the hot side of a body to the cold side, so through a negative temperature gradient. For a steady-state one-dimensional problem, the temperature gradient can be approximated by the temperature difference between two points divided by their distance Δx, so, if the area is constant in Δx, Fourier's law becomes:

$$P_{cond} = -\kappa A \frac{\Delta T}{\Delta x} \tag{4.2}$$

in which $\kappa(T)$ is considered constant in the temperature range fixed by ΔT.

We can introduce a helpful parameter, the thermal resistance R, which is an indicator of the ease of heat transfer through conduction. Thermal resistance is analogous to the concept of electrical resistance. In an electrical system, the current flowing between two points, 1 and 2, is described by Ohm's law:

$$I = \frac{V_1 - V_2}{R_e} \tag{4.3}$$

where I is the electrical current, $V_1 - V_2$ is the potential difference and R_e is the electrical resistance.

In the case of heat conduction, a similar expression can be derived starting from Equation 4.2,

$$P_{cond} = \frac{T_1 - T_2}{R} \tag{4.4}$$

where the heat transfer rate is considered analogous to the electrical current; in this case, the temperature difference $T_1 - T_2$ represents the driving potential for the heat flow. Comparing Equations 4.2 and 4.4, we can obtain the resistance

$$R = \frac{\Delta x}{\kappa A}. \tag{4.5}$$

In complex systems, such as composite bodies with different materials, we can compute an equivalent thermal resistance treating them as analogous to equivalent electrical circuits. Through the same analogy that stands for the fundamental law of heat conduction, we can assume a composite body as assembled with a number of multiple thermal resistance in series and/or in parallel. The resulting equivalent thermal resistance can then be computed following the same expressions that are used in the electrical case:

$$R_{eq}^{series} = \sum_i R_i \qquad\qquad R_{eq}^{parall} = \left(\frac{1}{\sum_i R_i}\right)^{-1}. \tag{4.6}$$

A practical example is that reported in Figure 4.1. The resulting resistance of the whole system can be expressed as:

$$R_{Tot} = R_1 + \left(\frac{1}{R_2} + \frac{1}{R_3}\right)^{-1} + R_4. \tag{4.7}$$
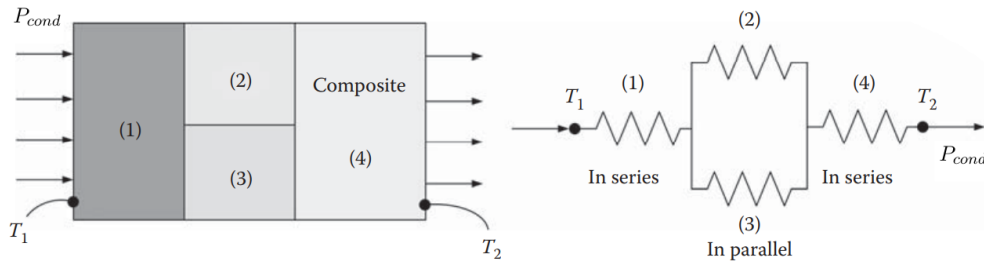
Figure 4.1. Thermal circuit for a series-parallel composite body.

This thermal circuit approach will be useful to simplify the conduction heat transport through complex systems such as the whole PT cooling station.

4.1.2 Radiation

Thermal radiation is a form of energy emitted as electromagnetic waves by all matter above a temperature of absolute zero. This heat transfer occurs purely due to the temperature of a source and it does happen also in the void: for this reason, it will be one of the mechanisms that we have to study in the high vacuum condition of the cryostat.

We can define a blackbody as an ideal body whose surfaces absorb all incident radiation, irrespective of wavelength and direction. For a given temperature and wavelength λ, no surface can emit more radiant energy than a blackbody. Using statistical methods, the blackbody spectral emissive power $E_{\lambda,b}(\lambda, T)$ is given by Planck's law. Integrating it over the entire range of wavelengths, we obtain a fundamental equation of thermal radiation that is Stefan Boltzmann's law:

$$P_{rad} = A\sigma T_s^4 \qquad (4.8)$$

where $\sigma = 5.67 \times 10^{-8} \frac{W}{m^2 K^4}$ is the Boltzmann's constant, T_s is the temperature of the blackbody and A its emitting surface.

Generally, we can consider the properties of a generic surface with respect to that of a blackbody. Radiative properties of a surface describe how an actual surface emits (through emissivity ϵ), reflects (through reflectivity ρ), absorbs (through absorptivity α) and transmits (through transmissivity τ) radiant energy. For example, ϵ represents the ratio of the actual radiant energy emitted by a surface relative to the energy emitted by a blackbody at the same temperature; analogous definitions stand for the other three properties.

All of these depend, in general, on the direction angle θ and wavelength: a diffuse emitter is characterized by equal energy emission in all directions, hence the properties will be independent of angle θ.

Kirchoff's law states that the emissivity at a given wavelength must equal the absorptivity at the same wavelength,

$$\epsilon_\lambda = \alpha_\lambda. \qquad (4.9)$$

A gray surface is characterized by radiation properties independent of wavelength:

we can define a gray diffuse body that has all the mentioned properties independent of direction and wavelength.

If we consider the heat exchange between two different surfaces, we have to introduce another quantity. Usually, only a portion of the radiation emitted from a surface arrives at another surface; we can define the view factor F_{ij} as the fraction of radiation heat transfer rate leaving surface i that is intercepted by surface j. The computation of these view factors is quite difficult and values for particular geometries are tabulated. A simplified case is that of enclosures. If we consider the radiation exchanged between all the surfaces inside an enclosure, we find the simple relation:

$$\sum_{j=1}^{n} F_{ij} = 1 \tag{4.10}$$

which stands for each i-surface. Particular types of enclosures are long parallel plates or long concentric cylinders.

In these particular enclosures, we can find a general expression for P_{rad}; it depends upon the specific view factor F_{12} between surfaces 1 and 2 and is characterized by their temperature T and emissivity ϵ,

$$P_{rad} = \frac{\epsilon_1 A_1 \sigma (T_1^4 - T_2^4)}{(1 - \epsilon_1) + \left(\frac{\epsilon_1}{F_{12}}\right) + \left(\frac{A_1 \epsilon_1}{A_2 \epsilon_2}\right)(1 - \epsilon_2)}. \tag{4.11}$$

We can see from Equation 4.11 that the radiative heat transfer rate is proportional to $(T_1^4 - T_2^4)$ of the surfaces in the enclosure. In the case of the ET-LF cryostat, the surfaces can refer to the inner surface of the cryostat itself or the different surfaces of the radiation shields. In the cooling process, we can then understand that if the temperature of the body's surface that we are cooling is high (in its absolute value and also with the respect to the other surfaces), the radiation mechanism will be the main contributor to the heat exchange. If the temperature is low, approximately below $150K$ [27], conduction heat transfer starts to become the primary form of heat transport: for this reason, geometries and materials are a key point in the design of cryogenic interferometers.

4.2   Cooling time

One of the most important parameters in a cryogenic system is the cooling time. If simulations and computations for the temperature gradient can be easily done in a steady-state scenario, in the real application, those results, has to be obtained in a finite time. In a facility such as ET-LF, the cooling time of the whole cryogenic apparatus has to be as small as possible to have more time for observations during a particular observational run.

Furthermore, another problem that has to be considered is the adsorption of the residual molecules by the mirrors. KAGRA has this sort of problem [27]. Water molecules could reach mirrors from the room temperature arms: the adsorption of them by the mirrors will decrease the reflectivity, the finesse of the cavity and then the sensitivity of the whole interferometer. Several calculations can be done to estimate the adsorption considering a Maxwell-Boltzmann distribution for the

molecules. Water molecules, whose size is of the order of 1Å, will form a layer on the mirror in a time that is:

$$t_{water} \sim 300 days. \tag{4.12}$$

The contribution of this layer of water molecules will be of the order of the molecules' size multiplied by a factor that considers the statistic of the adsorption. This value is comparable with the roughness of KAGRA's mirrors without the layer. Hence, to recover the mirror from adsorption, it is necessary to heat up the mirror to room temperature and to cool it down again once per 300 days. The cooling time, then, has to be much smaller than this number to have sufficient operative time for observations.

The main mechanisms of heat transport, which have to be considered in the cryogenic interferometer for cooling, have already been introduced in previous Sections (4.1.1 and 4.1.2). In those cases, general expressions for the heat flow rate have been presented (4.1 and 4.11). To compute the time we need to cool down a particular body, we need also information about the heat that has to be extracted.

Let's consider a one-dimensional problem and let $Q = Q(x,t)$ be the internal heat energy of a body at each point and time. In the absence of heat generation, from internal or external sources, the rate of change in internal heat energy of a body will be proportional to the rate of change in its temperature:

$$\frac{\partial Q}{\partial t} = \rho V c_P(T) \frac{\partial T}{\partial t} \tag{4.13}$$

where ρ is the body's material density, V its volume and $c_P(T)$ is the specific heat (at constant pressure) that in general depends on the temperature. The specific heat, by definition, is the amount of heat that must be added (or subtracted) to one unit of mass of the substance in order to cause a variation of one Kelvin:

$$c_P(T) = \frac{\Delta Q}{\rho V \Delta T}. \tag{4.14}$$

If we use the thermal circuit approach, we can have an approximative estimate of the temperature rate variation of each i-th body in series-parallel, starting from Equation 4.13:

$$\frac{\partial T_i}{\partial t} = -\frac{\sum_j P_{ij}(T)}{\rho_i V_i c_{P_i}(T_i)} \tag{4.15}$$

where $P_{ij}(T)$ is the heat flow rate (by conduction or radiation) from the body i to any body j.

From Equation 4.14, we can further obtain an estimation of heat that has to be extracted from the body to cool it down of ΔT. Dividing it by the total heat flow rate, we can obtain an approximative value for the time needed for the cooling:

$$\Delta Q_i = \rho V_i c_{P_i} \Delta T_i \quad \rightarrow \quad t_i = \frac{\Delta Q_i}{\sum_j P_{ij}}. \tag{4.16}$$

The exact computation of the transient heat transfer, when only conduction takes place (or when its contribution is the dominant one), leads to the typical Partial Differential Equation (PDE) for the temperature. A PDE is an equation

that imposes relations between the various partial derivatives of a multi-variable function, e.g. $T = T(x, t)$. This expression, in the one-dimensional case, can be obtained by combining Equations 4.13 and 4.1:

$$\frac{\partial T}{\partial t} = \frac{\kappa(T)}{\rho c_P(T)} \frac{\partial^2 T}{\partial x^2}. \tag{4.17}$$

Equation 4.17 can be easily made more difficult by introducing the radiation, for instance as a boundary condition on the radiating surfaces.

The exact solution of this equation is difficult to obtain, especially in the case of complex geometries and temperature-dependent coefficients such as specific heat or conductivity. Numerical approaches are then required to have a complete understanding of the whole heat transfer and to perform useful simulations.

4.3 Finite element analysis

Finite Element Analysis (FEA) is a powerful numerical analysis that relies upon the Finite Element Method (FEM)[29]. The FEM is a numerical method that is used in many branches of science and engineering including heat transfer; it is used to set up and solve systems of PDEs. FEM is exploited to divide a system, whose behavior cannot be predicted, into small pieces, or elements, whose solution of closed-form equations is known or can be approximated. The real benefit of FEA lies in the ability to solve arbitrary complex problems for which analytical solutions are not available or which would be prohibitively time-consuming. The overall steps in the FEM can be summarized as follows.

1. The first step is the discretization of the whole geometry: the model can be defined by a number of points in space called nodes. Each node has a set of degrees of freedom (temperature, displacements, etc.) that can vary based on the inputs of the problem. These nodes are connected by elements that define the mathematical interactions of the degrees of freedom. The shape of elements and their spatial distribution have, then, to be defined. For two-dimensional problems, common types of elements are linear triangles, bilinear rectangles and bilinear quadrilaterals; for multi-dimensional problems, other, more complex, shapes are used.

2. The next step is to choose a type of interpolation for dependent variables within the element. This choice, sometimes, is forced by the element type but for multi-dimensional cases, it is free to choose. In the two-dimensional case, the examples mentioned give us informations about the interpolation that is linear, bilinear, quadratic, etc.

3. We have then to determine the element property equations (or stiffness equations) which are used to solve the input problem. In our case, we have to set the Equations presented in previous Sections to describe the heat flow.

4. Once equations for every element are imposed, we have to assemble all the elements within the mesh, i.e. the nodes grid generated in the first step, following a specified group of assembly rules.

5. In the fifth step, boundary conditions are applied. In heat transfer problems, typical boundary conditions could be a fixed temperature in a specific point or heat flow rate entering or exiting a surface, e.g. heat flow rate settled by radiation or refrigeration power.

6. In the last step, the discrete equation set is solved with particular methods to obtain the global result for the whole geometry.

Just as a regular polygon approaches a perfect circle as the number of sides approaches infinity, a finite element model approaches a perfect representation of the real system as the number of elements becomes infinite. Since it is impossible to divide the system into an infinite number of elements, the FEM produces the exact solution to an approximation of the real problem we want to solve. The approximation can be improved, for instance, by refining the mesh created for the geometry, i.e. decreasing the size of elements to have a better interpolation. However, this may increase the number of equations to be solved extending the solution time beyond the point where it is practical to solve them by hand. For this reason, the FEM is always associated with computer programs that set up, solve and post-process the solutions to visualize them simply.

The software, based on FEM, used to perform thermal simulations, is ANSYS Mechanical. Mechanical is one of the different packages that ANSYS provides and it allows us to perform not only thermal simulations but also modal or structural simulations and combinations of them. From the thermal point of view, ANSYS gives us the possibility to perform a steady-state analysis and also a transient analysis. The former will be useful to understand the asymptotic limits of the geometry of the whole PT cooling station whilst the latter will be useful to understand the feasibility of the cooling, keeping in mind all the considerations made in Section 4.2.

To perform these types of simulations, ANSYS Mechanical uses the discrete form of Equations 4.1 and 4.11 when both radiation and conduction are considered. The software gives us the possibility to choose the material that forms all the different parts of the design with customized properties (such as conductivity $\kappa(T)$ and specific heat $c_P(T)$). For the radiative properties, only the emissivity ϵ has to be chosen because Mechanical considers all the bodies as gray diffuse (see Section 4.1.2) with emissivity equal to absorptivity (Kirchoff's law) and

$$\epsilon + \rho = 1. \tag{4.18}$$

Since transmissivity τ is considered null, through the only information of the emissivity, the software can obtain also the value of reflectivity through which it can compute the net energy absorbed by a surface with radiation. All the view factors are calculated within the different enclosures that can be defined manually.

4.4   Model

After the first, general, introduction to the principal heat equations, we can start describing the whole design of the PT cooling station. As already mentioned, the cooling station is composed of two PTs connected via a heat path to the cryogenic payload. The cryogenic payload is still under study, so, when the Amaldi Research Center will be completed, the PT cooling station can be tested on a test chamber. This test chamber will be a simple cubic chamber in which we can put different test masses to study the cooling time and also the vibration transmission. Simulations that will be presented in this dissertation will be performed considering this test chamber instead of the whole payload.
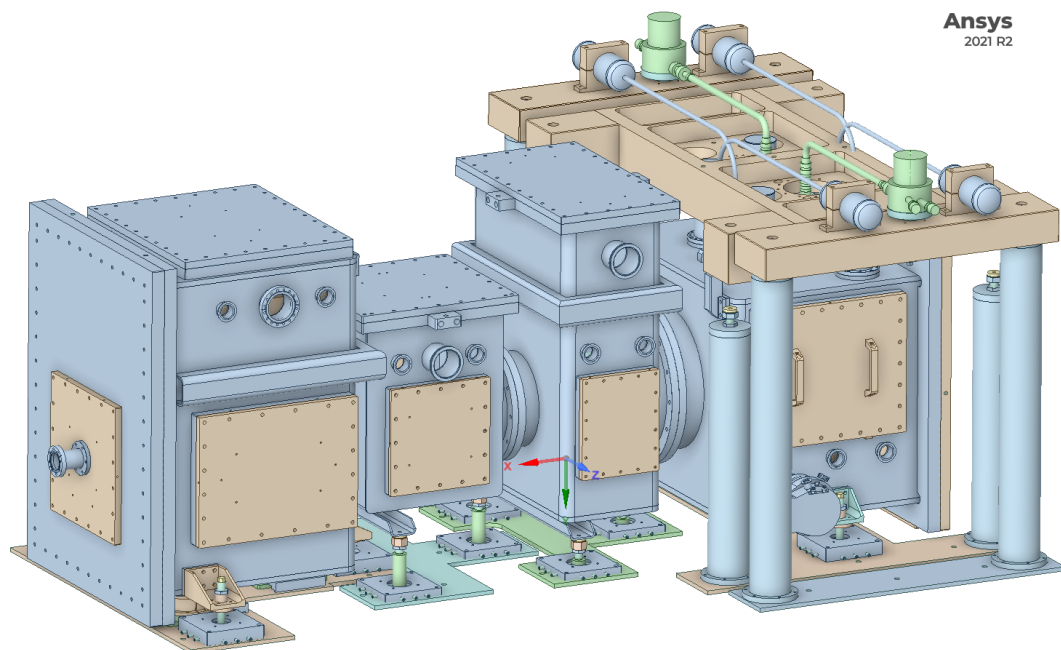

Figure 4.2. Complete model of the PT cooling station. External of the vacuum chamber.

The description of the design can start from the external outlook. Figure 4.2 represents the vacuum chamber that contains the cooling station. From the left to the right, we can see four different vacuum chambers assembled together through flanges that assure the vacuum condition is kept inside. The first one contains the test chamber while the rightmost is the one where the PTs are situated. The two chambers in the middle are useful for the support of the whole heat path and to cover the region where the heat path is vibrationally decoupled from the remaining part by means of the heat links.

Inside the vacuum chamber, which will be at room temperature, there is the shield connected to the first stage of PTs. It will be the $40K$ shield useful to reduce the incoming radiation from the room temperature vacuum chamber to the inner heat path. The heat flow rate would, indeed, be too high between two surfaces of $\sim 4K$ and $300K$ (up to a few hundreds of W), so an intermediate shield at $40K$ will

reduce drastically the radiation, which is proportional to the fourth power of the temperature (see Equation 4.11). The design of this shield, which covers both of the vibrationally decoupled parts of the heat path, is reported in Figure 4.3.
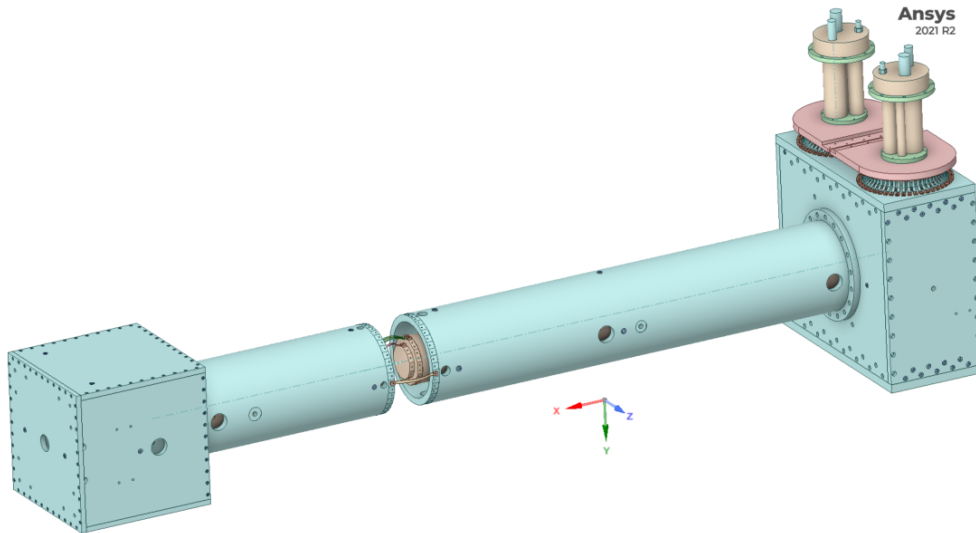

Figure 4.3. Complete model of the PT cooling station. Inner $40K$ shield.

On the left side of the Figure, we can better see the cubic form of the test chamber (also the shield will have the same shape). On the right side of the Figure, we can see the first stage of the PTs that will be connected to the shield by heat links. This will be the first contribution to the reduction of the vibrations coming from the PTs themselves. The shield that covers the inner bar used as the heat path will have a cylindrical shape.
The whole $40K$ shield will be made of Al 1080, i.e. 99.8% purity aluminum. In the Figure, all the suspensions and connections that are used to secure the shield to the vacuum chambers are omitted.
The inner heat path design is reported in Figure 4.4. We can see the test chamber on the left side part of the Figure whilst on the right side, the two PTs can be clearly seen. We can notice that also the second stages of the PTs are connected through heat links in the same way as the first stages. The connection with the heat path is made in a hammer shape region of the bar that has to be expanded to harbor both the PTs' first stages.
The bar will be made of Al 5N5 and will be vibrationally decoupled through two sets of heat links placed on the bar and on a smaller, inner, support.

We can now describe in detail all of the main parts of the design considering also the particular connections and suspensions that are useful to assemble the whole geometry. Particular attention will also be paid to the description of the innovative design of the heat links.
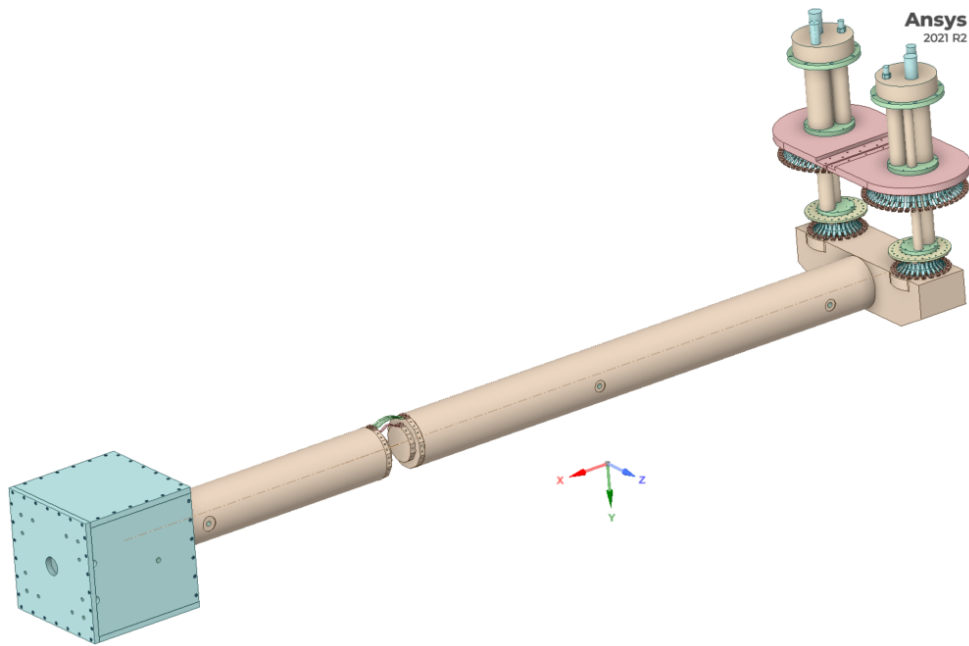
Figure 4.4. Complete model of the PT cooling station. Inner heat path.

4.4.1 Pulse tubes

The two PTs that would provide the refrigeration power are the PT420 Cryocoolers from Cryomech Inc..The design is reported in Figure 4.5.
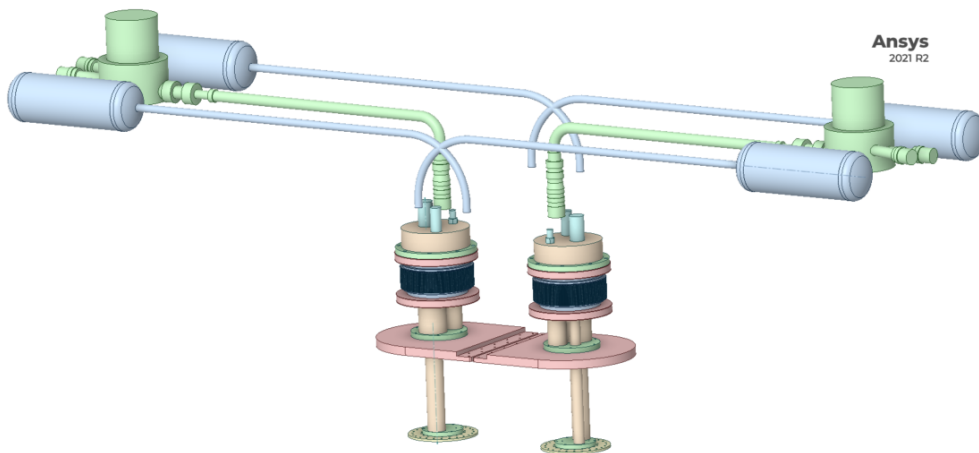

Figure 4.5. The two PT420 cryocoolers which would provide the refrigeration power to the whole PT cooling station.

The two pulse tubes have the rotary valve separated from the bulk of the PT: this configuration is called Remote Motor Option. This setup is preferred in a cryogenic interferometer because the mechanical vibrations arising from the rotary valve are strongly attenuated and only the high-pressure pulse vibrations reach the cold head.

The Figure shows the rotary valves with their connection tubes (not connected) on the upper side. The two PTs are connected together through a plate (pink in the Figure) from which heat links would connect the $40K$ shield. Above that, another vibration dissipation system is present in the vacuum chamber connection region. The characterization of a PT relies upon the refrigeration power that every stage can supply at different temperatures. Cryomech Inc. provides this information with the specific capacity curve of each PT model. The capacity curve for the PT420 with Remote Motor Option is represented in Figure 4.6.
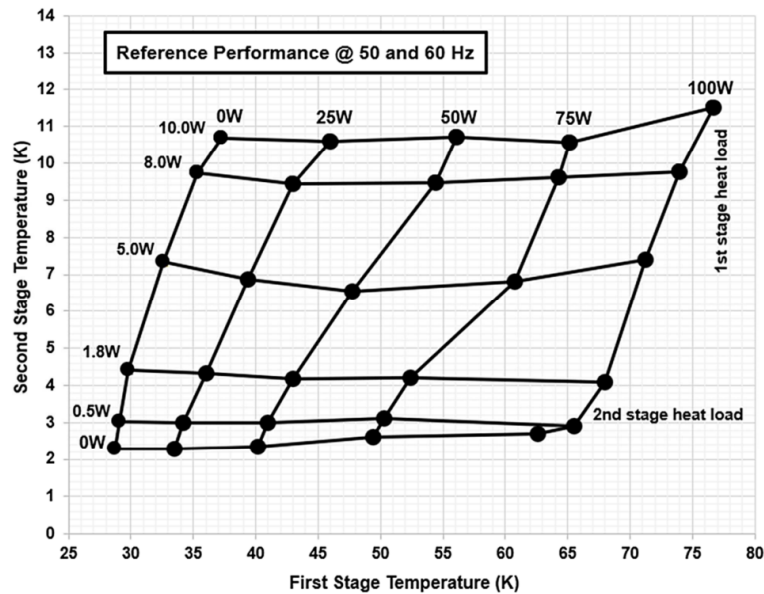

Figure 4.6. Capacity curve for PT420 cryocooler model with Remote Motor Option from Cryomech Inc. .

The Figure has on the y-axis the second stage temperature of the PT whilst on the x-axis the first stage one. All the horizontal lines refer to the refrigeration power provided to the second stage load; conversely, the vertical lines refer to the refrigeration power provided to the first stage load. The trend of the refrigeration lines isn't regular with the temperature and remark the fact that, in the low-temperature regime, it is more difficult to further cool down an object. This capacity curve will be crucial in the computation of the cooling time of the whole PT cooling station, especially in the low-temperature regime.
The pulse tubes and the vacuum chamber that contain them are supported by a solid structure, resting on the ground, which is presented in Figure 4.7.

4.4.2 Suspension fibers

The $40K$ shield is connected to the vacuum chamber by means of various suspensions, e.g. solid or fiber suspensions. We can see in detail the connections of the test chamber shield in Figure 4.8.

The Figure reports, on the left side, the interior of the vacuum chamber of the test chamber, we can see, indeed, the bottom plate that will complete the vacuum
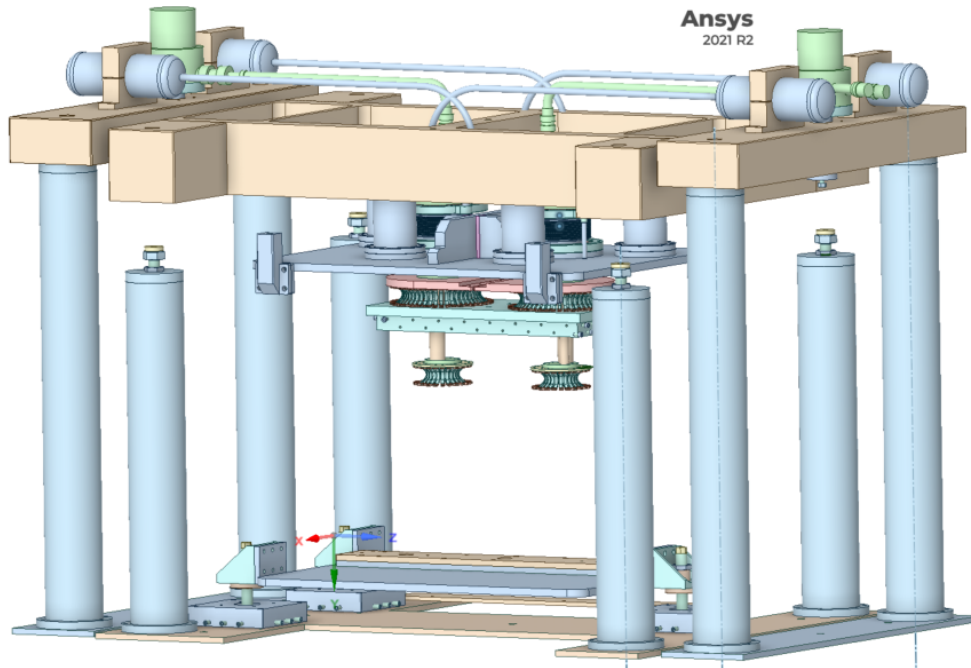
Figure 4.7. Structure used to firmly hold the PTs and the vacuum chamber of the cooling system.
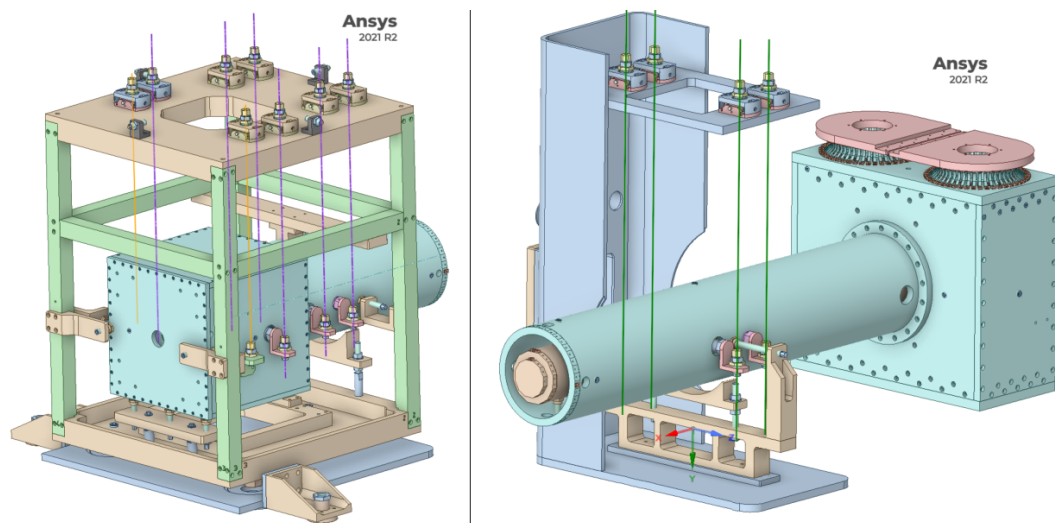
Figure 4.8. View side of the vacuum chambers. Left: test jig, a suspended platform surrounded by its thermal shield. Right: shield and cooling duct connected to the PTs' stages. The test jig chamber plays the role of a mini-cryostat to test cooling and vibration. The thermal connection between the two parts is the object of study in this thesis.

system. The test chamber's shield is surrounded by a cage that resembles the actuation cage of the payload design presented in Section 3.3.

The top of the cage is the plane from which eight different fibers are hung to suspend the chamber shield and the test chamber itself. Two fibers are used to hold the shield (yellow in the Figure) whilst six fibers (purple in the Figure) are used to suspend the chamber through six different supports that, through holes in the shield, are directly connected to the test chamber.

A similar suspension system is also used on the other side of the vibrational decoupled heat path. Inside the third (from the left) vacuum chamber in Figure 4.2 there is a similar fibers suspension system for the inner bar. In this case, the outer shield is connected to the vacuum chamber through mechanical support connected to the lower plate that closes the vacuum system. The fibers are four (green in the Figure) and are connected to the bar with the same supports already mentioned for the test chamber.

4.4.3   Heat links

As already discussed in the previous Sections, heat links are one of the crucial parts of the whole ET-LF interferometer. They have to vibrationally decouple the different parts of the heat path and the heat path itself from the payload, while efficiently thermally connecting all of them. To do this, flexible heat links have to be designed with a particular choice of materials that will be suitable for the thermal connection. KAGRA uses Al 6N for its heat links whose design is discussed in Section 2.5.3.

The design for ET heat links is quite different: it will have similar terminal heads to those of KAGRA (see the bottom side of Figure 2.10) while the seven twisted wires will be replaced by three foils with a thickness that varies between $50\mu m$ and $100\mu m$. The design is represented in Figure 4.9.
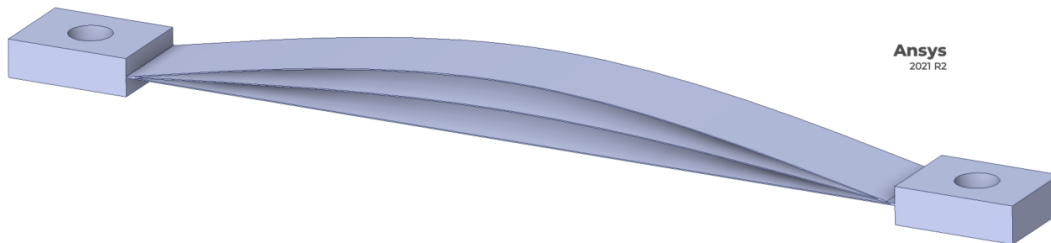

Figure 4.9. Heat link design with three foils in parallel between the terminal heads.

The materials also change with respect to KAGRA's. The terminal heads will be made of Cu 5N while the foils in Al 6N. The choice of copper for the heads is determined by a conservative approach. The aluminum is too soft for the realization of the terminal heads; hence, the use of copper guarantees a more reliable result maintaining almost the same thermal characteristics. A first heat link prototype is presented in Figure 4.10.

The heat links used in the PT cooling station with the test chamber will be of different lengths depending upon their positions. For the thermal simulations, the thermal circuit approach is used. The three foils are in parallel with length and cross-sectional area similar between them (at least in the real prototype). The simulation will then consider a single foil with an equivalent resistance for the three
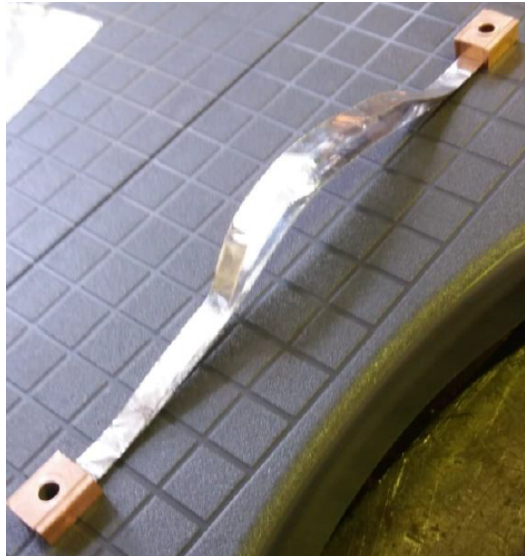
Figure 4.10. Heat link prototype with three Al foils and two Cu terminal heads.

parallel foils; following Equations 4.5 and 4.6 it becomes a foil with a tripled thermal conductivity. In this way, the simulation time will be reduced but the heat flowing will remain the same.

The terminal heads of all the types of heat links in the various positions are the same: a sketch is reported in Figure 4.11 with all the measurements.
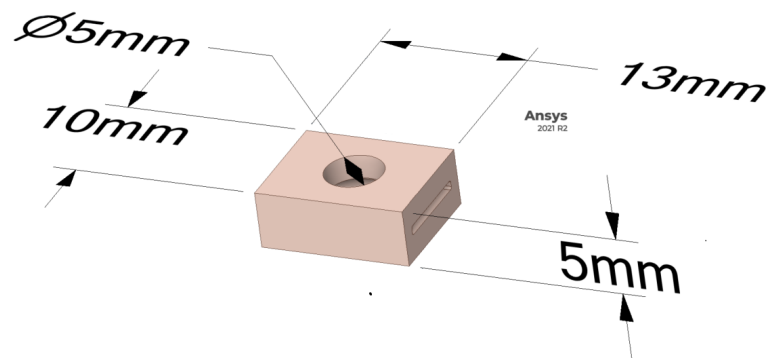

Figure 4.11. Terminal head in Cu 5N analogous in all the different heat links.

For the description of the differences between all the heat links, we can start from those connecting the two parts of the bar (and shield) represented in Figure 4.12.

The maximum number of heat links that the heat path and shield can sustain are:

- shield: 40,
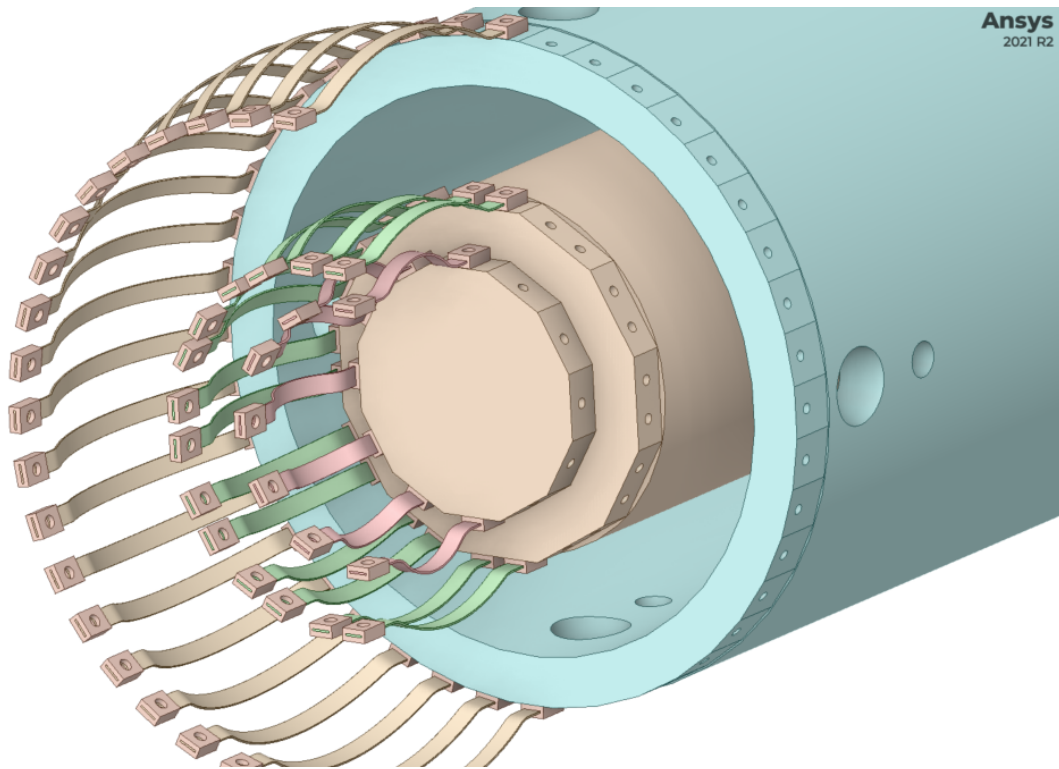
- external surface of the bar: 24,

Figure 4.12. Heat links connecting the two vibrationally decoupled parts of the bar and shield.

- inner support on the bar: 12.

The particular design of the heat links' foil changes with respect to their position. The distances between the two head's holes in each heat link are reported in Figure 4.13. From the top to the bottom, heat links of the shield, external surface of the bar and inner support are reported.

The remaining design of the heat links is that of the PTs' heat links. The detail of the connection is represented in Figure 4.14.

In this case, the heat links are attached forming two concentric circles to maintain the heat connection as smooth as possible between the shield (or the hammer shape region of the bar) and the bases on which PTs rest. Because of the two concentric locations for the connection, the number of heat links in each stage of each PT is high:

- first stage of each PT: 72,

- second stage of each PT: 42.

This so large number of heat links makes the connection mechanically tight with a non-efficient vibration decoupling; the thermal connection, therefore, will be excellent. An acceptable trade-off between the two will be one of the aims of the simulations. The design for the simulations and the measurements of this type of heat link is presented in Figure 4.15
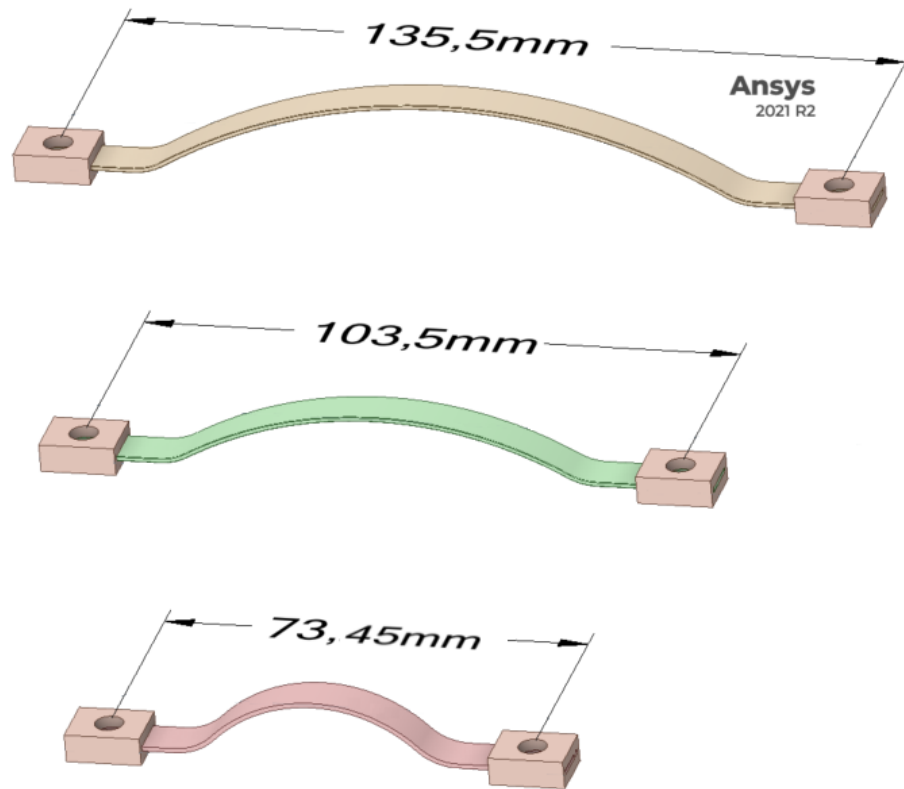
Figure 4.13. Particular design of the shield, external surface of the bar and inner support heat links from the top to the bottom. Relative measurements are reported.

4.5 Materials

The choice of the materials for all the different parts of the ET-LF interferometer, especially for the PT cooling station, has fundamental importance to achieve an efficient thermal transfer throughout the whole system. When the temperature starts to drop below $\sim 150K$, conduction heat transfer starts to overwhelm the radiation contribution: Fourier's law becomes then the driving equation for heat transport. The conductivity κ has a major role in these situations. Aluminum and copper are well known for their high thermal conductivities at cryogenic temperatures: this is the reason why these materials are the ones chosen for the cryogenic elements in the PT cooling station[35].

The inner bar, indeed, is made of Al 5N5 while heat links have Cu 5N as material for the terminal heads and Al 6N for the foils. Heat links have to efficiently thermal connect the different parts while they have to be soft to reduce the vibrations. The stiffness of the heat links is characterized as the spring constant in the practical application, the Young's modulus is then a key parameter in the choice of the material. Aluminum has almost half the value of Young's modulus for copper ($70\,GPa$ vs $130\,GPa$), therefore, aluminum has a large advantage over copper to realize soft heat links. For this reason, KAGRA's heat links are completely made of Al 6N. ET-LF's heat links, instead, will have only the foils made of 6N whilst
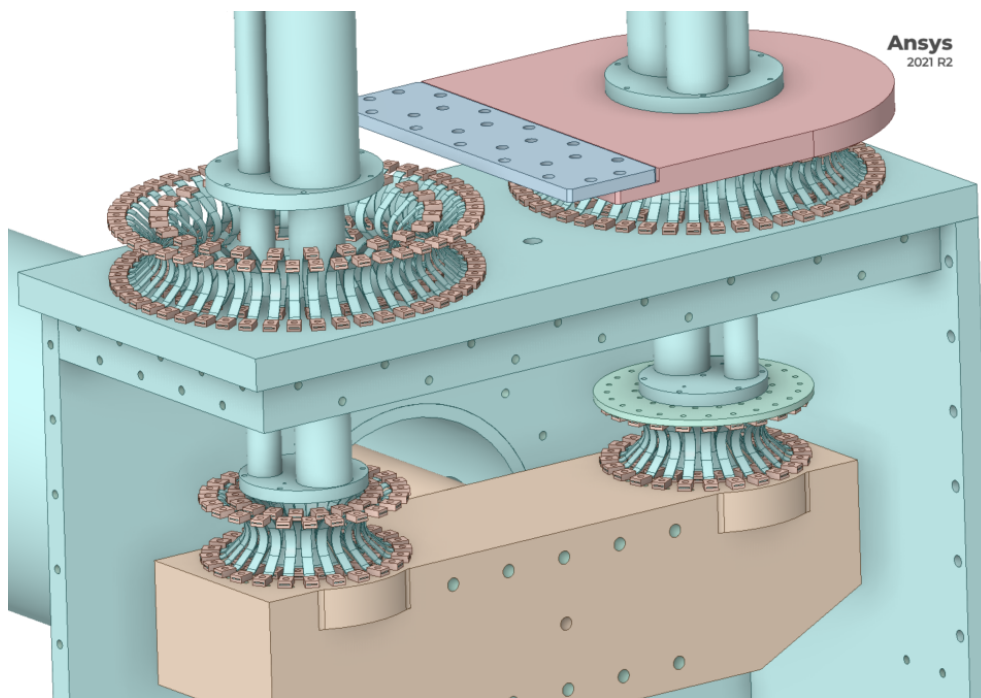
Figure 4.14. First and second stages of the two PTs and their heat links.
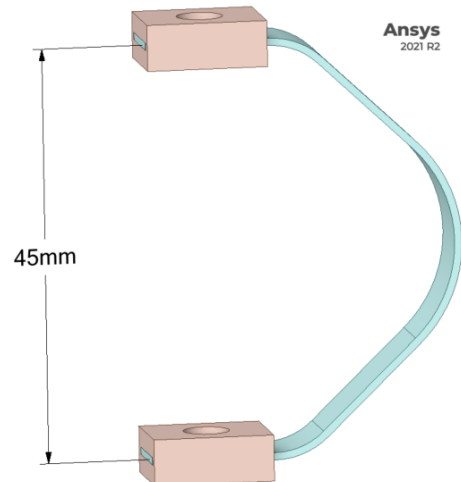
Figure 4.15. Design of first and second PTs' stages heat link.

the terminal head will be made of Cu. Therefore, the foils have to be as soft as possible while the terminal heads are used only as joints with the different parts of the interferometer. The choice of copper is, therefore, still optimal especially if it is made to avoid the possible deformations or problems in the clamping mechanism (see Section 4.4.3).

The thermal properties such as thermal conductivity $\kappa(T)$ or specific heat (at constant pressure) $c_P(T)$ of these materials can be found in literature, though the

real values depend on the specific element because of its geometry, purity, history of cold work and annealing. For this reason, thermal conductivity measurements of Al 6N used for the prototype of heat links will be presented in Chapter 6 of this dissertation. Thermal simulations, which will be the main topic of the next Chapter, will use instead tabulated values for thermal conductivity which, therefore, vary more than one order of magnitude between them at the same temperature. This will set a minimum and a maximum value for the conductivity that will fix a range for the accessible temperatures in the simulations. A. L. Woodcraft collected different values for the conductivity of high purity aluminum and copper from the literature providing recommended values depending upon temperature[33]. The results can be seen in Figure 4.16.
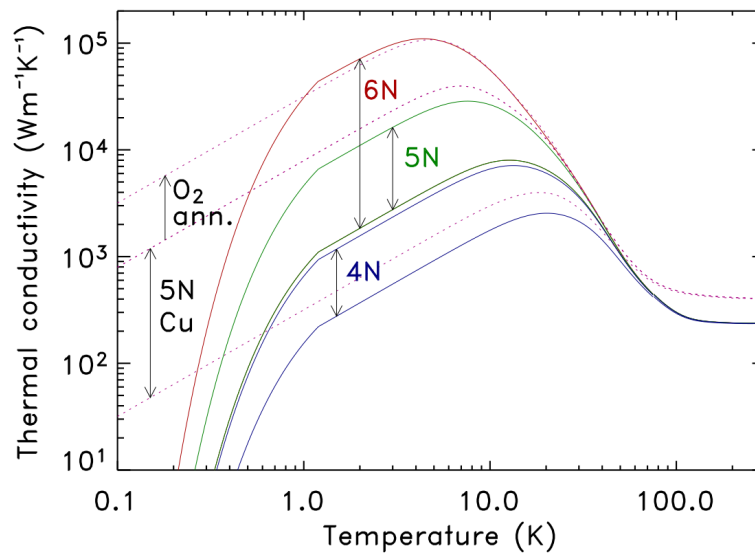
Figure 4.16. Recommended values for thermal conductivity for high purity aluminum and copper.

The thermal conductivity of these materials, as we can see in the Figure, increases by almost three orders of magnitude from $100K$ to cryogenic temperatures, i.e. below $10K$. This makes them suitable for the efficient conduction heat transfer that we need at those temperatures. The maximum and minimum values for high purities Al are reported with solid lines while those for Cu are in dashed lines. The limits of the ranges that simulations will consider are reported with the arrows of 6N and 5N Cu. Maximum values for the Al 5N5 are similarly chosen by interpolating between the two solid lines for 5N and 6N Al.

Since the variation of thermal conductivity with the temperature occurs below $100K$, we have to find its value also for the Al 1080 that composes the shield. This, indeed, will have a temperature that ranges between $40K$ and $100K$, so its thermal conductivity will change.

Values considered in the simulations are reported in Figure 4.17, in which the lower limit for generic 1000-series Al is represented among other Al alloys[32]. Those values will represent a conservative approach in the thermal transfer that will lead
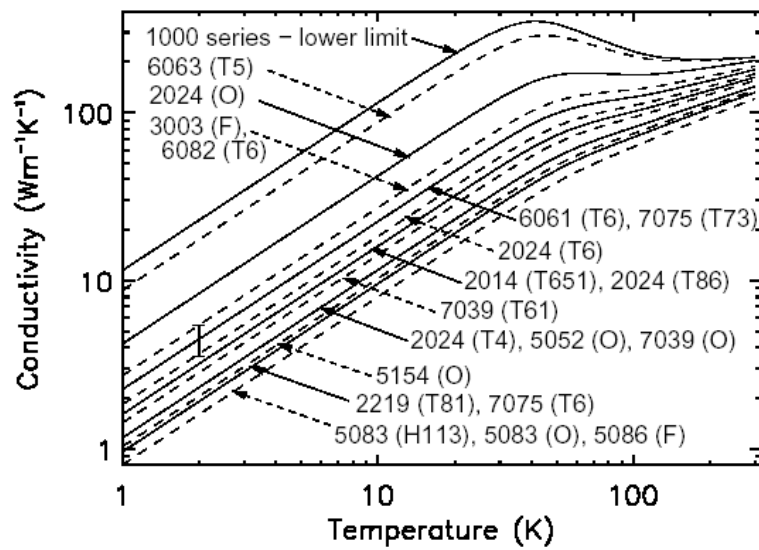
Figure 4.17. Recommended values for thermal conductivity for different Al alloys including 1000-series.

us to obtain a lower limit for the heat transfer in the shield.

For the computation of the cooling time, the specific heat of the different components of the PT cooling station will have a crucial role. It, indeed, gives us informations about the amount of heat that we have to subtract from an element in order to reduce of a certain ΔT its temperature. Values considered for aluminum (blue) and copper (orange) are represented in Figure 4.18[4].
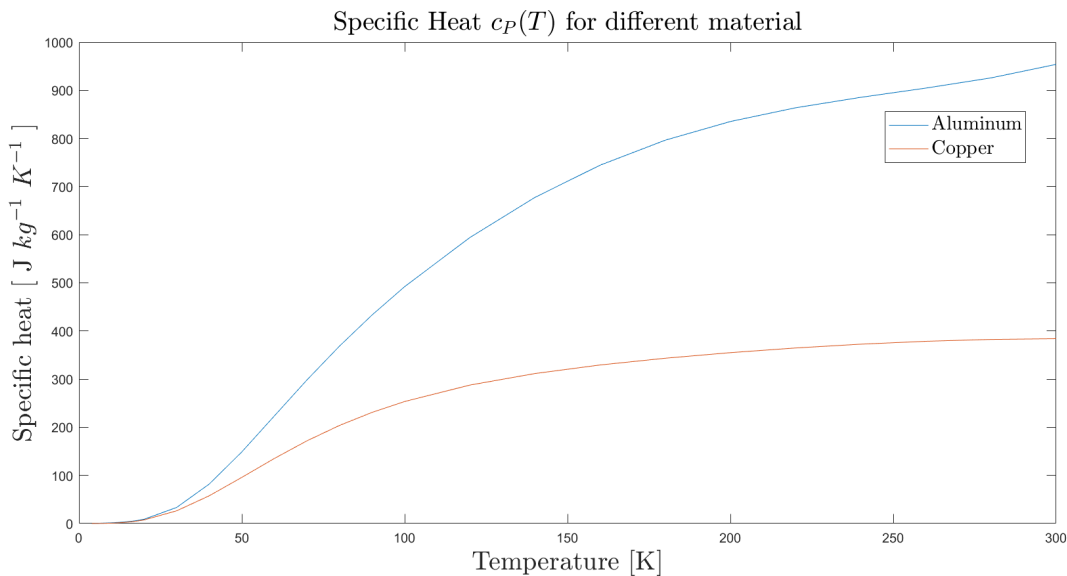
Figure 4.18. Specific heat values for aluminum (blue) and copper (orange).

4.6   Simplified model

Since FEM time spent on the analysis will grow depending on the number of elements, the model presented in Section 4.4 has to be simplified as much as possible maintaining the overall structure and crucial heat connections. All the inner suspensions between the shield and vacuum chamber or the inner bar and shield can be excluded from the simulations because the heat transfer through them can be considered negligible. The external outlook becomes the one represented in Figure 4.19.
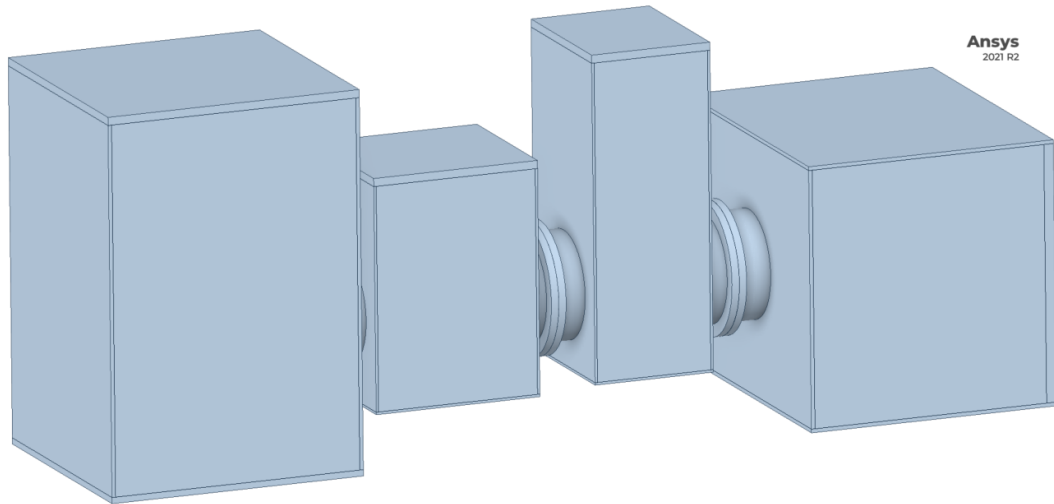
Figure 4.19. Simplified model of the PT cooling station. External of the vacuum chamber.

All the vacuum chambers become simple parallelepipeds maintaining the real size. The interior design is reported in Figure 4.20.
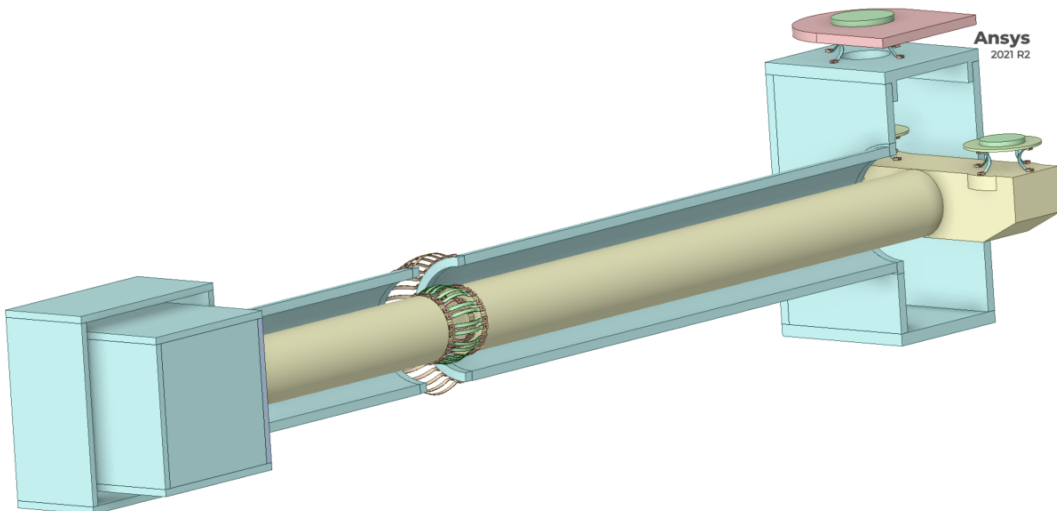
Figure 4.20. Simplified model of the PT cooling station. Shield and inner bar.

The entire PTs are removed and only the bases on which they rest remain: the refrigeration power will be imposed as a condition on those surfaces. The heat links, connecting the two parts of the bar, are in the same configuration already described in Section 4.4.3 whilst heat links connecting the PTs are reduced to only four. To maintain the same heat transfer of the real model, the conductivity of these heat links is modified through thermal circuit approximation; the symmetry of the connection is equally maintained by positioning the heat links each at 90 degrees from the others.

Chapter 5

Thermal simulations

Different types of thermal simulations can be performed using ANSYS Mechanical. We can divide them into the steady-state and transient ones.

The former refers to a simulation that evaluates the asymptotic equilibrium solution for the model. The system in this case is subject to constant heat loads and environmental conditions. Since in our thermal simulation we need to consider the variation in temperature of the conductivity $\kappa(T)$ and the contribution of radiation, the software must iterate to find a steady-state solution to the governing equations presented in Section 4.1.

The latter is, instead, a simulation that takes into account the temperature and other thermal quantities that vary over time. It will consider the history of the temperature variation of a body: this can be used to compute the cooling time of the whole PT cooling station on the bases of the capacity curve that will characterize the PTs' refrigeration power. In the same way as steady-state simulations, transient ones must iterate every time step to find the solution in the case of temperature-dependent properties; it will, therefore, continue the simulation for a fixed total time imposed at the beginning. The total simulation time will then be dependent also on the real-time through which the simulation must be performed: in this case a massive mesh refining may be prohibitive.

5.1 Thermal conditions

Before the start of a simulation, we have to define the conditions and constraints for all the governing equations. As already mentioned, ANSYS gives us the possibility to choose a tabulated material or to define a new material with particular properties such as conductivity and specific heat which vary over temperature. All the different parts of the PT cooling station are then specified with their material (following the considerations made in Section 4.4) and with the characteristic curves for conductivity and specific heat reported in Section 4.5.

From the radiative point of view, each radiative condition has to be imposed on a radiative surface. We can also specify a particular enclosure that will help the software in the computation of view factors. In the model, four different enclosures can be found:

- Exterior radiative surfaces: all the external surfaces of the vacuum chambers and flanges of the simplified model are exposed at ambient temperature. A radiative condition is considered in those surfaces with an open enclosure to ambient at a temperature of $300K$. The emissivity chosen for all these surfaces may vary but, in this case, it is fixed to $\epsilon = 0.25$. The emissivity of the radiative surfaces will vary for different simulations and will be crucial in the computation of the radiative heat transfer rate on each surface. Figure 5.1 shows in blue all those surfaces.
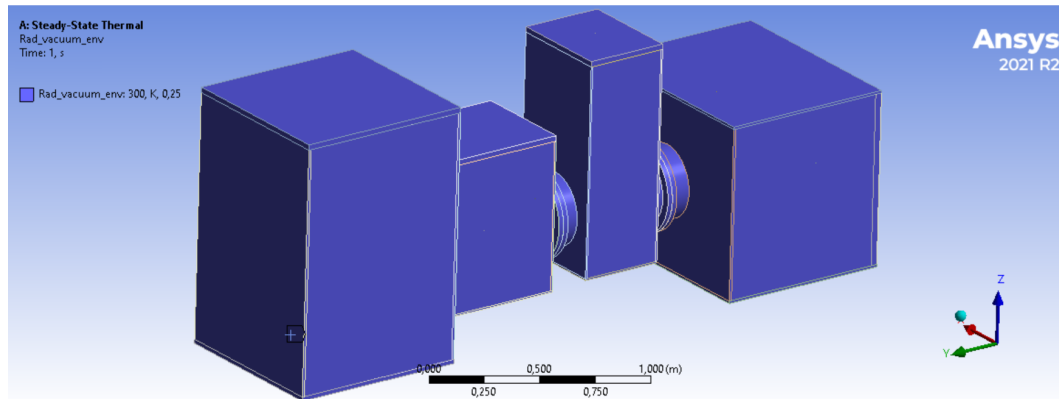
Figure 5.1. External radiative surfaces. The ambient temperature is fixed at $300K$ while the emissivity of the surfaces is $\epsilon = 0.25$.

- Interior of vacuum chambers - $40K$ shield: the first real enclosure that we can individuate is the one connecting the interior surfaces of the vacuum chambers (and flanges) with the external surfaces of the $40K$ shield. Since the shield is divided into two different parts to reduce the vibrations coming from the PTs, the enclosure can't be considered perfect. For this reason, ANSYS Mechanical has the possibility to choose an open enclosure: in this case, the sum of the view factors inside this enclosure for each surface will be less than one because some radiation can be lost through the aperture. In such an enclosure, an ambient temperature must be imposed; in a perfect enclosure, instead, the ambient temperature will be derived from the radiative equilibrium between all the surfaces. Since this enclosure is the one for the interior of the vacuum chamber, an ambient temperature of $300K$ will be considered. Figure 5.2 shows in blue the surfaces in the enclosure (represented by number 1 in the Figure): the emissivity of all the surfaces is fixed at $\epsilon = 0.25$ and also the room temperature is reported.

- $40K$ shield - inner bar: another enclosure is the one linking the interior surfaces of the $40K$ shield and the external surfaces of the inner bar. This enclosure, similarly to the previous one, will extend also in the region of the experimental chamber and, in the other direction, on the PTs bases and heat links located in the hammer shape region of the bar. The enclosure will be considered open also in this case because of the aperture on the shield (where the heat links are situated) and on the upper side of the PTs chamber (where two holes allow the

Figure 5.2. Radiative surfaces for enclosure number 1. The emissivity for all the surfaces is fixed at $\epsilon = 0.25$ and the ambient temperature at $300K$.

PTs to reach the inner bar). Since this enclosure won't directly see the $300K$ surfaces, an ambient temperature of $40K$ is fixed i.e. the expected temperature of the shield. Similarly to the other enclosure, this one (number 2) will have different emissivity for the surfaces depending on the simulation performed. Figure 5.3 shows in blue the radiative surfaces linked by this enclosure, this particular Figure has an emissivity for all the surfaces of $\epsilon = 0.25$ while the ambient temperature is fixed at $40K$.

Figure 5.3. Radiative surfaces for enclosure number 2. The emissivity for all the surfaces is fixed at $\epsilon = 0.25$ and the ambient temperature at $40K$. The Figure shows a section of the bar and shield.

- Internal surfaces of the experimental chamber: in the simulations, the experimental chamber is empty so a radiative condition is imposed on its internal

surfaces creating enclosure number 3. This enclosure extends until the whole right side part of the bar in Figure 5.4 which is hollow. Figure 5.4 shows a detail of this enclosure with the radiative surfaces in blue. Due to a hole located in the region connecting the two parts of the bar, this enclosure must be considered open: the ambient temperature, in this case, is fixed at $4K$.
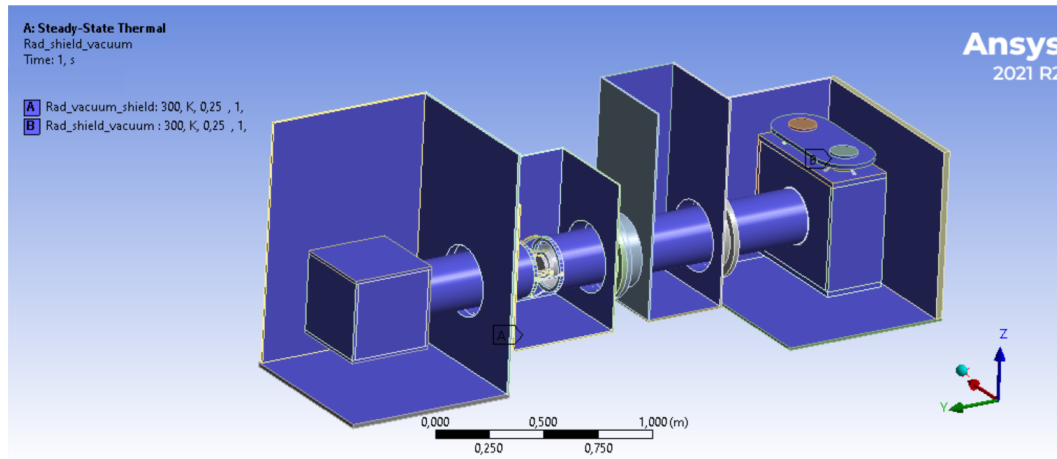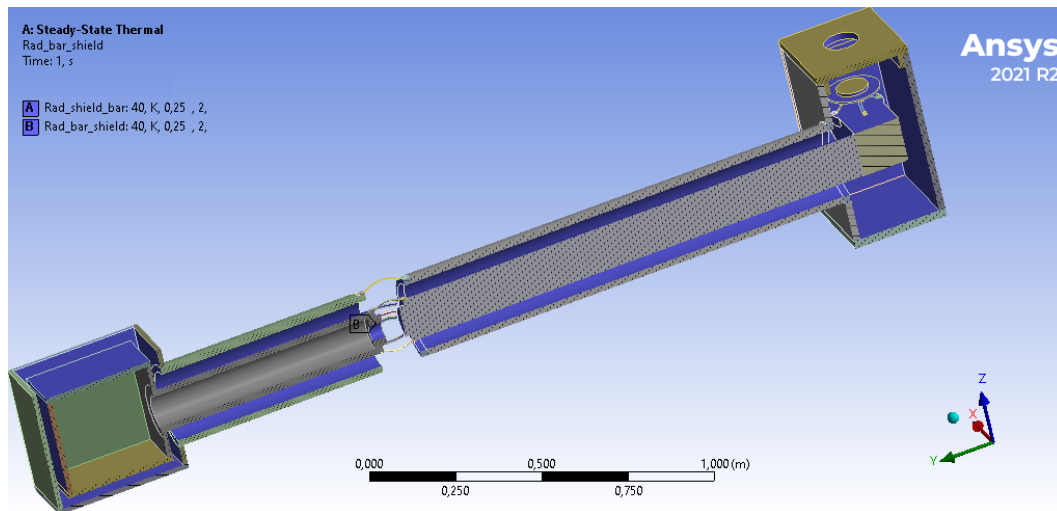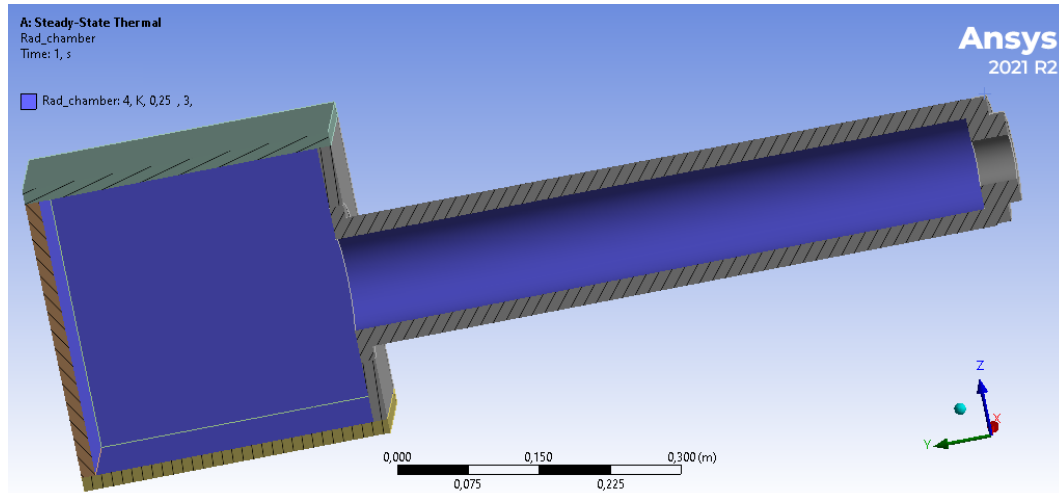

Figure 5.4. Radiative surfaces for enclosure number 3. The emissivity for all the surfaces is fixed at $\epsilon = 0.25$ and the ambient temperature at $4K$. The Figure shows a section of the bar and shield.

The other important condition we need to impose in the simulations is the heat load given by the refrigeration power of the pulse tubes. The surfaces where the refrigeration power condition is considered are the bases of the PTs reported in blue in Figure 5.5.

The refrigeration power provided by the pulse tubes is converted into a negative heat flow condition on those bases: two arrows in the Figure show the direction of the flow. The Figure represents a transient simulation where the heat flow condition can be modified, during the simulation time, to follow its dependence on the temperature of the surfaces where it is settled. Since the transient simulations will be useful to compute the cooling time, the temperature on those bases is expected to go down and the refrigeration power must follow it.

This condition is quite difficult to impose in the steady-state simulation because the PTs' refrigeration power is a function depending on the temperature of the first and second stages (see the capacity curve in Figure 4.6). Since a steady-state simulation must consider a constant heat load, the refrigeration power cannot be imposed with its variation with temperature. Even though we choose the heat flow value for a hypothetical equilibrium temperature, the simulation will be performed without taking into account the fact that at a higher temperature the refrigeration power (on the first and second stage) will be higher than at a lower temperature. Since this heat flow variation can't be considered, this condition can be modified into a temperature condition on the PTs bases. At the equilibrium, the surfaces' temperature where the PTs rest will be settled by the governing equations: the
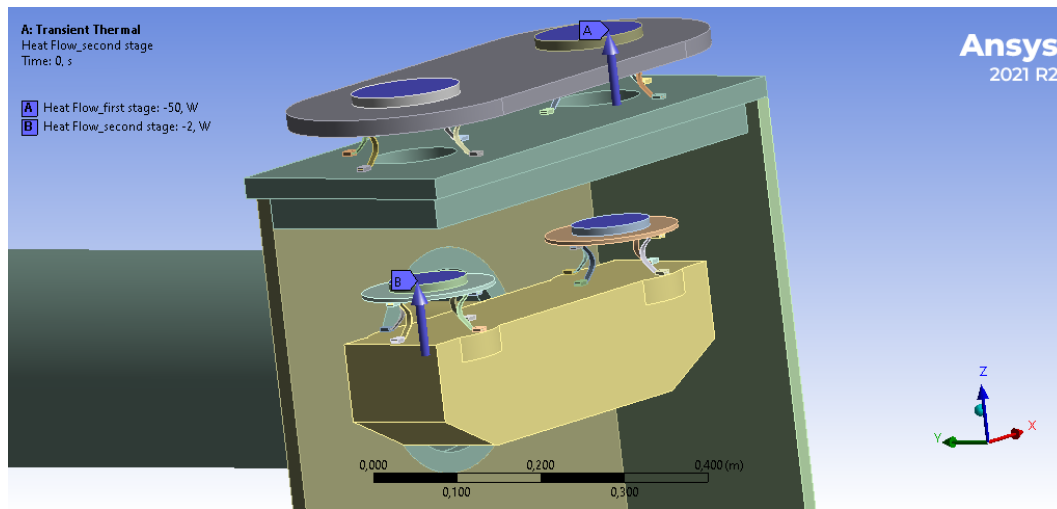
Figure 5.5. Surfaces where the refrigeration heat flow is imposed. The arrow indicates the direction of the heat flow.

heat transfer rate on those bases, that the simulation can compute, must equal the refrigeration power provided by the PTs. An iterative cycle can then be settled up to obtain the right temperature value (on the bases) that allows the conductive heat transfer rate to equal the refrigeration power given by the capacity curve at that temperature. In the following Section, where the steady-state simulations will be described in detail, the fundamental points of this cycle will be explained.

The last condition that we have to specify is the choice of emissivity for the different surfaces. The common manufacturing technique for aluminum objects leads their emissivity to the value of $0.15 - 0.20$. An emissivity of $\epsilon = 0.15$ will be considered for a real expectation value while a value of $\epsilon = 0.25$ will be considered in the worst scenario.

5.2 Steady-state simulations

Let's describe, firstly, the steady-state simulations that will be useful to understand the physical limit of the temperature gradient over the whole PT cooling station. As already mentioned in the previous Chapters, the temperature we need for the cryogenic payload is below $\sim 20K$: this value can be reached if the heat extracted through the heat path in the cooling station is the highest possible. A steady-state simulation can let us understand how the materials, coating and number of heat links are crucial for the final temperature gradient.

5.2.1 Refrigeration power condition

Let's briefly describe the fundamental points of the cycle settled up to convert the heat flow condition for the refrigeration power into a temperature condition on the same surfaces.

For a simple example, we can consider all the radiative enclosures described in

the previous Section with all the surfaces with an emissivity of $\epsilon = 0.25$. The conductivity values $\kappa(T)$, for all the different materials used, are the higher limit curves in Figure 4.16. The number of heat links in the different locations is modified in (the nomenclature follows the description in Section 4.4.3):

- shield: 1,

- external surface of the bar: 0,

- inner support on the bar: 1,

- PTs' first stage bases: 4 each,

- PTs' second stage bases: 4 each.

The different steps can be summarized in:

1. The first step consists in performing a simulation with temperature values on the PTs bases that are supposed to be correct. Since the radiation shield is considered at a temperature of $40K$ and the inner bar at $4K$, these are the values that we can choose. The emissivity of the inner bar is quite high (worst scenario), therefore, the bar is supposed to reach a temperature higher than $4K$, so an initial temperature of $20K$ is chosen. These starting temperature conditions are represented in Figure 5.6.
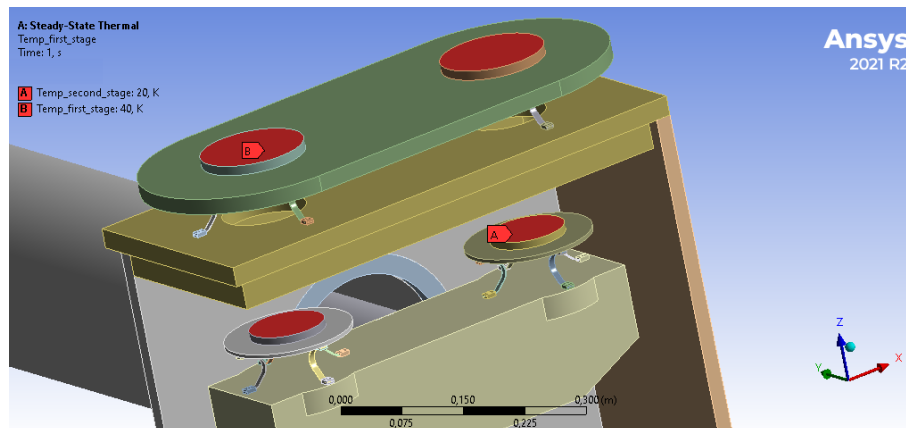
Figure 5.6. Starting temperature conditions on PTs bases for the first and second stages.

2. Once the simulation is finished, the total heat flux computed through the simulation can be read. The average value for this quantity on the bases will be used to find the proper curve in the capacity curve in Figure 4.6. The average will be performed using different heat flux probes over the surfaces, measuring them in a region away from the edges or the center. An example can be seen in Figure 5.7: four values are chosen for each PTs' first stage base while three are taken for the second stage.

   The Figure shows with a color scale the different values for heat flux on the whole simulated system. Almost all the different parts appear blue because
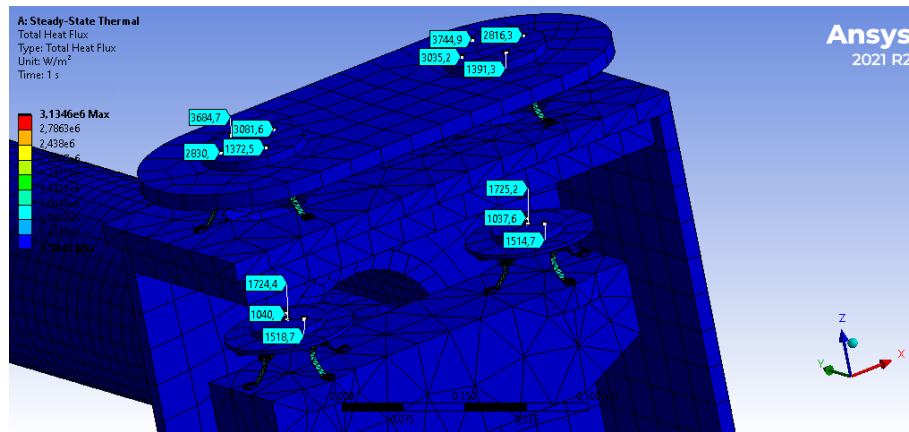
Figure 5.7. Different heat flux probes used to compute the average value for heat flux on the PTs bases.

the maximum value (red in the color legend in the Figure) is reached in the heat links: the foils of the visible heat links, indeed, are lighter.

The computation of the heat transfer rate involves the surfaces area, these values and the averaged heat fluxes are reported in the Table below:

Location	Heat flux [W/m^2]	Area [m^2]	Heat transfer rate [W]
First stage	2745	0.0132	36.2
Second stage	1427	0.00637	9.09

Table 5.1. Surfaces area values for the PTs bases and averaged heat fluxes for the simulation presented in Figure 5.6.

The last column in the Table reports the heat transfer rates that have to be used in the capacity curve.

3. Once the heat transfer rate for the chosen temperature has been computed, we can draw the interpolated curves on the capacity curve (see Figure 5.8). From their interception, we can find the new temperatures we have to impose on the surfaces for the new simulation.

   The new temperature for the simulation are $T_{first} = 49.5K$ and $T_{second} = 10.1K$.

4. The cycle can then restart from point 2 with the computation of the heat flux on the surfaces and the interpolation of the new heat transfer rate on the capacity curve. The cycle will stop when the new temperatures obtained with the interception of the interpolated curves will equal, within a certain tolerance, the temperatures used in the simulation just finished.

   In the example presented here, the cycle is stopped with a temperature of $52K$ on the first stage and $12K$ on the second. The heat fluxes are reported in Figure 5.9

Figure 5.8. Capacity curve with interpolated curves in red representing the heat transfer rate reported in Table 5.1. The blue lines represent the temperature on the first and second stages of the interception.
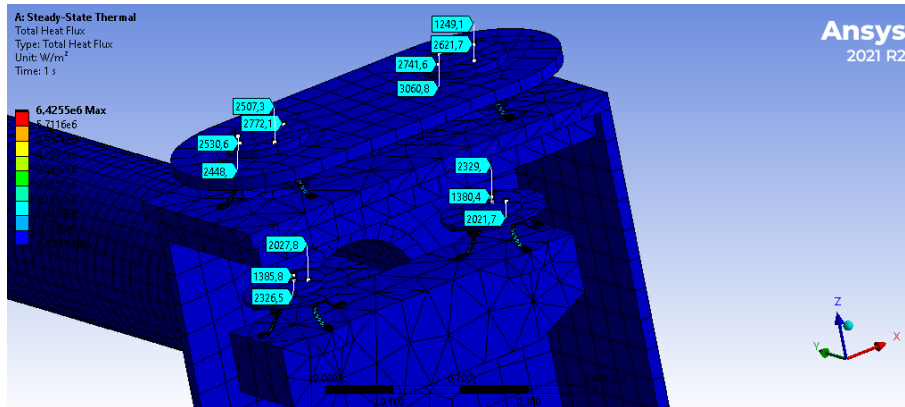
Figure 5.9. Heat fluxes on the PTs bases for the final simulation of the cycle with starting temperatures of $52K$ for the first stage and $12K$ for the second one.

The resulting values are then resumed in Table 5.2

Location	Temperature [K]	Heat transfer rate [W]
First stage	52	32.8
Second stage	12	12.2

Table 5.2. Final values for temperatures and heat transfer rates for the PTs bases.

The interpolation of the heat transfer rate obtained is presented in Figure 5.10: the temperatures of the interception of those values of heat transfer rate equal the temperatures used in the same simulation.
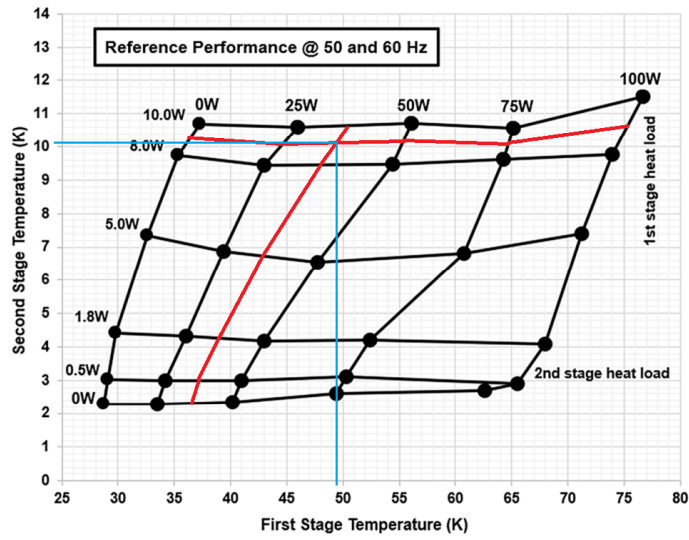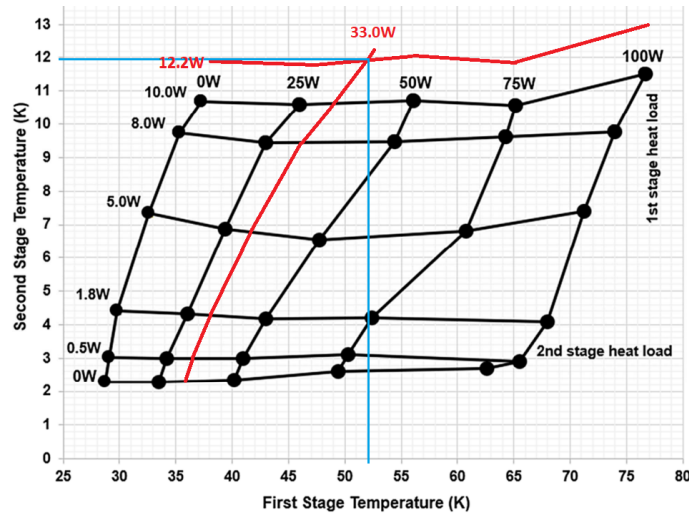
Figure 5.10. Capacity curve with interpolated curves in red representing the heat transfer rate reported in Table 5.2. The blue lines represent the temperatures on the first and second stages of the interception.

5.2.2 Simulations with upper limit values for conductivity

Since in Section 4.5 we presented different ranges for conductivity $\kappa(T)$, we have to perform different simulations using the upper and lower limits reported in Figure 4.16. In this Section, upper limit curves for Al 6N, Al 5N5 and Cu 5N (of the inner bar and heat links) are used; the next Section will, instead, use the lower limit of their ranges.

We can now start the description of the simulation's particularity. First of all, the number of heat links considered is summarized in Table 5.3.

Location	Heat links number
Shield	40
External surface of the bar	24
Inner support on the bar	12
PTs' first stage base	72
PTs' second stage base	42

Table 5.3. Heat links number for the simulation in different locations.

The number of heat links is then the maximum possible: this has to be varied in the following simulations because a lower number of heat links can be useful to lower the vibrations coming from the PTs. Although the number is the maximum possible, the simplified model will consider a lower number to guarantee a faster simulation. This can be obtained using the thermal circuit approach.

The first approximation can be made in the single heat link: the real model will be composed of three foils in parallel. Since their length and cross-sectional area can be considered the same, the simplified model can consider for each heat link a single

foil with a conductivity that is, following Equations 4.6 and 4.5:

$$R_{eq}^{parall} = \left(\frac{1}{\sum_i^3 R_i} \right)^{-1} = \left(\sum_i^3 \frac{\kappa A}{\Delta x} \right)^{-1} = \frac{\Delta x}{A} \frac{1}{3\kappa} = \frac{\Delta x}{A} \frac{1}{\kappa_3} \qquad (5.1)$$

in which $\kappa_3 = 3\kappa$ is the conductivity used for the single foil of each heat link in the simplified model. Furthermore, heat links in the same location can be considered in parallel and with the same length and cross-sectional area,

$$R_{eq}^{parall} = \left(\frac{1}{\sum_i R_i} \right)^{-1} = \left(\sum_i \frac{\kappa_3 A}{\Delta x} \right)^{-1} = \frac{\Delta x}{A} \frac{1}{\sum_i \kappa_3}. \qquad (5.2)$$

The conductivity has then to be modified by multiplying it by the number (i) of parallel heat links that have to be considered. The effective number of heat links can be summarized in Table 5.4:

Location	Number	Multiplier (heads)	Multiplier (foils)
Shield	4	10×	30×
External surface of the bar	4	6×	18×
Inner support on the bar	4	3×	9×
PTs' first stage base	4	18×	54×
PTs' second stage base	4	10.5×	31.5×

Table 5.4. Simplified model's heat links number for the simulation in different locations with the respective multiplier for conductivity.

The last two columns in the Table report the different multipliers applied to the conductivity at different locations to maintain the same equivalent resistance of heat links mentioned in Table 5.3. The first multiplier refers to the heat links heads that will consider only the parallel of the heat links; the last multiplier is the one used for the foils that will consider both the parallel of the foils and heat links.

Emissivity $\epsilon = 0.25$

We can report the results of the simulation that consider all the emissivity of the surfaces (see Section 5.1) with the value of $\epsilon = 0.25$. The refrigeration power condition has been modified into a temperature condition on the PTs bases following the cycle described in the previous Section.

The equilibrium temperature on the PTs bases are: $T_{first\,stage} = 80K$ and $T_{second\,stage} = 8.5K$. Figure 5.11 shows some temperature probes that allow us to understand some crucial points.

The major temperature variations take place in the heat links' site: their number and conductivity will have then an important role. The choice of emissivity $\epsilon = 0.25$ let us note that the shield will receive massive radiation that will raise its temperature over the wanted limits: the temperature of the experimental chamber's shield is $\sim 216K$ while it is preferred to remain under $100K$ to better reduce the radiation on the inner bar. The heat transfer rate coming from radiation will be crucial also in

Figure 5.11. Temperature gradient at equilibrium over the whole simplified model of PT cooling station. The simulation is performed with the upper limit values of conductivity for high purity materials and with an emissivity of all the surfaces of $\epsilon = 0.25$.

the equilibrium temperature of the PTs bases that will be double the planned value (around $40K$) for the first stage. Conversely, in the second stage, the temperature is $8.5K$ while it is planned to be of the order of $4K$. The aim of the shield is however maintained: starting from $8.5K$ on the PTs bases, the temperature gradient over the inner bar will rise until $\sim 8.64K$ on the experimental chamber's wall. A variation of $\Delta T = 0.14K$ will then take place, which is $\sim 1.6\%$ of the initial values: this would have been way higher without the shield.

We can perform a simulation with the same condition presented above without exploiting the thermal circuit approach for the bar's connection heat links.

As we can see from Figure 5.12, the equilibrium temperature of the PTs bases is the same as the case with the thermal circuit approach and also the temperature on the furthermost walls of the experimental chamber and its shield are almost the same. This validates the exploitation of the approximation that from now on will be used for all the simulations.

Emissivity $\epsilon = 0.15$

In this case, the simulation is performed under the same conditions as the previous one but with all the emissivity of the different surfaces of $\epsilon = 0.15$.

The equilibrium temperatures of the PTs bases are $64K$ on the first stage and $3.7K$ on the second. These values are lower than in the previous case because the emissivity considered in this case is lower: the radiative heat transfer rate is less than that in the $\epsilon = 0.25$ simulation, so the heat flux that will reach the PTs bases will be lower. The heat links are, anyway, the major cause of temperature variation and the temperature that will reach the experimental chamber's shield is still above the $100K$ limit. However, as in the previous case, the aim of the shield is preserved: the temperature gradient over the inner bar starts from $3.7K$ on the PTs bases (that is within the expected temperature range) and reaches a value of $\sim 3.72K$ on the

Figure 5.12. Temperature gradient at equilibrium over the whole simplified model of PT
cooling station. The simulation is performed with the upper limit values of conductivity
for high purity materials and with an emissivity of all the surfaces of $\epsilon = 0.25$. The
simulation is performed without the thermal circuit approach for the bar's connection
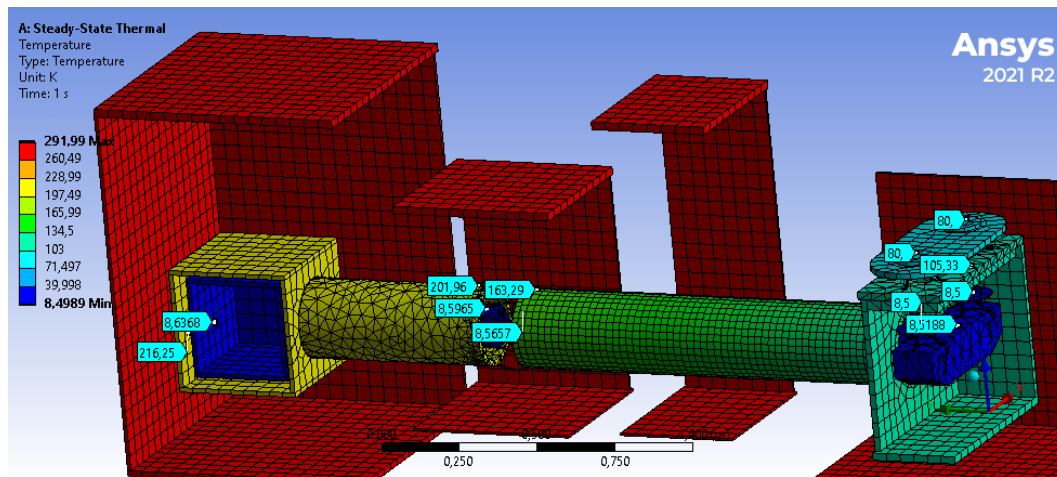heat links, the number of those heat links is then reported in Table 5.3.

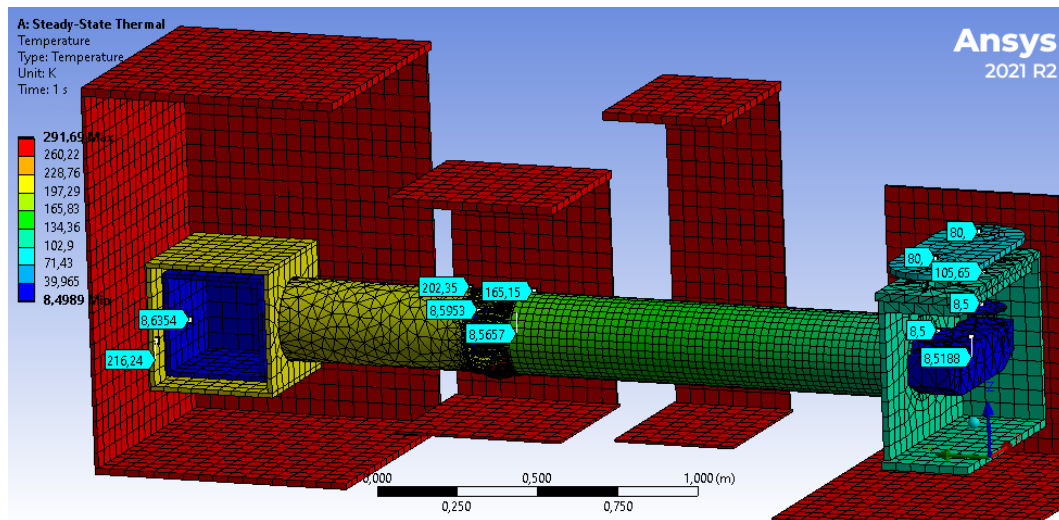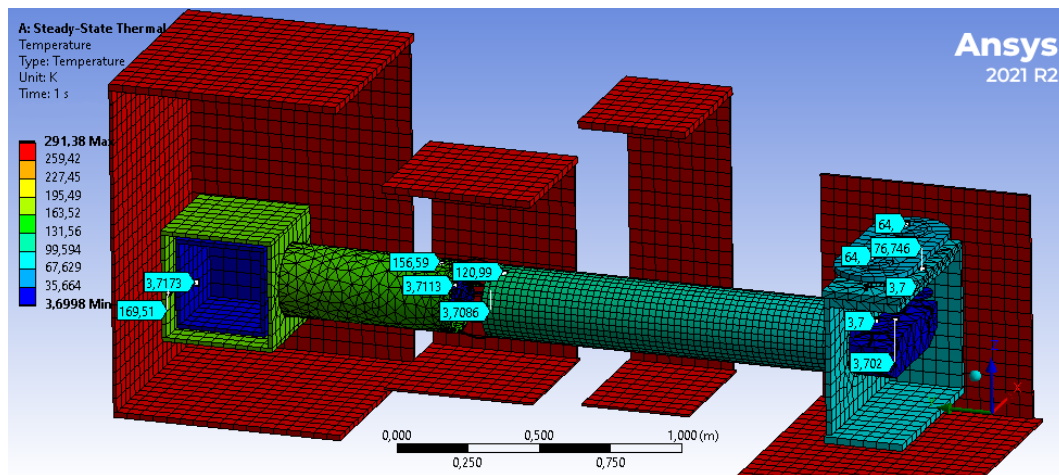**Figure 5.13.** Temperature gradient at equilibrium over the whole simplified model of PT
cooling station. The simulation is performed with the upper limit values of conductivity
for high purity materials and with an emissivity of all the surfaces of $\epsilon = 0.15$.

wall of the experimental chamber. The variation in temperature, in this case, is
$\Delta T = 0.017K$ which is $\sim 0.5\%$ of the initial temperature.

Heat links number variation

Since the aim of heat links is to thermally connect the different parts of the heat path while efficiently reducing the vibrations, we can try to perform simulations with a lower number of heat links. The vibrations that we want to reduce are especially the ones in the inner bar: it will, indeed, be connected to the cryogenic payload, so those vibrations will reach the mirror. A large number of heat links will create a robust connection that mechanically couples the parts with a lower reduction of vibration: on the thermal point of view, however, this will lead to a massive reduction of the thermal resistance making the heat connection more suitable. As already seen in the simulations, the major temperature variation takes place in the heat links location (both on the connection of the bar and below the PTs bases): if we reduce the number of heat links, the temperature variation is expected to rise. Since the vibrations have to be reduced on the inner bar, only the number of heat links connecting it will be modified while the external ones will remain the same (40 heat links on the shield and 72 below the PTs' first stage bases).
Such types of simulations are then performed and the results are reported in Tables 5.5 and 5.6. All the simulations consider the upper limits of the curves for the conductivity of high purity materials and the different emissivity are specified in the Tables.

Number	$T_{in}^{first\ stage}$ [K]	$T_{in}^{second\ stage}$ [K]	T_{end}^{shield} [K]	T_{end}^{bar} [K]
72-42-40-24-12	80	8.5	216.25	8.6368
72-42-40-12-12	80	8.5	216.18	8.6475
72-42-40-8-4	80	8.5	216.22	8.6902
72-42-40-0-4	80	8.5	216.22	8.7962
72-42-40-0-1	80	8.5	214.57	9.4748
72-24-40-24-12	80	8.4	216.19	8.5442
72-12-40-24-12	80	8.2	216.22	8.3607
72-4-40-24-12	80	8.0	216.25	8.2323

Table 5.5. PTs bases and furthermost wall of experimental chamber temperatures obtained from various simulations where the numbers of heat links connecting the inner bar are modified. The heat links' numbers are reported in the first column of the Table and they are in sequence: first stage - second stage - shield - external surface of the bar - inner support on the bar. Table refers to simulations performed with an emissivity of $\epsilon = 0.25$ for all the radiative surfaces.

From the first five rows of the Tables, we can see that the temperature in the furthermost wall of the experimental chamber (from the PTs) undergoes a little variation depending on the considered number of heat links in the connections. As we can expect, if the number of heat links in the connection between the two parts of the inner bar goes down, the radiative heat transfer rate on the experimental chamber's side will have more difficulties reaching the PTs bases: this will lead to an enhancement in the temperature on that side. Conversely, on the PTs side of the bar, the heat transfer rate will be less and this should lead to a lower heat flux on the bases, so their temperature condition is expected to be lower as the number of

Number	$T_{in}^{first\ stage}$ [K]	$T_{in}^{second\ stage}$ [K]	T_{end}^{shield} [K]	T_{end}^{bar} [K]
72-42-40-24-12	64	3.7	169.51	3.7173
72-42-40-12-12	64	3.7	169.51	3.7181
72-42-40-8-4	64	3.7	169.57	3.7214
72-42-40-0-4	64	3.7	169.61	3.7297
72-42-40-0-1	64	3.7	169.43	3.7748
72-24-40-24-12	64	3.7	169.51	3.7180
72-12-40-24-12	64	3.6	169.54	3.6203
72-4-40-24-12	64	3.5	169.53	3.5266

Table 5.6. PTs bases and furthermost wall of experimental chamber temperatures obtained from various simulations where the numbers of heat links connecting the inner bar are modified. The heat links' numbers are reported in the first column of the Table and they are in sequence: first stage - second stage - shield - external surface of the bar - inner support on the bar. Table refers to simulations performed with an emissivity of $\epsilon = 0.15$ for all the radiative surfaces.

heat links decreases. From those five rows, we cannot see this trend but this can be caused by the low precision in the conversion between the refrigeration power and temperature condition: in the real case, this trend is expected to be seen on the bases.

For all the different number combinations, the temperature on the furthermost wall of the experimental chamber's shield remains the same. This is what we expect because the number of heat links connecting the different parts of the shield (or the first stage of the PTs) is not modified during the simulations. The little variations in temperature of the inner bar, furthermore, will have a negligible effect on the final temperature gradient of the shield that will be mainly dependent on the $300K$ radiation of the vacuum chambers.

A particular example is the case where only one heat link is considered in the connection between the two parts of the bar: in this scenario, the symmetry of the whole heat transfer is broken and the heat transfer rate will undergo further difficulties flowing through the bar. This effect can be seen in the temperature value of the experimental chamber's wall: the variation in temperature with respect to the previous configuration is higher than that suffered with other configuration changes. The last three rows of the Tables show the same temperature values presented in the previous rows (on the PTs bases and in the experimental chamber's wall) but in this case, the number of heat links below the PTs bases is modified while heat links in the bar connection are maintained at their maximum value. Unlike the scenarios presented above, if the number of PTs heat links is modified, a variation of the temperature on the bases can be seen. This is caused by the fact that if we reduce the number of those heat links, all the radiation heat transfer rate will have difficulties reaching the bases (in the previous case, only a fraction of that heat transfer rate had this problem) so, that point becomes the bottleneck of the whole heat transfer. This leads to a reduction of the PTs' second stage bases' temperature as the number of heat links becomes lower. Since the parallel equivalent resistance of those heat links rises with the reduction of the number, also the difference in

temperature between the bases and the experimental chamber's wall increases.

5.2.3 Comparison with analytical solution

Before the analysis of the simulations with the lower limit curve for conductivity, we can make a simple calculation to verify that the simulation's outputs are reasonable. Let's consider for this purpose the simulation performed with the upper limit curve for conductivity, emissivity for all the surfaces of $\epsilon = 0.25$ and the maximum number of heat links (see Table 5.3). Since a complete predictive model of the whole cooling station is quite difficult to obtain due to the presence of both conductive and radiative heat transfer, we can compare the heat flux obtained with the simulation with the analytical computation of the heat transfer rate in different points of the model. The computation of the global energy contribution is, indeed, simpler to compute with respect to the temperature gradient along the bar and shield. At the equilibrium, in a steady-state simulation, the only contribution to the energy balance is given by the radiative heat transfer rate. Since the heat flows from the experimental chamber to the PTs bases (from the hotter to the colder side), we can make transverse sections in the model to take note of the heat flux in those points. We can then compare that heat flux with its analytical computation obtained following Stefan Boltzmann's law 4.11. Figure 5.14 shows a section of the bar and shield where three different vertical lines have been drawn. These lines indicate the transverse sections' locations where we can compare the heat contributions.
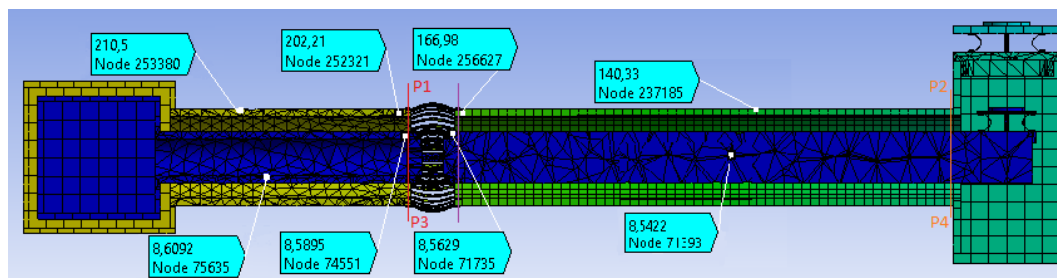
Figure 5.14. Section of the model. The three vertical lines show the locations where the analytical heat transfer rate and the simulated heat flux are compared.

Figure 5.15 shows the heat flux probes obtained in the simulation in the transverse sections described before. The leftmost figure represents the section indicated by the red line in Figure 5.14, the middle one is the purple line's one whilst the right side figure represents the heat flux probe in the orange line section.

We can average and summarize the heat flux in the different locations in the Table below:

We can now start the analytical computation of the radiative heat transfer rate. The computation of the radiative heat transfer rate for the red transverse section must consider, for the shield, the incoming radiation from the $300K$ vacuum chamber and the outgoing radiation toward the bar. Since the experimental chamber side of both the shield and the bar have a temperature gradient, we can choose an intermediate temperature for our calculation. We can then obtain the values for P_1
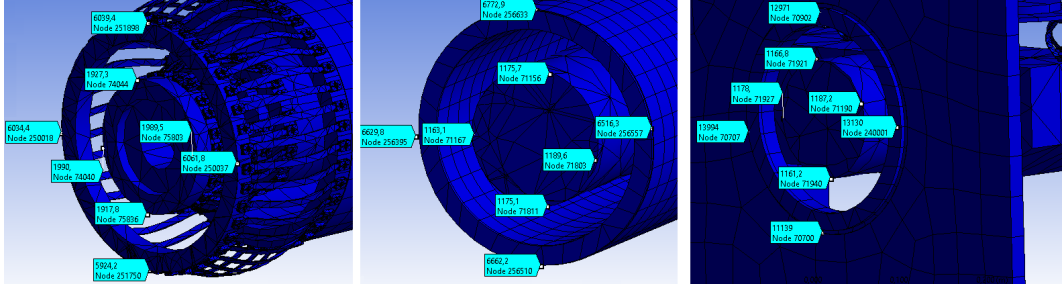
Figure 5.15. Simulated heat flux probe in different locations. The left side picture refers to the red line in Figure 5.14, the middle one to the purple line and, at last, the rightmost one to the orange.

Location	Red $[W/m^2]$	Purple $[W/m^2]$	Orange $[W/m^2]$	Area $[m^2]$
Shield	6015.0	6645.3	12808	0.0150
Bar	1956.2	1175.9	1173.3	0.0154

Table 5.7. Simulated heat flux in the different locations, the colors refer to the transverse sections described in Figure 5.14. The last column reports the cross-sectional area through which the flux has to be computed.

and P_3, i.e. the net radiative heat transfer rate for the shield and bar respectively,

$$
\begin{aligned}
P_1 &= \epsilon\sigma[1.47m^2 * (300^4 - 210^4)K^4 - 1.36m^2 * (210^4 - 8.6^4)K^4] = 90.8W \\
P_3 &= \epsilon\sigma[0.90m^2 * (210^4 - 8.6^4)K^4] = 22.0W
\end{aligned}
\tag{5.3}
$$

where the respective radiative areas have been calculated. The expected heat fluxes are then computed using the cross-sectional areas reported in Table 5.7:

$$
F_1 = \frac{90.8W}{0.0150m^2} = 6053.3\frac{W}{m^2} \qquad F_3 = \frac{22.0W}{0.0076m^2} = 2894.7\frac{W}{m^2}.
\tag{5.4}
$$

where we consider the cross-sectional area for the bar $A_{bar} = 0.0076m^2$ because the bar in the experimental chamber side is hollow. As we can see, the value for the heat flux in the shield is equal to the simulated one while the bar's value is a bit higher: this may be caused by the relevance of the view factor in a smaller enclosure. We can, however, point out that the simulated heat flux probes follow the expectation within the errors caused by view factors.

The radiative heat flux has now to be carried by heat links to the other part of the bar and shield. Since the computation of the expected temperature variation between the two ends of the heat links is quite difficult to obtain (because we have to consider both the contribution of radiation and conduction), we can make a quick check for the efficiency in the heat transfer, computing the heat flux at the beginning of the other part of the bar, just beyond the heat links (purple section). If we suppose that heat links carry the whole heat transfer rate, the value for the flux beyond them isn't equal to that before the gap. The simulated value for the

heat flux is $6645.3 W/m^2$ which corresponds to $99.7W$. This higher value for the heat transfer rate is given by the additional radiative heat transfer rate on the heat links. These have a little radiative area, but if we consider all the 40 heat links in the shield, the radiative surface becomes considerable. We have also to consider the additional surface where heat links rest. The contribution of heat transfer rate can then be computed,

$$P_{links}^{shield} = \epsilon\sigma[0.08m^2 * (300^4 - 184^4)K^4 - 0.06m^2 * (184^4 - 8.57^4)K^4] = 6.9W. \quad (5.5)$$

The expected value is then $97.7W$ which is similar to the simulated one.
In the same way, in the bar connection, the additional contribution is

$$P_{links}^{bar} = \epsilon\sigma[0.06m^2 * (184^4 - 8.57^4)K^4] = 0.97W. \quad (5.6)$$

The expected heat flux is then

$$F_{links}^{bar} = \frac{22.97W}{0.0154m^2} = 1491.6\frac{W}{m^2}. \quad (5.7)$$

This value is still higher than the simulated one: we can, however, make the same consideration about the view factor also in this scenario.
At last, we can consider the energy balance at the end of the shield/bar before the chamber where PTs are housed: the computation of radiative heat transfer rate in that site would be difficult because of the shape of the bar and shield, so the view factors would have a major role. We can calculate the additional heat transfer rate given by radiation in the two concentric cylinders. Let's call P_2 the additional heat transfer rate for the shield and P_4 the one for the bar:

$$\begin{aligned} P_2 &= \epsilon\sigma[1.08m^2 * (300^4 - 140^4)K^4 - 0.91m^2 * (140^4 - 8.54^4)K^4] = 113.2W \\ P_4 &= \epsilon\sigma[0.58m^2 * (140^4 - 8.54^4)K^4] = 3.2W \end{aligned} \quad (5.8)$$

The expected total heat fluxes at the orange transverse section are then

$$F_{TOT}^{shield} = \frac{210.9W}{0.0150m^2} = 14060\frac{W}{m^2} \qquad F_{TOT}^{bar} = \frac{26.17W}{0.0154m^2} = 1699.4\frac{W}{m^2}. \quad (5.9)$$

The flux in the shield agrees with the expectation while the bar's one is still higher than the expected one. However, comparing the simulated heat flux in the purple section with that in the orange section of the bar, we can see that those values are similar. The additional heat transfer rate in the bar is $3.2W$ so a variation in the heat flux of $\sim 200W/m^2$ is expected. This missing flux can be explained, as usual, with the view factors that, especially in the bar's orange transverse section, are relevant in the calculation of the radiative heat transfer.
Although the simulated energy balance in the inner bar is dissimilar to the expectation, the shield's balance follows the analytical calculation: we can then use these results to demonstrate that the simulation outputs can be considered rightful.

5.2.4   Simulations with lower limit values for conductivity

We can now report simulations performed with the lower limit curves for high purity materials. Following the same scheme of the previous Section, simulations with different values for emissivity ϵ (0.25 and 0.15) are firstly presented with the heat links' number that is reported in Table 5.3 (the thermal circuit approach will be however considered, so the effective number that the simulation will use is the one reported in Table 5.4); then, variations in the number of heat links will be considered.

Emissivity $\epsilon = 0.25$

The first simulation reported is the one with an emissivity of $\epsilon = 0.25$.

Figure 5.16. Temperature gradient at equilibrium over the whole simplified model of PT cooling station. The simulation is performed with the lower limit values of conductivity for high purity materials and with an emissivity of all the surfaces of $\epsilon = 0.25$.

The equilibrium temperature of the PTs bases are: $T_{first\,stage} = 77K$ and $T_{second\,stage} = 8.3K$. Figure 5.16 shows the same temperature probes shown in the simulations performed with the upper limit of the curves. We can focus on the differences between this simulation and the analogous with the upper limit.

One of the first differences we can see is the temperature on the PTs bases. Focusing on the shield, we can see that, in this case, the equilibrium temperature on the first stage bases is $77K$ while, with the upper limit, we got $80K$. This is mainly due to a different temperature on the inner bar rather than the different curves used for the conductivity. The lower and upper limits of this quantity, indeed, start to differ one from the other below $\sim 50K$: the temperature gradient on the shield, instead, starts from a value of $77K$, so the heat transfer rate should undergo the same resistance of the upper limit case. This can be seen also studying the absolute value of the temperature difference between the PTs bases and the furthermost wall of the experimental chamber. In the upper limit simulation, this value is $\Delta T = 136.25K$ while in the lower limit it is $\Delta T = 137.72K$: these values are similar and their difference of $\sim 1.5K$ is less than 1% considering an average temperature on the

shield of $\sim 160K$. This result shows us that the equivalent resistance through the whole shield of the cooling station will be the same in the upper and lower limit cases.

The effects of the massive changes in the values for conductivity can be seen in the inner bar: below the temperature of $10K$, the conductivity upper and lower limit curves assume values that differ one from the other by more than one order of magnitude. We can see the consequences of this both in the temperature value of the PTs' second stage bases and in the absolute value of the temperature difference. The temperature on the bases, in the lower limit case, is $8.3K$ which is less than the equilibrium temperature found for the upper limit case: this shows us that the heat connection through the PTs heat links is worse than in the other case. The two curves, for a temperature of $8K$, have more than one order of magnitude of difference in the conductivity: this increases the equivalent resistance by the same amount, making harder the heat flow. The first evidence of this can be seen in the temperature difference between the PTs bases and the hammer shape surface of the bar. In the upper limit case, this value is $\Delta T \sim 0.02K$ which is 0.22% of the initial temperature; in the lower limit, this value becomes $\Delta T \sim 0.15$ which, in this case, is 1.77% of the initial temperature. Since this difference is less than one order of magnitude, i.e. the variation of resistance in the two cases, the heat transfer rate on the bases will also be less in the lower limit case (following Fourier's law 4.4) and this will explain the lower equilibrium temperature on the bases. The same argument can be made for the heat links connecting the two parts of the bar.

At last, if we consider the absolute value of temperature difference between the second stage bases and the experimental chamber wall, we can find the value of $\Delta T = 0.14K$ for the upper limit while $\Delta T = 0.84K$ for the lower limit cases. The variation, with respect to the starting temperature of the bases, is $\sim 1.65\%$ for the upper and $\sim 10.12\%$ for the lower cases: the proportion between the two follows the one found for the PTs heat links.

Emissivity $\epsilon = 0.15$

In this case, all the emissivities of the different surfaces are fixed at a value of $\epsilon = 0.15$.

The equilibrium temperature of the PTs bases are: $T_{first\ stage} = 58K$ and $T_{second\ stage} = 3.3K$. Figure 5.17 can be described following all the considerations made in the previous case for the simulation with lower limit curves (with an emissivity of $\epsilon = 0.25$). Focusing on the differences between this simulation and the analogous performed with the upper limit curve for conductivity, we can notice, also in the $\epsilon = 0.15$ case, that the PTs first stage bases temperature is lower than the upper limit scenario. Even in this case, we can explain this with the differences in temperature in the inner bar rather than with the different conductivity curves used. The absolute values of the temperature difference between the first stage bases and the wall of the experimental chamber's shield are, indeed, similar: $\Delta T = 105.5K$ for the upper limit curve and $103.4K$ for the lower limit.

The effects of the different choices of curves for the conductivity can be seen in the temperature gradient of the inner bar. It follows the same trend of the gradient
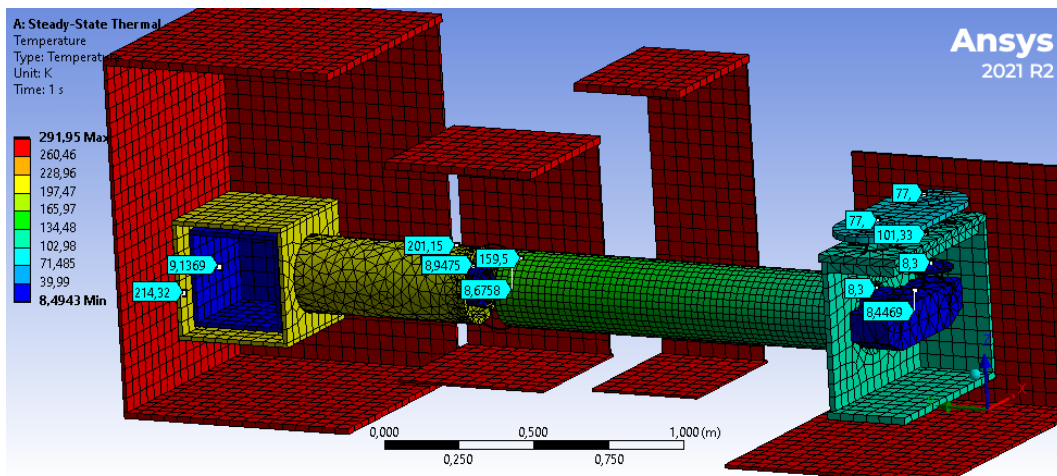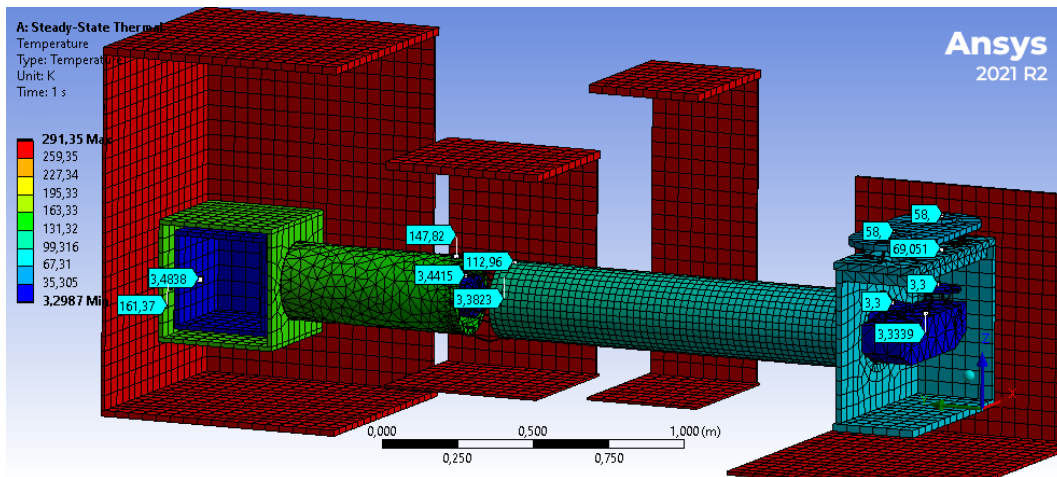
Figure 5.17. Temperature gradient at equilibrium over the whole simplified model of PT
cooling station. The simulation is performed with the lower limit values of conductivity
for high purity materials and with an emissivity of all the surfaces of $\epsilon = 0.15$.

described for the $\epsilon = 0.25$ case. The first, important, difference is the PTs' second
stage equilibrium temperature which is $3.3K$. With the combination of lower
conductivity values and lower radiative heat transfer rate, the temperature will be
lower in the bases but the refrigeration power cannot sustain its role till the end
of the experimental chamber. The absolute value of the temperature difference is,
indeed, $\Delta T = 0.18K$ that is $\sim 5.45\%$ of the initial temperature, a value that exceeds
the one found for the $\epsilon = 0.25$ simulation; in this case, the ratio is larger because,
although the radiative heat transfer rate will be lower with an inferior emissivity,
the lower limit for conductivity reduces the conduction heat transfer rate by one
order in magnitude.

Heat links number variation

The tables below report simulations with variations in the number of heat links
in the connection of the bar and below the PTs bases. Only the heat links connecting
the inner bar are modified in their number because we want to reduce the vibrations
mainly in the heat path that will connect the payload.

The trend for the temperature gradient with the variation of the number of heat
links follows all the considerations made for the upper limit curve for conductivity.
The effect of the inferior values of conductivity can be seen in the temperature of the
furthermost wall of the experimental chamber. While the trend follows that of the
upper limit curve, the absolute value of the temperature becomes quite high as the
number gets lower. A particular case is that of the simulation with only one heat link
connecting the two bars. Especially in the $\epsilon = 0.25$ case, the experimental chamber's
wall temperature reaches a value of $\sim 15K$. This value cannot be accepted in the
real application and it is useful to understand the need for a reasonable number of
heat links for the connections.

Number	$T_{in}^{first\ stage}$ [K]	$T_{in}^{second\ stage}$ [K]	T_{end}^{shield} [K]	T_{end}^{bar} [K]
72-42-40-24-12	77	8.3	214.32	9.1369
72-42-40-12-12	77	8.3	214.37	9.2320
72-42-40-8-4	77	8.3	214.33	9.2136
72-42-40-0-4	77	8.3	215.31	10.415
72-42-40-0-1	77	8.3	215.02	14.955
72-24-40-24-12	77	8.2	214.76	9.3206
72-12-40-24-12	77	8.2	214.76	9.4074
72-4-40-24-12	77	8.1	214.73	19.92

Table 5.8. PTs bases and furthermost wall of experimental chamber temperatures obtained from various simulations where the numbers of heat links connecting the inner bar are modified. The heat links' numbers are reported in the first column of the Table and they are in sequence: first stage - second stage - shield - external surface of the bar - inner support on the bar. Table refers to simulations performed with an emissivity of $\epsilon = 0.25$ for all the radiative surfaces.

Number	$T_{in}^{first\ stage}$ [K]	$T_{in}^{second\ stage}$ [K]	T_{end}^{shield} [K]	T_{end}^{bar} [K]
72-42-40-24-12	58	3.3	161.37	3.4838
72-42-40-12-12	58	3.3	161.37	3.5046
72-42-40-8-4	58	3.3	161.37	3.5879
72-42-40-0-4	58	3.3	161.41	3.7830
72-42-40-0-1	58	3.3	161.40	4.6949
72-24-40-24-12	58	3.2	161.25	3.4071
72-12-40-24-12	58	3.2	161.22	3.4492
72-4-40-24-12	58	3.1	161.16	3.5223

Table 5.9. PTs bases and furthermost wall of experimental chamber temperatures obtained from various simulations where the numbers of heat links connecting the inner bar are modified. The heat links' numbers are reported in the first column of the Table and they are in sequence: first stage - second stage - shield - external surface of the bar - inner support on the bar. Table refers to simulations performed with an emissivity of $\epsilon = 0.15$ for all the radiative surfaces.

All the simulations, both with the upper or lower limit curves for conductivity, show the effective need for the radiative shield that, as expected, will reduce the radiative contribution from the $300K$ vacuum chambers on the inner bar. The temperature on the inner bar is, indeed, preserved from the PTs bases till the furthermost wall of the experimental chamber within a factor of $0.5 - 1.6\%$ of the initial temperature when the upper limit curve is considered whilst within a factor $5 - 10\%$ with the lower limit. When the payload and its cryostat are considered, the amount of radiation that will reach the pulse tubes will be higher; for this reason, a lower temperature gradient would be a better choice. This can be obtained considering a special refinement for the surfaces of all the parts that are considered in the cooling station. A polishing treatment could be performed on those surfaces but the shape and purity of the parts could be a problem in the real application.

Therefore, the emissivity that can be reached with this treatment is of the order of $\epsilon = 0.05$. Simulations with the upper and lower limit curves for conductivity with this value of emissivity can, however, be performed.

5.2.5 Polishing treatment

Although this type of coating could be useful to reduce the radiation in the shield, it is quite difficult to realize for our purpose. However, we can perform simulations to understand the relevance that it would have.

As already mentioned, the emissivity that we can use is $\epsilon = 0.05$ and we can present both the simulations with the upper and lower limit curves for conductivity to have the entire possible range for the temperature gradient varying the conductivity. The simulation will be performed with the maximum number of heat links exploiting the thermal circuit approach (their number is reported in Table 5.4).

Upper limit curve

Figure 5.18. Temperature gradient at equilibrium over the whole simplified model of PT cooling station. The simulation is performed with the upper limit values of conductivity for high purity materials and with an emissivity of all the surfaces of $\epsilon = 0.05$.

Lower limit curve

Both simulations show that with the reduction of the emissivity, the shield temperature and its gradient will decrease. The equilibrium temperature on the PTs' first stage bases is $37K$ for both the curves and this is because of the massive variation between the two starts at a temperature below $10K$. The value of $37K$, therefore, is within the range of values that we want for the real application shield. The absolute value of temperature difference, furthermore, is way lower than in the previous cases: in this case, we have a value of $\sim 17K$ which is $\sim 45\%$ of the initial
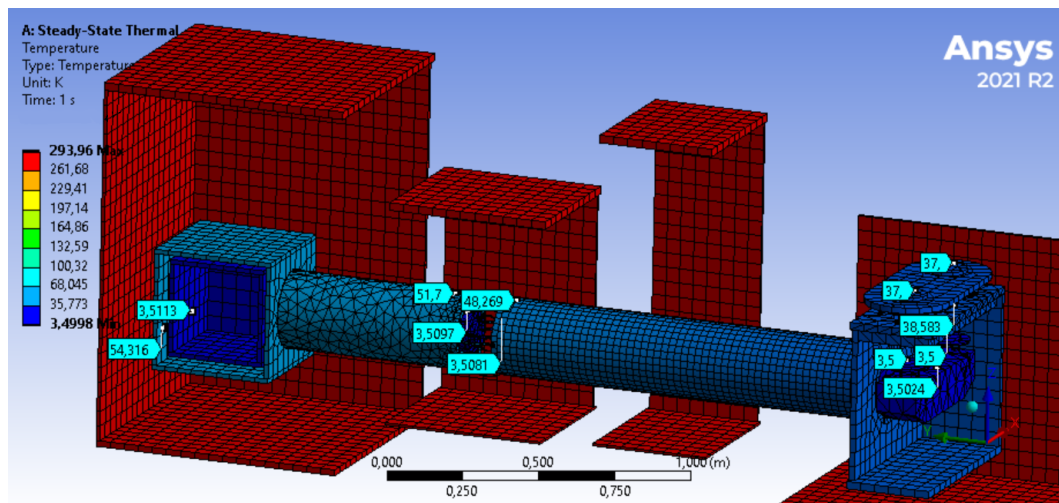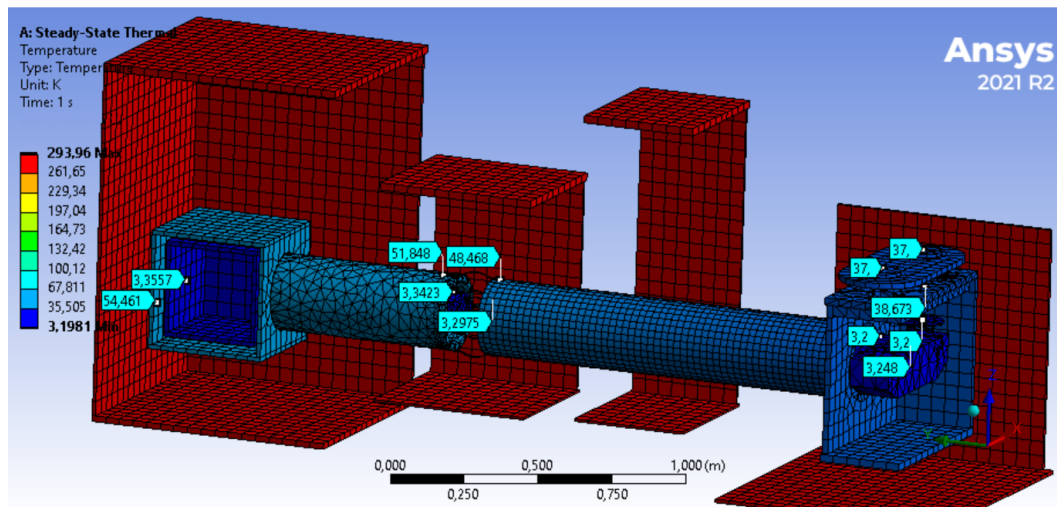
Figure 5.19. Temperature gradient at equilibrium over the whole simplified model of PT cooling station. The simulation is performed with the lower limit values of conductivity for high purity materials and with an emissivity of all the surfaces of $\epsilon = 0.05$.

temperature. In the previous case, this value was in the range $100 - 200\%$ of the initial temperature.

Since the temperature of the whole shield is maintained well below the value of $100K$, the radiative input from the shield to the inner bar is lower and this can be seen both in the equilibrium temperature of the second stage bases and in the absolute value of the temperature difference. Between the two simulations, we can see differences in the PTs' second stage bases: this is caused by the difference of more than one order of magnitude in the conductivity curves that happens at the temperature of $3 - 4K$. In the upper limit case, the equivalent resistance of the heat links will be lower and the heat flux on the bases would be higher: this leads the bases' temperature to get higher. Therefore, the temperature difference between the bases and the experimental chamber's wall will be less. Conversely, with the lower limit curve, the heat flux on the bases is lower (and their temperature is less than in the other case) but the temperature difference is higher than that with the upper limit. In the former situation, indeed, the temperature difference between the second stage bases and the furthermost wall of the experimental chamber is $0.0113K$ which is $\sim 0.32\%$ of the initial temperature: this number is lower than $\sim 1.6\%$ and $\sim 0.5\%$ respectively for the case of $\epsilon = 0.25$ and $\epsilon = 0.15$ (both with the upper limit curve). In the latter case, i.e. with the lower limit curve, the temperature difference is $0.1557K$, that is 4.87% of the initial temperature: this value is, anyway, less than that of the other emissivity cases (10.1% for $\epsilon = 0.25$ and 5.57% for $\epsilon = 0.15$).

A variation in the emissivity can be, then, useful to reduce the incoming radiation on the shield and to reduce its temperature gradient: this will also reduce the radiation to the inner bar that will reach a lower temperature. Another possible solution to reduce the radiation on the shield is the use of a super-insulation system between the shield and the vacuum chamber.

5.2.6   Super-insulation system: Mylar

A super-insulation system is a multilayer insulation that uses stacks of low-emittance metalized sheets (Mylar) separated by low-conductance spacers surfaces that prevent adjacent layers from contacting. In this way, the multiple radiative enclosures within the multilayer will reduce the incoming heat transfer rate by acting as an insulator. Each metalized sheet and spacer has a thickness of the order of μm and the effective insulation properties of the multilayer depend upon the number of sheets packed together. Thanks to the low thickness of each sheet, the multilayer system has a global thickness of few mm, e.g. 40 layers of Mylar have a thickness of about $20mm$. Several empirical formulas can be found in the literature to understand the insulation efficiency and the resulting heat flux when a super-insulation system is used. Typical values of $2\frac{W}{m^2}$ can be considered when ~ 50 layers of Mylar are considered between the temperature of $300K$ and $< 100K$. This value, following Boltzmann's law (Equation 4.8), can be converted into an emissivity value:

$$\frac{P_{rad}}{A} = \epsilon_{Mylar}\sigma(T_1^4 - T_2^4) \;\; \rightarrow \;\; \epsilon_{Mylar} = \frac{P_{rad}}{A\sigma(T_1^4 - T_2^4)} \tag{5.10}$$

where Boltzmann's law is considered without taking into account the view factors. A value of $\epsilon_{Mylar} = 0.0043$ can be obtained using the reported heat flux value. This number is similar to those obtained with the various empirical formulas[8][26].
This super-insulation system can be used in the PT cooling station between the shield and the vacuum chamber. Since the implementation of the various layer of Mylar would increase too much the simulation time, a value of $\epsilon_{Mylar} = 0.0043$ can be used for the external surface of the shield. This will modify, then, the enclosure number 1 (see Section 5.1) with respect to the previous simulations. We can perform the same set of simulations made in the previous Sections with this value of emissivity. The upper and lower limit curve for high purity material's conductivity can be considered while the other surfaces' emissivity can be modified between $\epsilon = 0.25$ and $\epsilon = 0.15$.

Upper limit curve

In Figures 5.20 and 5.21, we can see that the lower value of the shield's external surface's emissivity leads the whole shield to assume a lower temperature value. As we can expect, since the emissivity chosen is $\sim 0.2\%$ of the one considered for the polishing case, the PTs bases equilibrium temperature is lower than that obtained in that case. The temperature difference between the bases and the furthermost wall of the experimental chamber's shield is lower in both the emissivity cases considered with respect to the $\epsilon = 0.05$ simulation. The previous value of $\sim 45\%$ of temperature enhancement with respect to the bases' temperature of the first stage is reduced to a value of $\sim 10\%$ in both cases: we can see, however, a different trend in the temperature difference. While in the previous case, with the same emissivity on all the surfaces, the temperature difference between the bases and the experimental chamber's shield wall was lower with a minor value of emissivity (because the radiative heat transfer rate incoming from the vacuum chamber was lower), in this case, that value increase as the emissivity get lower because the surfaces will radiate less radiation towards the bar. We can see this trend in the two simulations reported

Figure 5.20. Temperature gradient at equilibrium over the whole simplified model of PT cooling station. The simulation is performed with the upper limit values of conductivity for high purity materials. The emissivity of all the surfaces is $\epsilon = 0.25$ and Mylar on the shield is considered.
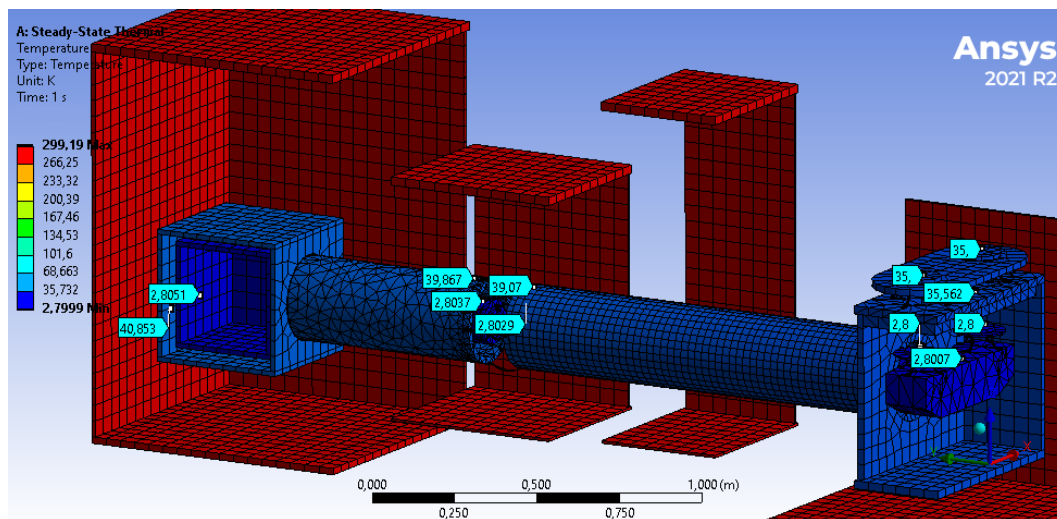
Figure 5.21. Temperature gradient at equilibrium over the whole simplified model of PT cooling station. The simulation is performed with the upper limit values of conductivity for high purity materials. The emissivity of all the surfaces is $\epsilon = 0.15$ and Mylar on the shield is considered.

above: with $\epsilon = 0.25$, the temperature difference is $3.36K$ while with $\epsilon = 0.15$ the difference is $5.85K$.

Focusing on the bar, the temperature of the PTs' second stage bases is lower than any other simulation made before and this is expected because the radiative heat transfer rate incoming from the shield is lower. Both the simulations, with different

emissivity value, have an analogous temperature difference between the bases and the chamber: this is caused by the similar temperature gradient on the shield.

Lower limit curve
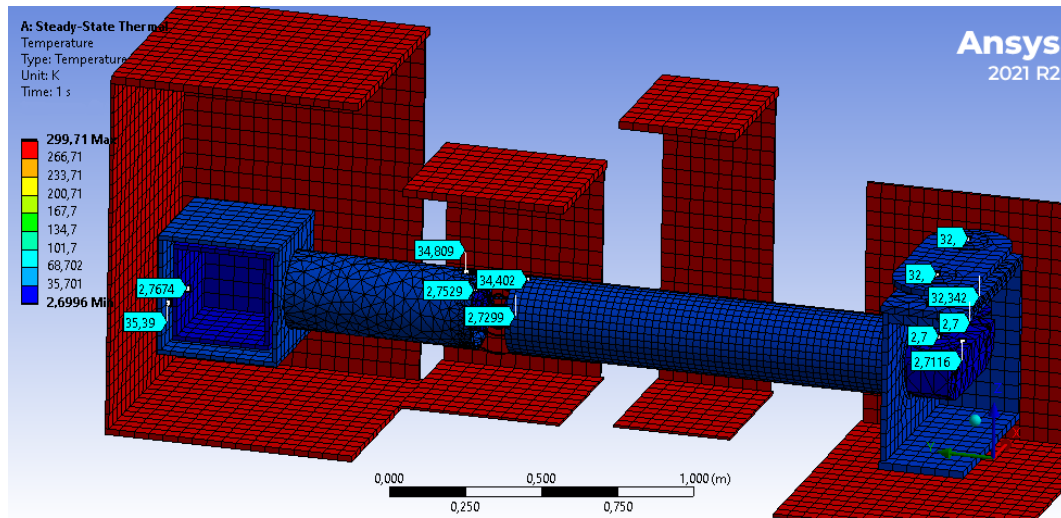
Figure 5.22. Temperature gradient at equilibrium over the whole simplified model of PT cooling station. The simulation is performed with the lower limit values of conductivity for high purity materials. The emissivity of all the surfaces is $\epsilon = 0.25$ and Mylar on the shield is considered.
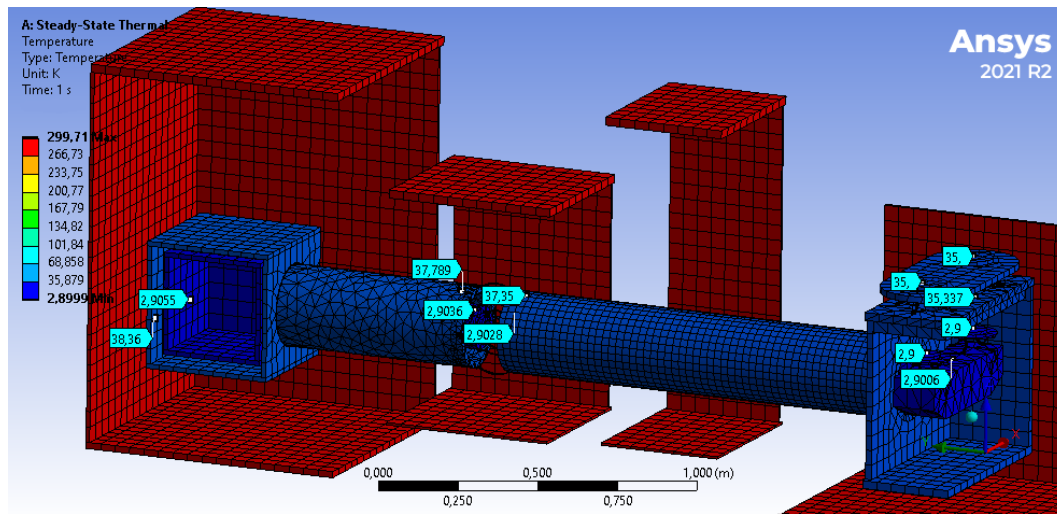

Figure 5.23. Temperature gradient at equilibrium over the whole simplified model of PT cooling station. The simulation is performed with the lower limit values of conductivity for high purity materials. The emissivity of all the surfaces is $\epsilon = 0.15$ and Mylar on the shield is considered.
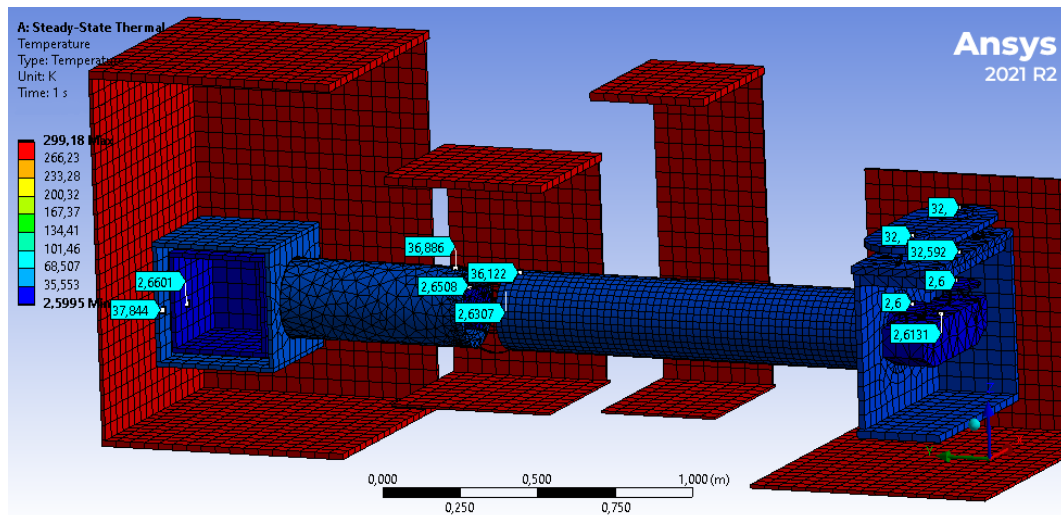
Simulations with the lower limit curve for conductivity follow the ones performed with the upper limit. As already explained in the previous Section, the lower conductivity leads the bases to get an equilibrium temperature a bit lower than that with the upper limit because the equivalent resistance in the connection points rise and the heat flux will have more difficulties reaching the bases. Both simulations have a difference of $3K$ on the first stage temperature while there's a $0.2K$ difference in the second stage.

The differences caused by the different curves can be seen, as usual, in the inner bar: the temperature difference in both cases is $\sim 2.3 - 2.5\%$ of the second stage temperature while in the upper limit case this value is $\sim 0.18 - 0.19\%$. Anyway, the temperature on the experimental chamber walls with the lower limit curve is still the lowest of all the simulations performed.

5.2.7   The problem of the bar's aperture

All the simulations performed till now consider four different enclosures, each with their own ambient temperature that we have to impose because they cannot be considered perfect enclosures (see Section 5.1). Although we saw in Section 5.2.2 that the thermal circuit approach is a good approximation for the global temperature gradient, we have to stress that the simulations are performed with another approximation.

Figure 5.24. Heat links in the connection part of the bar. Different colors are used for the different enclosures.

As we can see in Figure 5.24, the upper surfaces of the heat links of the shield are considered within enclosure number 1 (red in the Figure): this enclosure has an ambient temperature of $300K$ because at the equilibrium it will have a temperature given by the vacuum chambers' radiation. This enclosure cannot be considered perfect because it has an aperture in the heat links location. Enclosure number 2 is formed by the interior surfaces of the shield and the shield's heat links (green in the Figure) and by all the surfaces of the bar and bar's heat links (yellow in the Figure).

This enclosure has an ambient temperature of $40K$ because at the equilibrium the temperature of the bar will be settled by the shield's radiation (whose temperature is considered $\sim 40K$). In the aperture, the $300K$ radiation, however, will pass through the heat links because they are separated one from the other and it will heat up the inner heat links' surfaces or, through scattering, directly the bar.

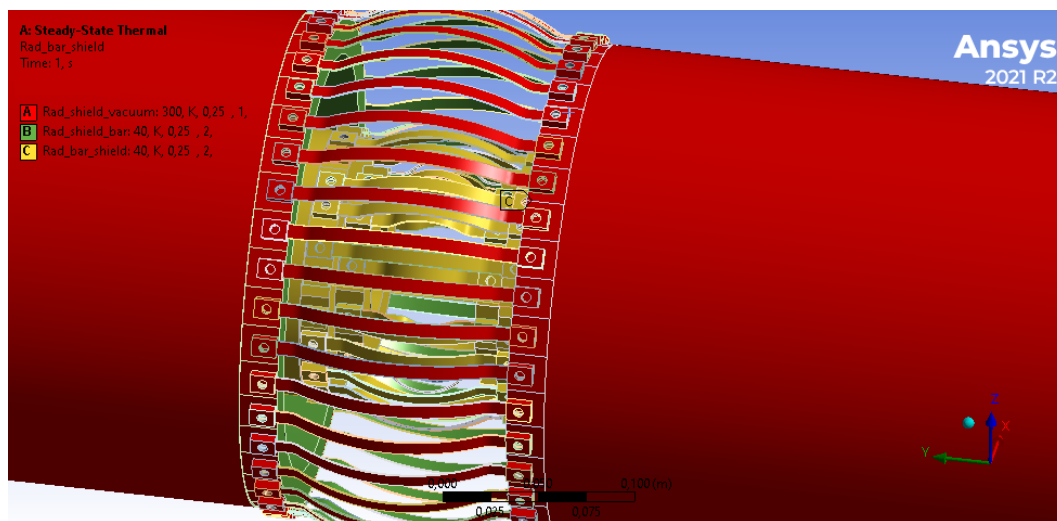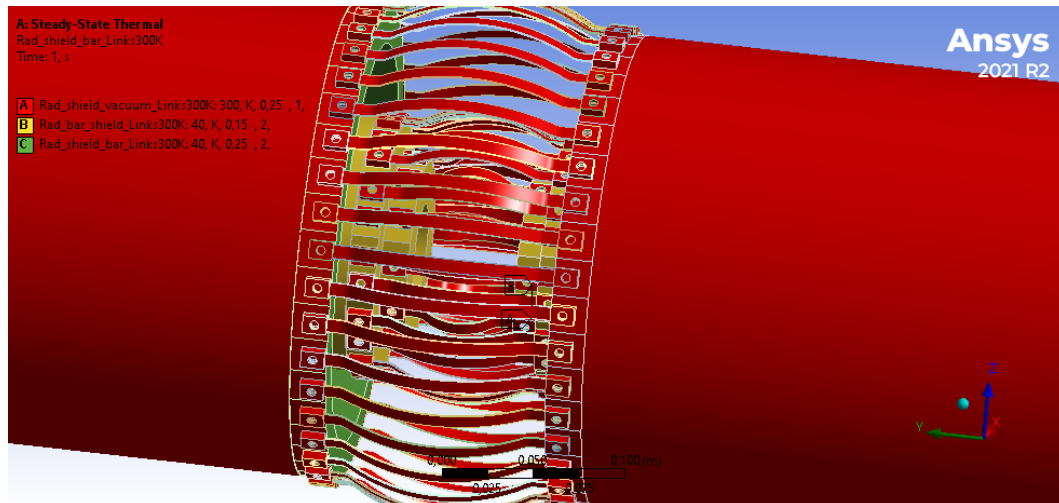**Figure 5.25.** Heat links in the connection part of the bar. Different colors are used for the different enclosures.

We can see the relevance of this effect by performing two different simulations: using the same conditions, i.e. upper limit curves for conductivity and emissivity for all the surfaces $\epsilon = 0.25$, we can do a simulation in which the enclosures remain the same as before (see Figure 5.24) and one other where all the heat links (the shield and the inner ones) are considered in enclosure number 1 with an ambient temperature of $300K$ (see Figure 5.25: all the surfaces of the heat links are red, so they are considered in enclosure number 1).

In the former case, the result we obtain is the same reported in Figure 5.11. A zoom of the temperature gradient over all the heat links is reported in Figure 5.26.

The latter case is reported in Figure 5.27.

We can see, in this last case, that the shield will be at a higher temperature than the case of two different enclosures. This is because, while considering a single enclosure, also the inferior surfaces of the foils will radiate with an ambient temperature of $300K$.

Focusing on the interior heat links, we can see that the absolute value of the temperature at the two ends of the connection is a bit higher than in the case with different enclosures: this is what we expected because of the hotter surface from which the radiation comes. The temperature difference between the two ends of the link is quite the same but in the one enclosure case is a bit higher.

This effect is expected to have some consequences also for the transient simulations. In those cases, constant radiation from surfaces at $300K$ till the innermost heat links in the bar, would reduce the cooling efficiency resulting in an enhancement of the
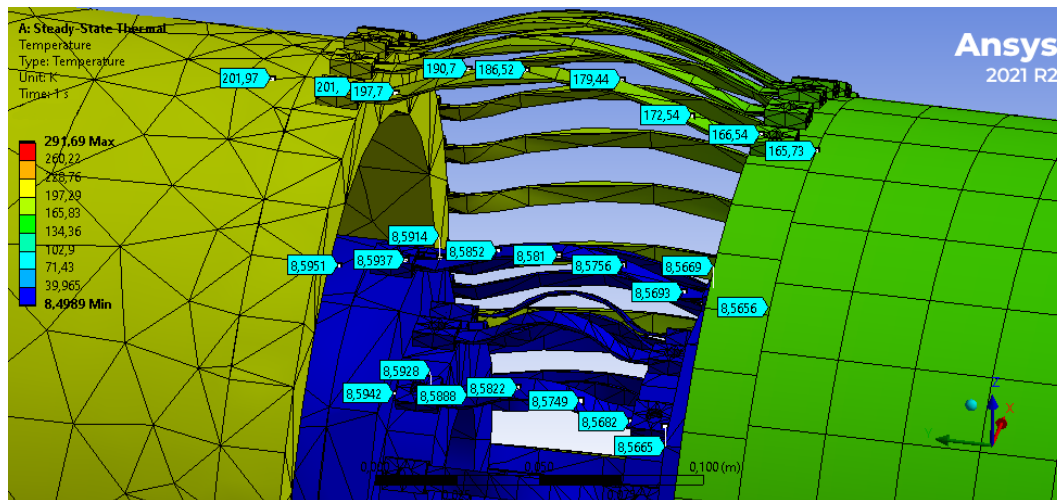
Figure 5.26. Temperature gradient over all the heat links when two different enclosures are considered in the simulation.
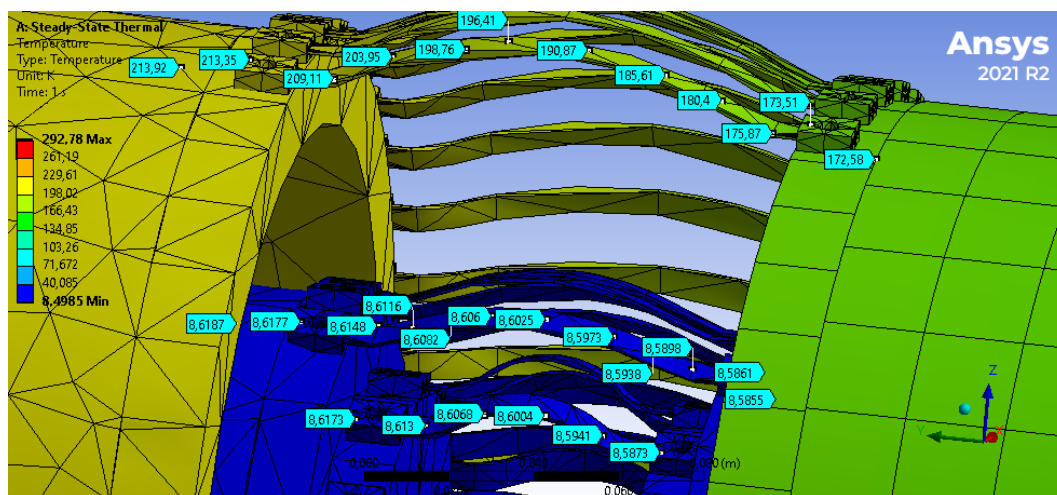
Figure 5.27. Temperature gradient over all the heat links when only one enclosure is considered for the heat links in the simulation.

cooling time. This problem can be improved by adding in the PT cooling station model an additional shield for the heat links site (see Figure 5.28). This shield has to be connected only to one part of the shield to guarantee vibration decoupling. In the region where the additional shield can't be connected to the radiative shield, some scattered light can enter and it will heat up the links. This effect would, anyway, be lower than direct radiation onto the heat links.

This shield can also be used as a support for the multi-layer insulation system. The simulations with Mylar considered a value for the emissivity of $\epsilon = 0.0043$ for the exterior surfaces of the shield's heat links too, so the Mylar was considered also above those. This additional shield can be useful to sustain the insulator and to
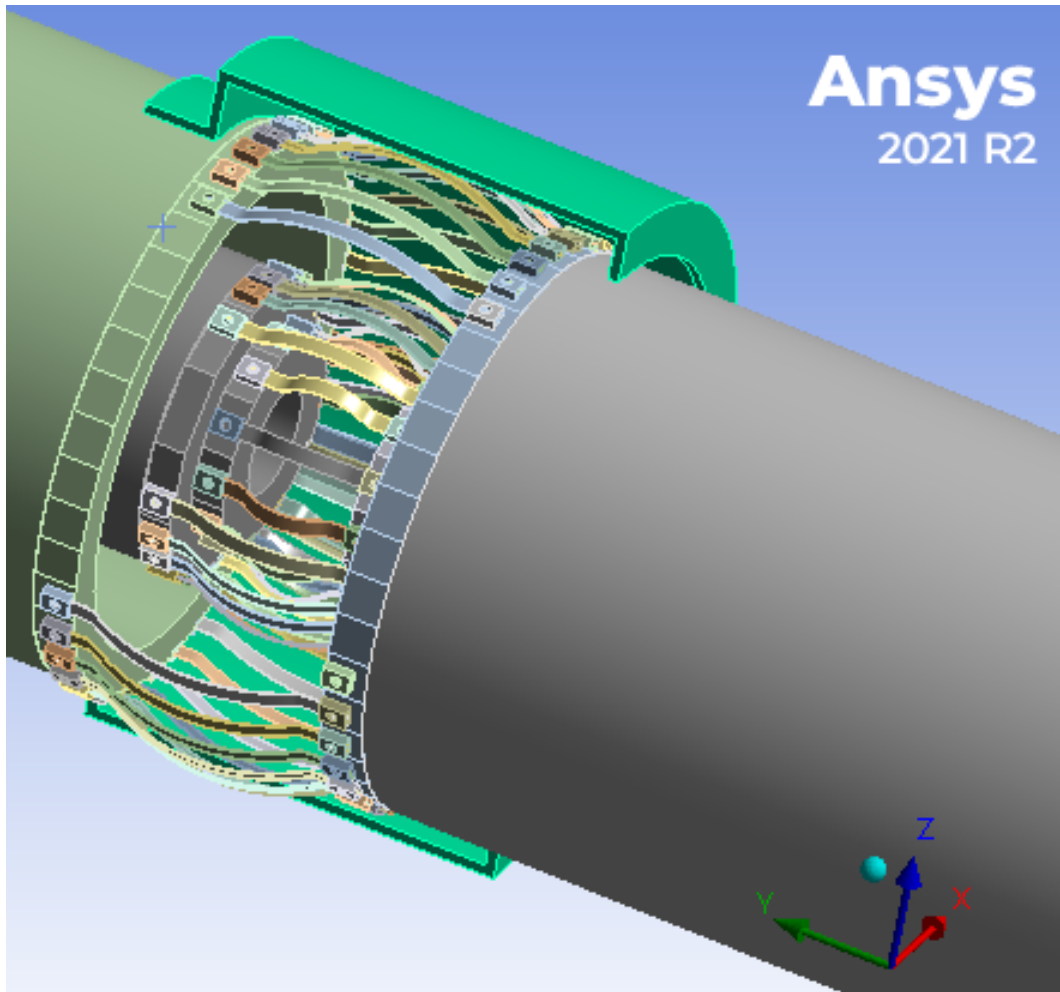
Figure 5.28. Additional shield simplified model. The Figure shows a section of this shield.

mechanically decouple all the different parts.

We can now perform a simulation with this shield using the same conditions considered in the previous two simulations (upper limit curve for conductivity and emissivity of $\epsilon = 0.25$ for all the surfaces) to obtain a rigorous comparison with the others. The enclosures in this case become:

1. Enclosure number 1: the shield part of this enclosure will consider the exterior part of the additional shield and the remaining parts of the bar. The ambient temperature is $300K$.

2. Enclosure number 2: in this case, enclosure number 2 will consider the external and internal surfaces of the shield's heat links and the internal surface of the additional shield. Its ambient temperature is $40K$.

Figure 5.29 shows the temperature gradient over all the heat links in this new configuration. The absolute temperature and the gradient on the shield's heat links follow those of the two enclosures case: this is because the shield will assume an
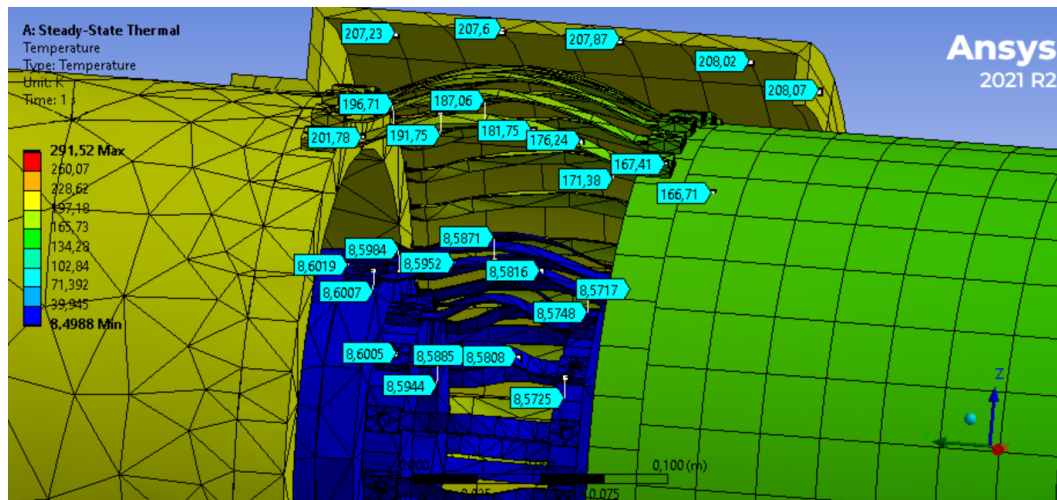
Figure 5.29. Temperature gradient over all the heat links when the additive shield is considered in the simulation.

equilibrium temperature following that of the bar in which it is connected. The temperature on the inner heat links, instead, is a bit higher than the case with two enclosures because, in this case, they will receive also the radiation coming from the interior surface of the additional shield. That radiation is analogous to the missing radiation from the $300K$ vacuum chamber that we haven't considered in the other case. This is then a more realistic configuration even though the temperature is a bit higher. Making a comparison with the one enclosure case, we can see that the additional shield will however reduce the radiation (from $300K$ to $200K$) and so the temperature on the inner heat links is lower.

5.2.8 Steady-state results

We can briefly resume some of the most remarkable results of the steady-state simulations. We can divide the results following the conductivity curve used.

Table 5.10 shows some results of the simulations performed with the upper limit curve for the conductivity while Table 5.11 the results with the lower limit one. The configurations chosen reflect the parameters we expect for the real application. As already mentioned, the typical emissivity value for aluminum is $\epsilon \sim 0.15$ whilst the value of $\epsilon = 0.25$ was used for the worst-case scenario. Hence, the Tables report the steady-state temperature of the PTs' first and second stage bases and the temperature of the furthermost wall of the experimental chamber and its shield for the model with $\epsilon = 0.15$.

The first row of the Tables shows the result of the simulations performed without the super-insulation system: we can see, indeed, the high temperature gradient along the radiation shield caused by the $300K$ vacuum chamber's radiation. A temperature variation of $\Delta T \sim 100K$ is unacceptable for the real application. However, even if its temperature is too high, the shield's aim is respected. The temperature variation in the inner bar is way lower than that in the shield and the temperature reached in

Configuration	$T_{in}^{first\ stage}$ [K]	$T_{in}^{second\ stage}$ [K]	T_{end}^{shield} [K]	T_{end}^{bar} [K]
w/o Mylar $\epsilon = 0.15$ 72-42-40-24-12	64	3.7	169.51	3.7173
w/o Mylar $\epsilon = 0.15$ 72-42-40-0-4	64	3.7	169.61	3.7297
w/o Mylar $\epsilon = 0.15$ 72-4-40-24-12	64	3.5	169.53	3.5266
with Mylar $\epsilon = 0.15$ 72-42-40-24-12	35	2.8	40.853	2.8051
with Mylar $\epsilon = 0.25$ 72-42-40-24-12	35	2.9	38.360	2.9055

Table 5.10. PTs bases and furthermost wall of experimental chamber temperatures obtained from various simulations where the numbers of heat links and emissivity are modified. The heat links' numbers are reported in the first column of the Table and they are in sequence: first stage - second stage - shield - external surface of the bar - inner support on the bar. Table refers to simulations performed with the upper limit curve for conductivity.

the PTs' bases is preserved till the experimental chamber.

The second and third rows of the Tables show the results of the simulations performed with a variable number of heat links. As we can expect, a reduction in the number of heat links makes the heat transfer harder causing an increase in the temperature of both the shield and bar.

The fourth row of the Tables reports the results of the Mylar simulations. In these types of simulations, the emissivity of the external surface of the shield is modified to a value of $\epsilon_{eff} = 0.0043$ and we can already see the effect of the super-insulation in the PTs' bases' temperature. In both the conductivity cases, the temperature of the first stage's bases is way lower than in the case without the Mylar. The entire temperature gradient, furthermore, is way lower with respect to the previous simulations. The experimental chamber's shield's temperature, indeed, is of the order of the real application expectation ($\sim 40K$). The inner bar, too, has a temperature gradient lower than the case without the super-insulation.

The last row in the Tables shows the results of the simulations with Mylar but with an emissivity for the remaining surfaces of $\epsilon = 0.25$: hence, it represents the worst-case scenario with the Mylar. We can see, however, that the presence of Mylar is fundamental: even if we consider the worst scenario for the emissivity, we can obtain an equilibrium temperature for the shield that is almost the same as the $\epsilon = 0.15$ case. On the contrary, the temperature gradient is even smaller because we have to consider higher radiation that can leave the shield towards the bar; its equilibrium temperature, indeed, is a bit higher than the $\epsilon = 0.15$ case.

Configuration	$T_{in}^{first\ stage}$ [K]	$T_{in}^{second\ stage}$ [K]	T_{end}^{shield} [K]	T_{end}^{bar} [K]
w/o Mylar $\epsilon = 0.15$ 72-42-40-24-12	58	3.3	161.37	3.4838
w/o Mylar $\epsilon = 0.15$ 72-42-40-0-4	58	3.3	161.41	3.7830
w/o Mylar $\epsilon = 0.15$ 72-4-40-24-12	58	3.1	161.16	3.5223
with Mylar $\epsilon = 0.15$ 72-42-40-24-12	32	2.6	37.844	2.6601
with Mylar $\epsilon = 0.25$ 72-42-40-24-12	32	2.7	35.390	2.7674

Table 5.11. PTs bases and furthermost wall of experimental chamber temperatures obtained from various simulations where the numbers of heat links and emissivity are modified. The heat links' numbers are reported in the first column of the Table and they are in sequence: first stage - second stage - shield - external surface of the bar - inner support on the bar. Table refers to simulations performed with the lower limit curve for conductivity.

5.3   Transient simulations

We can now focus on the description of the transient simulations. As already explained, transient simulations can be useful to understand the effective cooling efficiency of the PT cooling station with respect to time. Steady-state simulations help us understand the physical limits of a particular configuration (geometry, choice of materials, emissivity, etc) but the results obtained are at the equilibrium: it can be reached ideally in an infinite time. Transient simulations are then indispensable for a real application because we want to know, in a finite and reasonable time, the temperature that will reach the whole facility. Following the same condition presented in Section 5.1, transient simulations will use further information for the materials, i.e. specific heat and density, to compute the cooling time following Equations reported in Section 4.2. In these particular types of simulations, since non-constant heat load can be exploited, refrigeration heat transfer rate can be imposed on the bases as an initial condition. Some problems can however be found. The calculation of the cooling time has to start from the room temperature to the hypothetical equilibrium temperature found for the different configurations in the previous Section. The trend of the PTs' refrigeration power (see the capacity curve in Figure 4.6) focuses on the typical working temperature of both the first and the second stages. The temperature range of the second stage is, indeed, $\sim 2K - 10K$ which is the range of temperature expected for the inner bar while the $40K$ temperature expected for the shield is within the range of the first stage

reported ($\sim 30K - 80K$). The computation of the whole cooling time needs also informations about the refrigeration power when both the stages are at $300K$. We can overcome this problem following a simple solution used by M. A. Green et al.[12]. Usually, each model of PT has a certified performance that is guaranteed by the producer. Since the authors didn't have the capacity curve for the full range ($300K$ till cryogenic temperature) for their PT's model, i.e. PT415 with remote motor, they obtained a predictive trend by rescaling the full range capacity curve for PT410 on the bases of the proportion of their respective certified performance. We can do the same to obtain a predictive trend for the capacity curve of PT420.

The certified performance for PT410 is $1.0W$ at $4.2K$ on the second stage with $28 - 30W$ at $40K$ on the first. The full range capacity curve is reported in Figure 5.30.
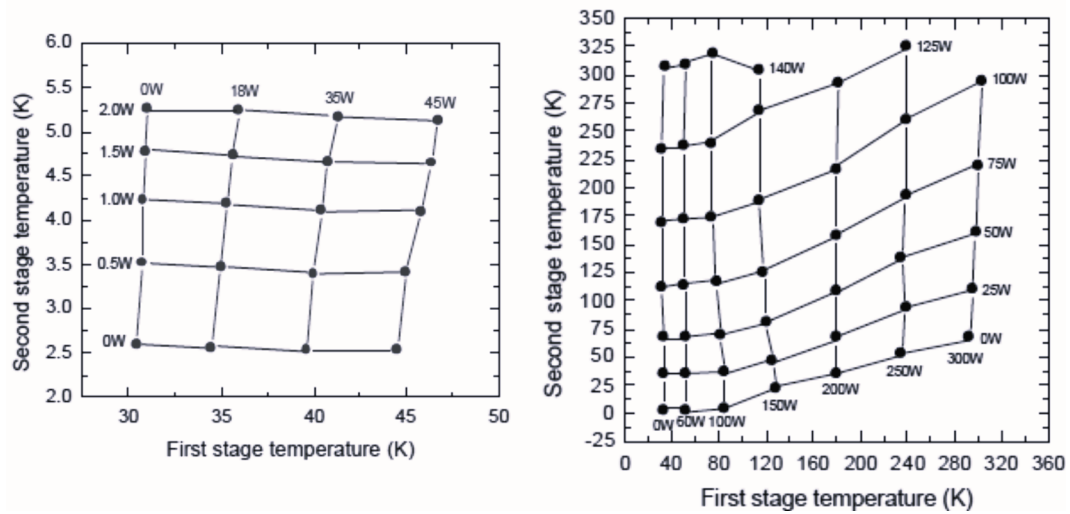
Figure 5.30. Capacity curve for the typical working range (on the left) and for the full range, room to cryogenic temperature (on the right).

The certified performance for our PT420 with remote motor is $1.8W$ at $4.2K$ on the second stage with $50W$ at $45K$ on the first. To obtain the trend we can then multiply the second stage refrigeration power of the PT410 by 1.8 while, for the first stage refrigeration power, we can multiply by 1.5. The full range capacity curve obtained is reported in Figure 5.31.

Comparing this predictive trend with the capacity curve reported in Figure 4.6, we can see that, at least for the first stage's refrigeration power, this trend is different from the provided one for the $90W$ curve. We will however perform transient simulations with this capacity curve even though we cannot expect the hypothetical infinite time solution to converge to the steady-state equilibrium solutions found in the previous Section.

5.3.1   Transient cycle

We can start the description of the transient simulations by explaining how a transient simulation can be settled up. Let's consider the model with the upper limit
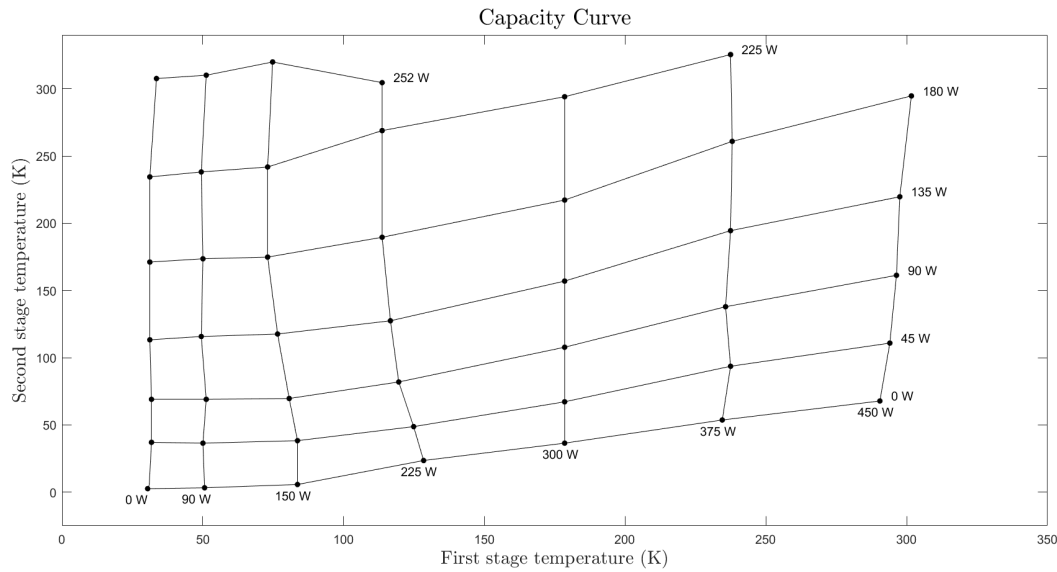
Figure 5.31. Predictive trend for the capacity curve for the full range, from room to cryogenic temperature, of PT420 with remote motor.

curve for the conductivity, emissivity value for all the surfaces of $\epsilon = 0.25$ and the maximum number of heat links (reported in Table 5.4).

As already mentioned, we can impose the refrigeration power condition directly on the PTs bases following the predictive capacity curve in Figure 5.31. Since we have to start with a room temperature model, we have to obtain the refrigeration power value for the temperature of $300K$ for both the first and second stages. The interpolated values are $P_{first} = -440W$ and $P_{second} = -185W$. Before the start of the simulation, we have to impose the real-time through which the simulation must be performed; so, we have to impose a priori the validity time for the refrigeration power settled. Since the refrigeration power is a function of PTs' bases temperature, we can perform the simulation for a generic long time and then take the time the PTs' bases take to reach a chosen ending temperature for the validity of the refrigeration power. This time value represents the first time step of our simulation, characterized by its refrigeration power conditions. ANSYS gives us the possibility to impose a heat load condition, i.e. our refrigeration power, which varies with time: we can then start a new simulation which will consider, for the first time step, the initial refrigeration conditions and for the second, the new interpolated refrigeration values based on the first step's ending temperatures of the PTs' bases.

In this way, choosing an ending temperature for the validity range which is $\sim 10-15K$ below the initial temperature, we can build our simulation from a temperature value of $300K$ for both the first and second stages to a temperature that approaches the equilibrium temperatures found in the steady-state simulations.

Figure 5.32 shows the results of the simulation described. Blue curves represent the first stage temperature while red curves the second stage's one. Solid lines show the temperature for the PTs' bases while dashed lines show the temperature computed on the furthermost wall of the experimental chamber with respect to the

PTs' location. As we can expect, the temperature of the PTs' bases decreases very fast in the first seconds of the simulation (they reach a temperature of $\sim 200K$ in the first $2500s$). This is caused by the first bottleneck of the model which is characterized by the PTs' heat links in both the first and second stages. Although we are considering 72 heat links in the first stage and 42 for the second stage, the equivalent resistance is still high; the bases can then reach a low-temperature value while the heat transfer rate of the remaining geometry has difficulties in reaching the bases.

Cooling with $\epsilon = 0,25$, upper limit curve, maximum heat links
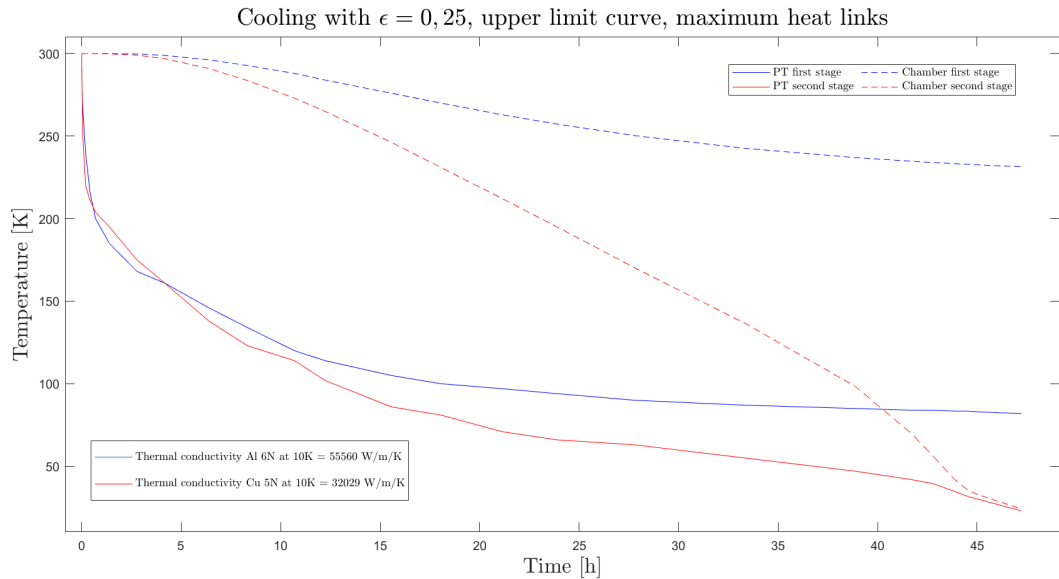
Figure 5.32. Cooling simulation for the model with $\epsilon = 0.25$, upper limit curve for conductivity and the maximum number of heat links. Blue curves represent the first stage temperatures while red curves the second stage's one. Solid lines show the temperature of the PTs' bases while dashed lines the temperature of the furthermost wall of the experimental chamber.

When the temperature variation of the PTs' bases starts to decrease, the first bottleneck has been surpassed and the first half of the bar (and shield) starts to cool down. In this situation, the second bottleneck starts to become relevant. The equivalent resistance of the shield's heat links or bar's heat links is higher than the bulk material's resistance which characterizes the bar or the shield. Hence the heat transmission will be obstructed. The experimental chamber's wall starts to cool down after $\sim 4h$, when the PTs' bases' temperature is $\sim 160K$: a massive temperature gradient will then be present.

We can see from the solid curves that the PTs' bases cool down following the same trend: until $\sim 130K$, the first and second stage bases have almost the same temperature. When the radiation starts to become relevant, the first stage starts to cool less because the radiative heat transfer rate rises every time step (it comes, indeed, from the outer vacuum shield which is at $300K$). The relevance of the radiation can be seen also in the dashed curves, i.e. the experimental chamber temperature; the blue line, indeed, represents the first stage's experimental chamber

temperature which reaches a temperature of $\sim 230K$ for the entire duration of the simulation. Otherwise, the speed of cooling of the second stage experimental chamber is higher than the first stage's. The red dashed line, indeed, has a higher slope than the blue's and it approaches the PTs second stage's base temperature at the end.

These results follow the expectations given by the steady-state simulation of the same model (see Figure 5.11). Focusing on the first stage, we can see that the expected temperature for the PTs bases is $80K$ while for the experimental chamber is $216K$. The values obtained for the transient simulation (after approximately two days) are $82K$ for the PTs' bases and $230K$ for the chamber. In the case of the second stage, instead, the expected values are $8.50K$ and $8.64K$ respectively for the bases and chamber (hence a small gradient is expected); the simulation has been stopped at a temperature of $23K$ for the PTs' bases and $24.3K$ for the experimental chamber. The slopes of the two red curves, anyway, suggest that a lower temperature could be reached; contrariwise from the blue lines, whose derivative at the ending time approaches zero, the red lines' slope is still high. The simulation had to be stopped because every new additional time step makes the computation time higher and, since the temperatures approach the higher slope regions for both conductivity and specific heat, the time step needs to be smaller each time. We can however conclude that, to reach the temperature of $\sim 8.5K$, we need an additional time that is low with respect to the time already spent. Hence the predictive needed time for the model is ~ 2 days.

Analytical comparison

Before the description of a more realistic model, i.e. considering an emissivity of $\epsilon = 0.15$, Mylar for the shield and the additive shield, we can try to compare the obtained cooling time with an analytical estimation.

The complete analytical calculation of the cooling time requires resolving the three-dimensional PDE described in Section 4.2 considering the radiation and the refrigeration power as boundary conditions. We can, however, compare the required cooling time obtained in each time step of our simulation with an analytical estimation. Since, in every time step, we have the information about the refrigeration power used (for both the first and second stages) and the initial and ending temperature, we can compute the total heat extracted. Following Equation 4.16, the total heat extracted will be proportional to the temperature difference and to the specific heat which is a function of temperature: this last quantity will be, then, computed considering an average temperature between starting and ending temperature of each time step. The temperature variation, instead, can be computed both considering the variation on the PTs' bases or in the experimental chamber temperature: an average temperature in this situation is harder to obtain because of the two bottlenecks of the model. Two different times can then be calculated, one considering the ΔT on the PTs' bases and another on the experimental chamber. The two quantities can be computed as:

$$ t_{PT} = \frac{\rho V c_P(\bar{T}) \Delta T_{PT}}{P_{refr}} \qquad\qquad t_{chamb} = \frac{\rho V c_P(\bar{T}) \Delta T_{chamb}}{P_{refr}}. \qquad (5.11) $$

We can compute these times for every step and compare them with the simulated time.

Figure 5.33. Comparison between analytical times computed for each step with the simulated time for both the first and second stages.

Figure 5.33 shows both the first (left) and second stage (right) comparison between the two times computed and the simulated time for every step of the simulation. Red lines represent the estimated time considering the temperature variation on the PTs' bases; since we are considering that the ΔT describes the entire model, the estimated time is expected to be way larger than the simulated time: this trend can be seen in both stages. The simulated time in those steps, indeed, refers to the time needed to cool down only the PTs' bases before the first bottleneck of the model. From the point when the blue lines cross the red curves, we can obtain

approximatively the step in which the bottlenecks are efficiently surpassed. From that step on, the experimental chamber starts to cool down faster than the PTs' bases. Comparing the times with the cooling curve in Figure 5.32, we can see that the first stage cooling for both the bases and chamber has an analogous slope: this can be seen also in the analytical time estimation, red and blue lines on the left of the Figure 5.33 are almost the same curve but shifted by some time steps that represent the delay caused by the bottlenecks. A different trend can be seen, instead, on the right side of Figure 5.33, the blue curve has a maximum higher than the red line's after the crossing: this can be explained by the cooling acceleration of the experimental chamber that can be seen from the red dashed line in Figure 5.32.

The analytical comparison must be done between the black curves, i.e. the simulated time, and the red/blue curves. We can see that, for the first steps, the simulated time is within the range of the two analytical times but, firstly on the first stage trend and then on the second, the simulated time starts to exceed the analytical solutions. This is mainly due to the radiation: in the analytical calculation, the radiative heat transfer rate isn't considered. Its contribution is negligible in the first time steps, i.e. when the temperature of the model is almost the same as the vacuum shield, but when the temperature starts to drop, the radiative heat transfer rate will reduce the cooling efficiency. Hence, the simulation time is expected to rise. This effect, furthermore, must be seen mostly in the first stage time, that is the stage with the $300K$ incident radiation.

We can try to estimate the radiative contribution to the total time of cooling. Considering the Boltzmann's equation 4.11 without taking into account the view factors, we can modify the two cooling times in:

$$t_{PT} = \frac{\rho V c_P(\bar{T}) \Delta T_{PT}}{P_{refr} + P_{rad}} \qquad\qquad t_{chamb} = \frac{\rho V c_P(\bar{T}) \Delta T_{chamb}}{P_{refr} + P_{rad}}. \qquad (5.12)$$

The resulting comparisons between the analytical times and simulated time are reported in Figure 5.34.

In this case, some negative times can be seen both in the first and second stage's analytical times. These are due to an overestimation of the radiative contribution due to a non-averaged temperature and to view factors. The first stage analytical times, however, approaches the simulated time with the radiative contribution. This validates, at least for the first stage, the simulation. In the last steps of the simulation, both the first and second stages' times approach each other: this shows us that the simulation reaches an equilibrium between the heat extracted and the radiative contribution.

5.3.2 Simulation with maximum heat links

We can now describe the results of the simulation performed with the maximum number of heat links (see Table 5.4). The model used is with the upper limit curve for conductivity, emissivity $\epsilon = 0.15$, Mylar on the outer surface of the shield ($\epsilon_{eff} = 0.0043$) and with the additional shield for the $300K$ radiation on the heat links.
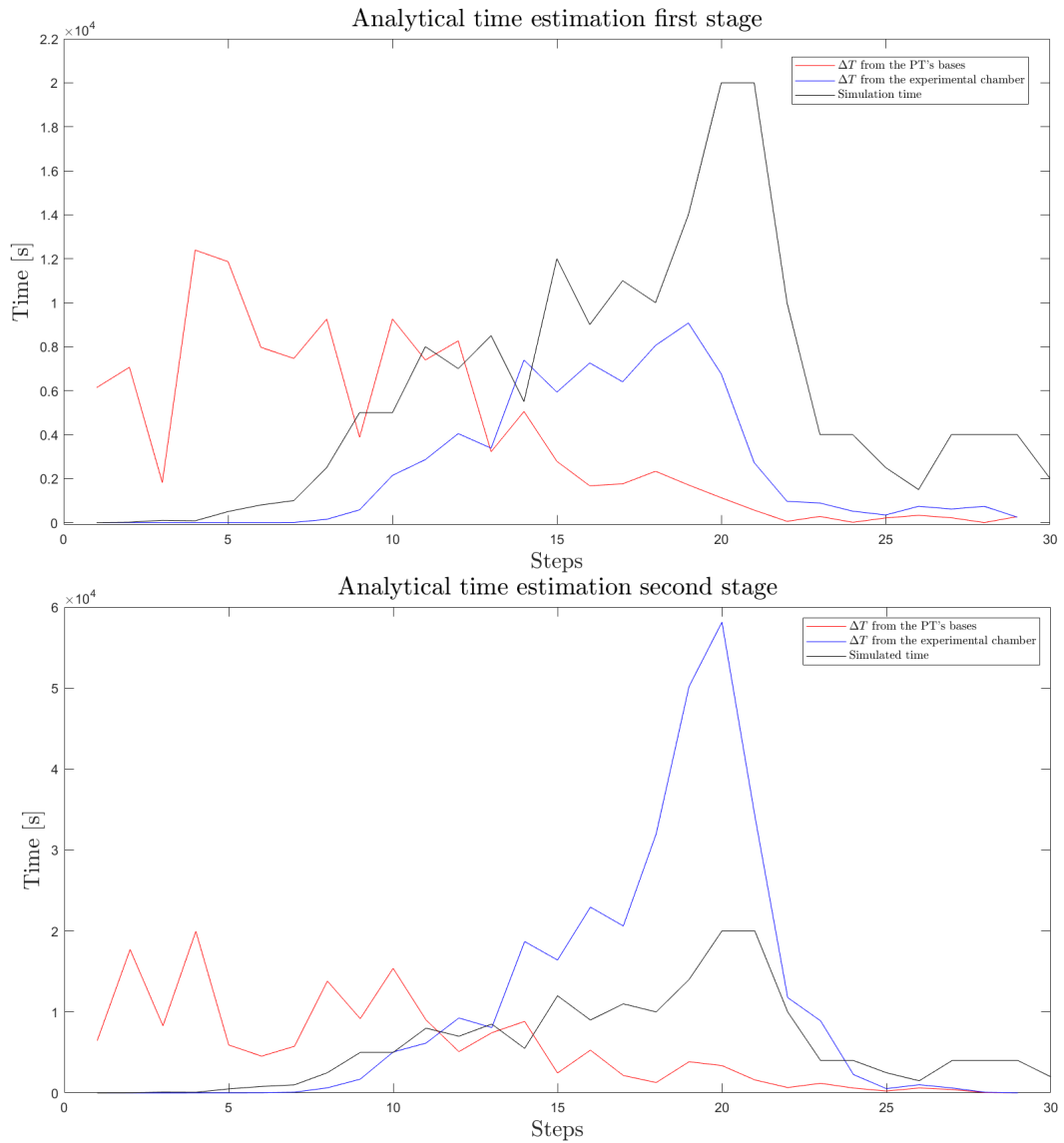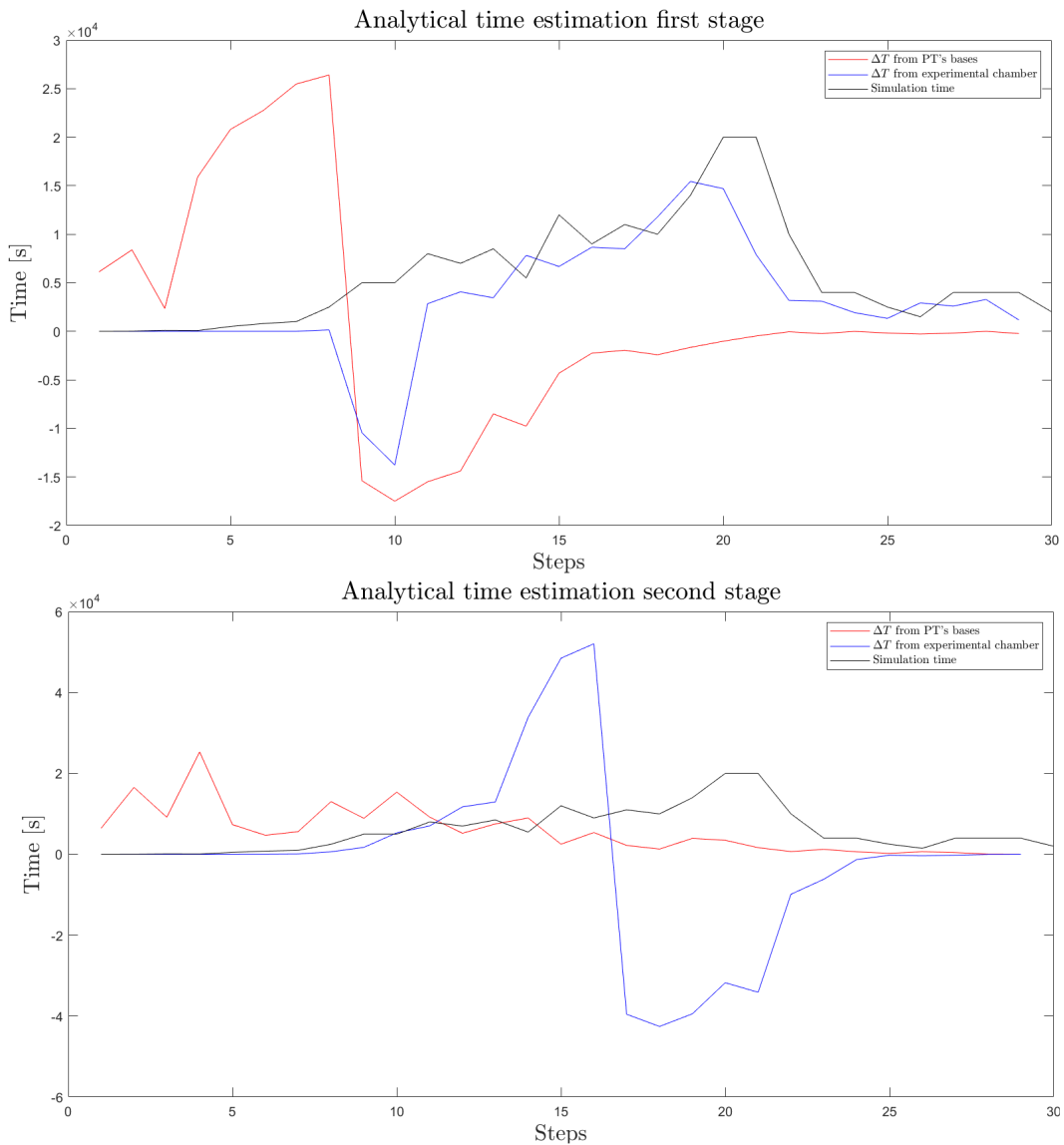
Figure 5.34. Comparison between analytical times computed for each step with the simulated time for both the first and second stages. Radiation contribution is considered.

Figure 5.35 reports the temperature trends for the PTs' bases and experimental chamber of both the first and second stages.

We can start the description with the PTs' bases' temperature. Both the first and second stages (solid lines in the Figure) have the same cooling trend: the first stage, however, is always colder than the second stage. This is what we expected because the first stage, i.e. the shield, is useful to block the direct radiation coming from the vacuum shield; hence, thanks to its cooling, the inner bar can lower its temperature. We can see also in this situation the relevance of the two bottlenecks of the model: the experimental chamber, so the entire facility, starts to cool down after $\sim 5.5h$ which is $\sim 1/5$ of the whole simulation time. This long delay, as

Cooling with $\epsilon = 0,15$, MYLAR, upper limit curve, maximum heat links
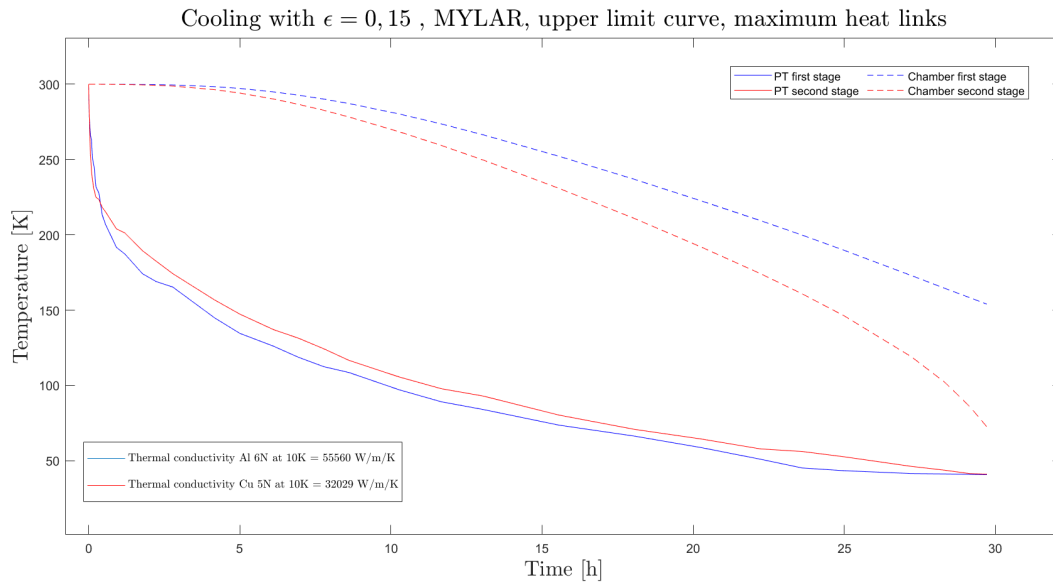
Figure 5.35. Cooling simulation for the model with $\epsilon = 0.15$, Mylar on the shield, upper limit curve for conductivity and the maximum number of heat links. The blue curves represent the first stage temperatures while the red curves the second stage's one. Solid lines show the temperature of the PTs' bases while dashed lines the temperature of the furthermost wall of the experimental chamber.

already mentioned in the $\epsilon = 0.25$ simulation, is due to the two heat links site whose equivalent resistance is high. The presence of the Mylar, however, helps the cooling of the first stage which approaches the temperature of $154K$ before the end of the simulation. The second stage's chamber follows the shield slope in the first seconds and then starts to accelerate the cooling trying to approach the second stage's bases' temperature.

The values of this simulation have to be compared with the steady-state simulation in Figure 5.21. Thanks to the Mylar, the equilibrium temperature of the shield is $35K$ on the PTs' bases and $\sim 41K$ on the experimental chamber. The transient temperature on the first stage bases is $40.7K$ at the end of the simulation; this value can be considered an equilibrium value because the slope of the cooling curve approaches zero: the temperature is in good agreement with the steady-state temperature. On the first stage's experimental chamber side, instead, the temperature is way higher than the expected equilibrium temperature: the slope of the blue dashed curve in Figure 5.35 suggests that the cooling is far from the end. The same trend can be seen in both the red curves. The equilibrium temperature of the second stage is $\sim 2.8K$ with a small gradient; both the red curves are away from the equilibrium temperature but the slopes are still high.

The complete transient simulation, then, requires a longer simulation time but, as already mentioned, the next time steps of the simulation must be shorter to better follow the high slopes in the conductivity and specific heat. However, with this simple transient simulation, we can understand again the relevance of the Mylar. With respect to the $\epsilon = 0.25$ simulation presented above, we can see that the experimental

chambers of both the first and second stages cool in less time: this is caused by the minor relevance of the radiative contribution. Considering, as in the $\epsilon = 0.25$ case, that the remaining time for the equilibrium is lower than the time spent, we can obtain a predictive total time for the cooling of ~ 1.5 days.

5.3.3   Variation of the model

We can present two other transient simulations performed with some variations with respect to the simulation presented above. The model will still have the additional shield for the radiation, upper limit curve for conductivity, Mylar on the shield and $\epsilon = 0.15$, but the differences will be:

1. Model 1: 8 heat links on the inner bar. From the maximum number of $24 + 12$ (on the external surface of the bar and on its inner support), the heat links on the bar are reduced to $4 + 4$;

2. Model 2: 200 heat links on the shield. From the maximum number of 40, the heat links on the shield are increased to 200. This number requires also a modification in the geometry of the whole shield because that large number of heat links cannot be inserted in the geometry, but it won't be considered.

Model 1

We can present the cooling curve of the new model compared with the main model, i.e. the model described in Section 5.3.2.

We can see in Figure 5.36 the comparison between the main model and the new configuration. As we expected, the PTs' bases' temperatures in the new configuration follow the main model's ones. Especially in the first stage temperature curve, we can see that also the ending temperature is the same as the main model. The ending temperature of the second stage's bases, instead, is a little lower because of the reduction of the inner heat links: as already discussed for the steady-state simulations, a lower number of heat links makes the heat flow harder; hence the second stage bases can reduce further their temperature.

The major differences can be seen in the second stage experimental chamber's temperature. While the first stage chamber's temperature follows the main model, the second stage's is delayed by $\sim 5.5h$: this is what we expect with a reduction of the heat links. We can see that the simulation has been stopped when the second stage experimental chamber's temperature is almost equal to the main model ending temperature: this stress the fact that, when the temperature approaches the one of the high slopes in the conductivity and specific heat, the simulation requires smaller time steps.

Following the same consideration used in the previous descriptions, we can obtain the cooling time for this model which is $\sim 1.75 days$.

Model 2

In the same way as the previous simulation, we can present the comparison between the main model and the "Model 2" configuration. Increasing the number of

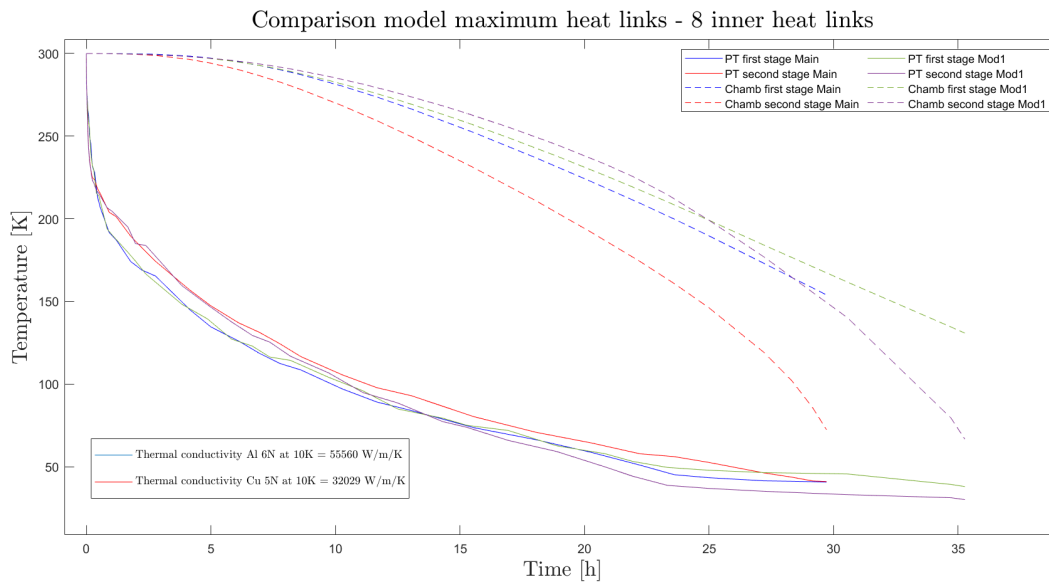Comparison model maximum heat links - 8 inner heat links

Figure 5.36. Cooling simulation for the model with $\epsilon = 0.15$, Mylar on the shield, upper limit curve for conductivity and 8 heat links in the inner bar. Blue curves represent the first stage temperatures while red curves are the second stage's ones for the main model. Green curves represent the first stage temperatures while purple curves are the second stage's ones for Model 1 configuration. Solid lines show the temperature of the PTs' bases while dashed lines the temperature of the furthermost wall of the experimental chamber.

shield's heat links, we want to show that, if the first stage reaches a lower temperature in a minor time, the second stage too will cool down faster.

Figure 5.37 shows exactly what we expect. The green dashed line represents the first stage experimental chamber's temperature; it is always below the blue dashed line, i.e. the main model analogous, hence, the first stage will cool down faster in the "Model 2" configuration. We can see the effects of this in the second stage considering the purple dashed line. Till the temperature of the first and second stage's experimental chamber remain close, the faster cooling of the first stage doesn't affect the cooling of the second stage. After $\sim 25h$, when the cooling of the second stage starts to accelerate, the first stage has a temperature of $\sim 30K$ lower than the main model: this allows the second stage's cooling to accelerate even more than the other configuration. The estimated cooling time is 1.3 days, a bit lower than the main model.

Further modification

Other transient simulations should be performed to better understand all the possibilities in the cooling of the facility. Following the same scheme of "Model 1" and "2", other variations in the number of heat links could be considered. For the shield's heat links, we can imagine performing simulations varying also the number of the PTs' heat links: what we can expect is almost the complete removal of all the

Comparison model maximum heat links - 200 shield's heat links
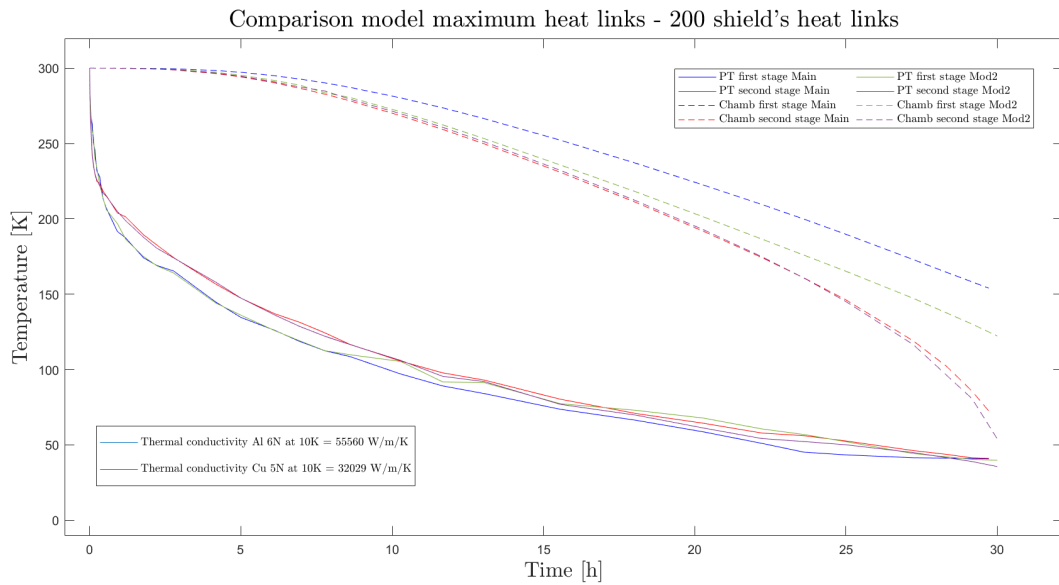
Figure 5.37. Cooling simulation for the model with $\epsilon = 0.15$, Mylar on the shield, upper limit curve for conductivity and 200 heat links in the shield. Blue curves represent the first stage temperatures while red curves are the second stage's ones for the main model. Green curves represent the first stage temperatures while purple curves are the second stage's ones for Model 2 configuration. Solid lines show the temperature of the PTs' bases while dashed lines the temperature of the furthermost wall of the experimental chamber.

bottlenecks on the shield, so it should cool down even faster than the "Model 2" case. In the inner heat links modification, instead, we can try different combinations, of both bar's heat links and the second stage's PTs' heat links, to better understand the physical limits of the cooling time with any vibrational constraints.

All of these simulations can also be performed by exploiting the lower limit curve for conductivity: in that case, we can consider the whole possible range of time's value for the cooling.

5.3.4 Transient results

We can resume the cooling time estimated in the simulations in Table 5.12.

Configuration	Cooling time [days]
$\epsilon = 0.25$, all links	2
$\epsilon = 0.15$, Mylar, all links	1.5
$\epsilon = 0.15$, Mylar, 8 inner links	1.75
$\epsilon = 0.15$, Mylar, 200 shield's links	1.3

Table 5.12. Cooling time in the various simulations performed. All the simulations are performed using the upper limit curve for conductivity.

The results remark the fact that the presence of Mylar is fundamental: in addition

to the possibility to reach a lower temperature in the shield, which allows a reduction in the temperature gradient of the bar, the Mylar is useful to reduce the cooling time of the whole facility.

As expected, a lower number of heat links in the inner bar increases the cooling time; we can see, indeed, that when only 8 inner heat links are considered, the cooling time increase by more than 15% with respect to the case where all the heat links are used.

The simulation performed with 200 heat links, instead, shows that the efficiency of the heat transfer in the shield must be enhanced to allow the shield to reach a lower temperature in less time: this yields the inner bar to follow that trend resulting in more efficient cooling.

Chapter 6

Al 6N conductivity measurement

High purity materials are fundamental for a good heat transfer due to their high conductivity value at cryogenic temperatures. Their relevance can be understood in the previous Section where different steady-state and transient simulations are performed considering various values for the conductivity of high purity aluminum and copper. Those values are taken from A. L. Woodcraft[33] who collected various results from the literature to give us recommended values that span a large range. Since the upper and lower limit curve used for the simulations vary more than one order of magnitude at cryogenic temperature, the simulation results can only be taken as a reference for the best and worse cases. A real case simulation can be performed only when the real parameters can be used for conductivity, emissivity and specific heat. In this Chapter, a measurement of conductivity for a sample of 6N aluminum will be described.

6.1 Thermal conductivity

The heat transfer in a solid is due both to lattice vibrations (phonons) and to conduction electrons[31], [35]. Experiments show that in reasonably pure materials, nearly all the heat is carried by the electrons while in impure materials an appreciable proportion of thermal conductivity is due to lattice conduction. The heat carriers do not move ballistically from the hotter to the colder part of the material. The result is a diffusive process which can be described as a gas diffusing through the material. The thermal conductivity κ can then be described as:

$$\kappa = \frac{1}{3}c_V v \lambda_0 \tag{6.1}$$

where c_V is the specific heat at constant volume, v and λ_0 are, respectively, the velocity and the mean free path of conduction electrons. In the low-temperature regime, both velocities for phonons and electrons are independent of temperature. In the same regime, the mean free path of electrons is constant since it becomes comparable in size with the density of impurities and defects in metal: thus, high purity metals have larger conductivities at low temperatures. In the case of high

purity materials with a small diameter (if wires) or thin foils, the size of the sample can be comparable with the mean free path of an electron and can limit the conductivity. This is known as the size effect.

An analytical estimation of the thermal conductivity can be made considering the Debye temperature θ_D as a temperature limit for phonons contribution. In very low-temperature regions ($T << \theta_D$), the Wiedemann-Franz law holds:

$$\frac{\kappa}{\sigma} = \frac{\pi^2}{3}\left(\frac{k_B}{e}\right)^2 T = L_0 T \tag{6.2}$$

where κ and σ are, respectively, the thermal and electrical conductivities, k_B is the Stefan-Boltzmann constant, e is the elementary charge and $L_0 = 2.443 \times 10^{-8} V^2/K^2$ is the Lorentz factor. Thermal conductivity measurement, generally, requires a long time and specific instrumentation, especially in the low-temperature regime. On the other hand, electrical conductivity measurement is much easier; hence, using the Wiedemann-Franz law, we can use electrical conductivity to obtain thermal conductivity values.

To estimate the thermal conductivity at higher temperature regions, we need to consider electron scattering by phonons. Since the number of phonons increases with temperature, these types of scattering are temperature-dependent. By combining the Wiedemann-Franz trend with that of a higher temperature range, below $\theta_D/10$, which is $\kappa \sim T^{-2}$, we can express the conductivity as:

$$\kappa = \frac{1}{AT^2 + B/T} \tag{6.3}$$

which can be applied below $\theta_D/10$ and approximately below $\sim 30K$ for aluminum. Coefficients A and B depend upon the type of material.

A good parameter to evaluate thermal conductivity is the RRR: it is defined as the ratio between the electrical conductivity at cryogenic temperature (usually $4.2K$) and that at room temperature,

$$RRR = \frac{\sigma_{4.2K}}{\sigma_{300K}} = \frac{\rho_{300K}}{\rho_{4.2K}} \tag{6.4}$$

where ρ is the resistivity ($\rho = \frac{1}{\sigma}$).

The ratio, following the Wiedemann-Franz law, is the same as that between the respective temperature thermal conductivities. Usually, the RRR value can be considered an indicator of the purity of a metal. Since at low temperatures, the electrical conductivity is determined by scattering on defects, the RRR is a measure of the limiting defect scattering, hence of the purity of the material.

Particular attention can be paid to the description of the size effect. As already mentioned, when the diameter of a wire or the thickness of a foil is comparable in size with the mean free path of the conduction electron, the conductivity (if the Wiedemann-Franz law stands, both electrical and thermal) may be reduced[21]. Different studies have been made on this effect: conductivity for thin specimens was calculated by Fuchs[11] and Sondheimer[28] (F-S theory) for films and by Dingle[7] for wires. These calculations are based on the spatial variation of the electron distribution function. Different alterations of their equations can be found: they consider various side effects but in the first order their calculations can be used to

fit experimental data. Since, unlike KAGRA's, ET's heat links are composed of thin foils, we can report the Equation for the modified electrical conductivity due to the size effect for thin films:

$$\frac{\sigma}{\sigma_0} \sim \frac{3}{4}(1 - \epsilon)\frac{d}{\lambda_0} log\left(\frac{\lambda_0}{d}\right) \tag{6.5}$$

where σ is the electrical conductivity for the thin film while σ_0 is the same quantity but for the bulk material. With the same subscript, λ_0 is the mean free path of the bulk material while d is the thickness of the foil. This Equation is obtained considering a general theory, which does not assume that the scattering at the surface of the film is entirely diffuse. This would, indeed, occur only if the surface deviates very much from a plane. The value ϵ refers to the fraction of electrons that are scattered elastically at the surface. The limits of this quantity are $\epsilon = 0$ which is the case where a completely diffuse scattering takes place and $\epsilon = 1$ with completely specular reflection: in this last case, Equation 6.5 can't be considered and $\sigma/\sigma_0 = 1$.

6.2 Experimental setup

The experimental measurement will be a resistivity measurement through which we can obtain thermal conductivity following Equation 6.2. This measurement allows us to obtain the value of RRR for the material as well. This Section will describe the experimental setup with a characterization of the specimen, the technique and the instrumentation used.

6.2.1 Specimen

The aluminum foil has the dimension of $(98.34 \pm 0,01)mm$ in length, $0.5mm$ in width and $100\mu m$ thick. Such dimensions were chosen to have an acceptable value of resistance of the sample. The resistivity we need, in fact, is connected to the resistance we measure through the second Ohm's law:

$$R = \rho\frac{L}{A} \tag{6.6}$$

where L is the length of the specimen while A is the cross-sectional area through which the current will flow. Since the electrical resistivity is expected to diminish at low temperatures (since the thermal conductivity is expected to rise), the cross-sectional area was chosen to obtain a value of resistance high enough to be easily measurable with standard equipment. The dimensions, especially the thickness, can be compared with the mean free path to understand the relevance of the size effect. T. Yamada[35] reports a value for the mean free path of conduction electron for the bulk in aluminum 6N of $\lambda_0 = 0.7mm$. This value is almost an order of magnitude greater than the thickness, so the size effect is expected to be relevant.

6.2.2 Measurement technique

The resistance measurement is performed using the 4-wire (or Kelvin) technique[17]. Usually, the measurement-wires' resistance is very small (order of tens of ohms), so

in typical resistance measurements, it will be negligible. If the sample resistance is, however, very low, even lower than the cable resistance, that contribution would be relevant. We know from Ohm's law 4.3 that resistance is equal to voltage divided by current. The current is the same at all points in the circuit but we want to measure only the voltage dropped across the sample resistance and not the wire's contribution. In addition, our goal is to measure this resistance from a distance; a simple scheme is reported in Figure 6.1.
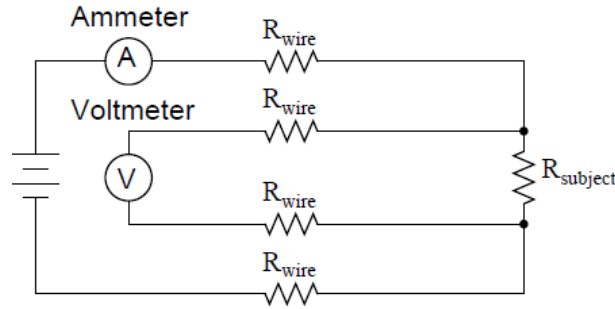
Figure 6.1. 4-wires measurement scheme.

As we can see, the voltmeter has to be connected through two long resistive wires. The voltage drop along them will, however, be negligible, so the voltmeter measurement will be nearly the same as if it were connected directly across the sample resistance.

The measurements are performed with Keithley Model 2182 Nanovoltmeter[15] and Model 6221 AC and DC Current Source[16] linked with Delta-Mode. Delta voltage measurement uses a current-reversal technique to cancel the effects of thermal ElectroMotive Force (EMF). When dissimilar metals, that make up terminals and contacts, touch each other and create a temperature difference, they generate a EMF: this phenomenon is called Seebeck effect. It could create undesirable noise during small voltage measurements because its typical order of magnitude is μV per K of temperature difference. Each Delta reading is calculated from two voltage measurements: one on the positive phase of an alternating current source (V_1) and one on the negative phase (V_2). Each measurement includes the thermal EMF. Considering a test circuit that has $+10\mu V$ of EMF, for a positive test current, the measurement will be $|V_1| + 10\mu V$ whilst for the negative one, $-|V_2| + 10\mu V$. The two values are then averaged:

$$Delta = \frac{|V_1| + 10\mu V + |V_2| - 10\mu V}{2} = \frac{|V_1| + |V_2|}{2}. \tag{6.7}$$

The Delta value obtained is then without the contribution of the EMF.

6.2.3   Experimental instruments

Measurement base
A measurement base has been designed to electrically connect the foil to the 4-wires used for the measurement. The base is a Printed Circuit Board (PCB) where four connectors are welded: two of them will be used to carry the current while the other two to make the voltage measurement. Figure 6.2 shows the PCB; on the upper surface, the copper conductive foil is removed from the middle part. The electrical connection between the two ends will be guaranteed only by the Al 6N foil.
Two aluminum clamping elements are situated on both the ends of the PCB: they are designed to clamp the foil and to assure the mechanical and electrical connection to the base.
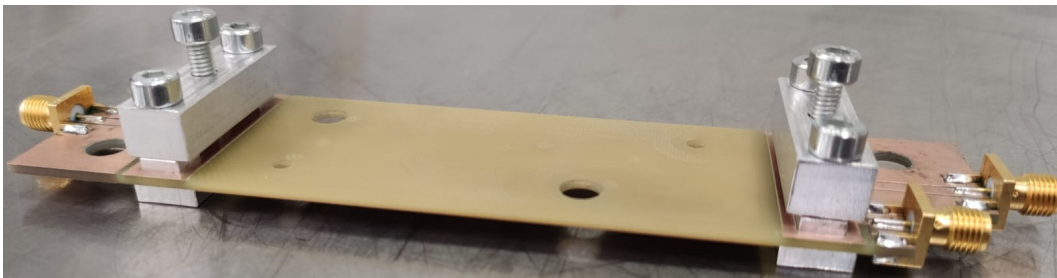
Figure 6.2. Experimental base used to hold the specimen. At the two ends, two screw clamping elements can be used to fix the film during the measurement.

The two end screws for each clamping element will attach the two clamping parts while the middle screw will be used to fix the aluminum foil to the base. Figure 6.3 shows a detail of the upper element of the clamping mechanism.

Figure 6.3. Details of the clamping mechanism.

The upper surface of the element in the Figure is the base-side surface: the screw will be inserted from the surface below and it will push the little cube that will be inserted into the square hole in the element. The project of the clamping mechanism was designed to have only one point (for each side) assigned to fix the foil at the base: in this way, the electrical contact between the foil and the PCB would be the smoother possible. A torque screwdriver is used to screw the middle screw of the clamping mechanism: the torque applied is $1Nm$.

Cryostat

The cryostat used for the measurement is reported in Figure 6.4.
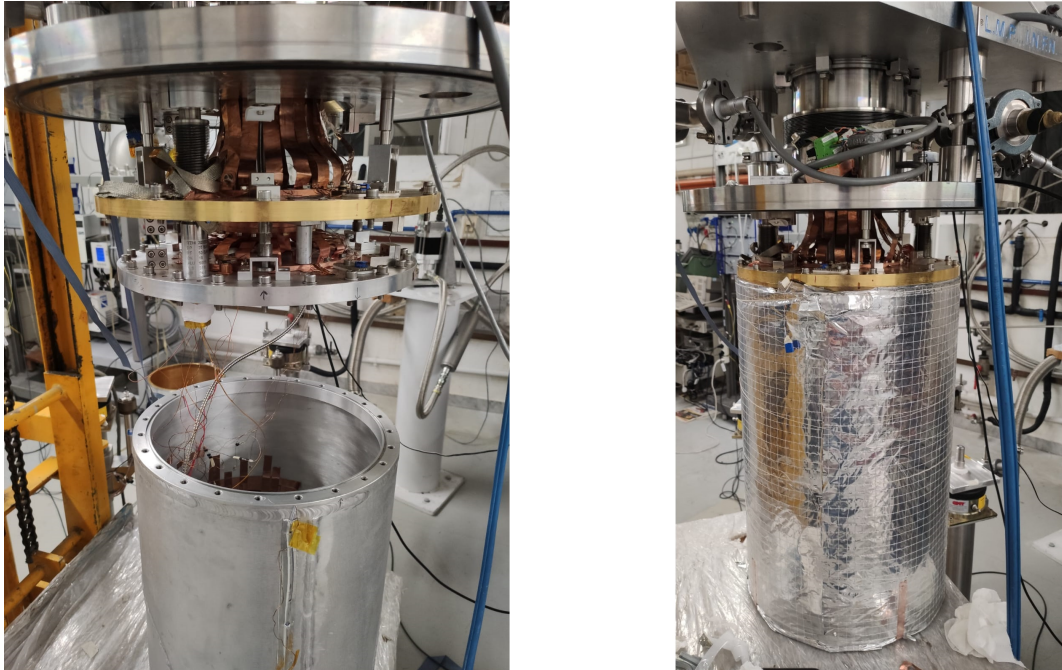
Figure 6.4. Cryostat used for the cryogenic measurement. The figure shows, on the left, the inner part of the cryostat while on the right the radiation shield.

The left side part of the Figure shows the inner chamber (that will reach a temperature of $\sim 15 - 20K$) with the bottom part of the PT used to supply the refrigeration power. On the right side part, instead, is shown the radiation shield attached to the first stage of the PT.

Thermometers

Since the measurement will be temperature-dependent, various thermometers are disposed around the cryostat. First of all, two diode thermometers are used to measure the temperature on the PT bases. Two Cernox^{TM}, i.e. resistance thermometers, are located on the measurement base to quantify the temperature of the foil during the measurement. One last diode thermometer is installed on the internal surface of the inner chamber's cover. It is useful to control possible gradients in the cryostat chamber between the upper and the bottom part, where the measurement base is located.
Figure 6.5 shows the measurement base installed on the bottom surface of the cryostat inner chamber.

In the Figure, we can see the measurement base where the sample is fixed through the two clamping elements at the two ends. On the upper surface of the base, the two Cernox^{TM} are fixed through two screws. Two additional aluminum 6N foils are

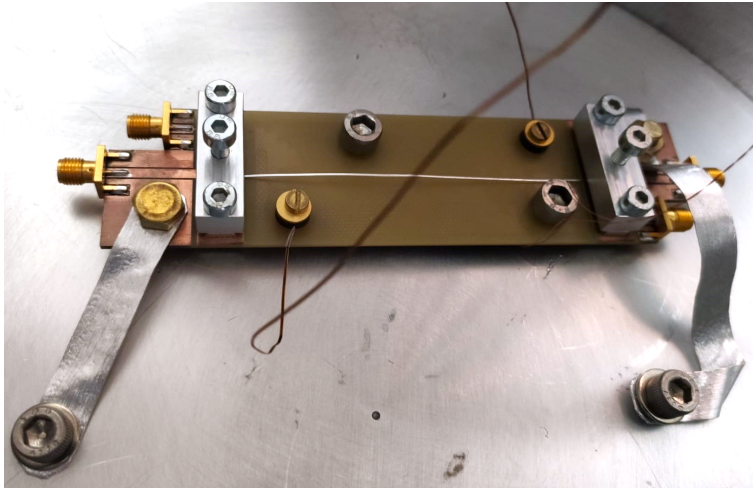**Figure 6.5.** Experimental base installed on the bottom surface of the cryostat's inner chamber. The aluminum 6N sample is fixed in the base and the two Cernox^{TM} thermometers are located on the upper surface. Two additional aluminum 6N foils are used to better thermalize the base's upper surface.

used to thermalize the copper on the upper surface of the PCB.

Heaters

Two different heaters are installed in the experimental setup: they are useful to perform resistance measurements at a temperature higher than the lowest possible reached by means of the PT.
The former heater is installed in the internal lateral surface of the cryostat's inner chamber. Its resistance is $109.7\,\Omega$. The latter is located on the bottom surface of the measurement base: it is formed by seven $13\,\Omega$ resistors welded together. Its resistance is $92.9\,\Omega$.

6.3   Preliminary measurement

A first measurement for the resistivity value has been attempted with the specimen and experimental setup described above. The cryostat has been cooled with a PT until the temperature of $\sim 15K$. Through the diode thermometer on the cover of the inner chamber and the two Cernox^{TM} on the experimental base, a little temperature gradient was found in the chamber: the experimental base reached a temperature of $(16.71 \pm 0.02)K$ [1] while the cover was at $(15.24 \pm 0.02)K$. During the cooling of the entire cryostat, several resistance measurements have been taken and an unwanted trend was found below 40K. The value of the resistance, indeed, starts to remain constant at the value of $255\mu\Omega$ in the temperature range of $40K$ to $\sim 16K$. In that range, the thermal conductivity value is expected to rise (see Woodcraft value 4.16)

---

[1]The uncertainties on the temperature values are the sum between the last readable digit in the instrumentation $0.01K$ and the calibration uncertainties found in [18].

and so the resistance is expected to descend. The possible causes for that trend can be found in:

- possible contact resistance;

- problems in the 4-wire technique.

The former problem can be simply explained by considering that the electrical current (usually $100mA$) is forced to pass through the sample whose width is $0,5mm$ and thickness of $100\mu m$: this may cause a residual resistance due to the small cross-sectional area.
We can describe the measurement with the equivalent circuit reported in Figure 6.6.
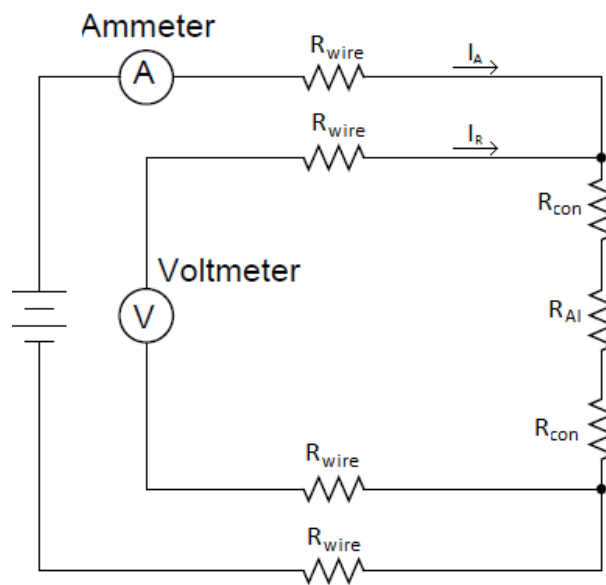
Figure 6.6. Equivalent sketch of the preliminary measurement: the voltmeter measures two additional contact resistances.

We can see from the Figure that the voltmeter measures two additional resistance contributions given by the small cross-sectional area. If we consider $I_A >> I_R$, the effective measure is:

$$\Delta V_{meas} = I_A(R_{Al} + 2R_{con}).\tag{6.8}$$

The latter problem is related to the 4-wire measurement technique. Although we designed two different paths for the current and the voltage reading (for both ends) in the experimental base, the actual electrical contact is only one for each side. It is, indeed, guaranteed by the little cube inside the upper-side clamping element which is pushed by a screw.

Both these problems can be solved by making little changes to the specimen and to the experimental base.

New specimen

A new specimen can be designed to reduce the first type of problem.
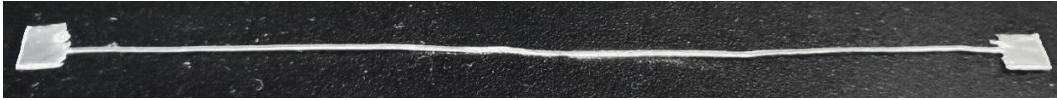
Figure 6.7. Modified specimen used for the measurement. The areas at the two ends are increased to overcome possible contact resistance.

We can see from Figure 6.7 the modified sample used for the measurements. The contact ends of the specimen have been enlarged to expand the cross-sectional area through which the current can pass. While the width of the sample remains $(0.5 \pm 0.01)mm$, the end areas become $(4.43 \pm 0.01)mm \times (4.43 \pm 0.01)mm$, a little bigger than the dimensions of the cube used for the clamping mechanism. The length of the new sample is $(97.01 \pm 0.01)mm$ (excluding the end areas) while its thickness is $100\mu m$.

New experimental base

The 4-wire technique can be improved by adding two new electrical contacts for the voltage reading. In Figure 6.8, we can see two new electrical contacts between the two clamping mechanisms: these have to be insulated from the other elements to guarantee an actual four-contacts measurement. The previous two voltage contacts can still be used to verify that the measurement with the new contacts differs from the one with the external voltage contacts.
The thermometers and heater attached to the base remain the same as those already described in the previous Sections.
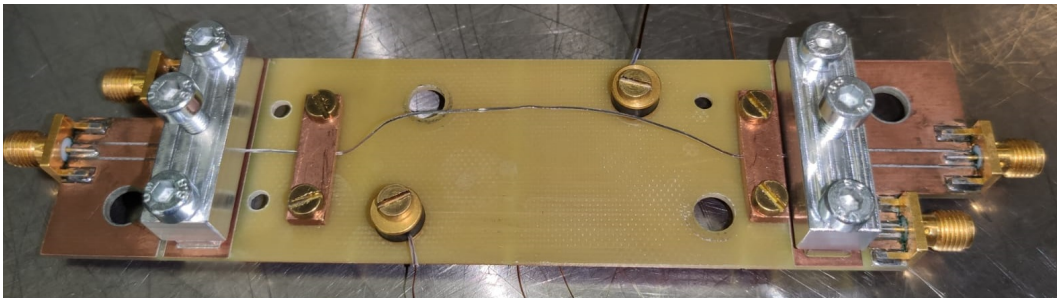
Figure 6.8. Modified experimental base used for the measurement. Two new electrical contacts have been added to separate the voltage reading from the current contacts. The new specimen can also be seen.

In this new setup, we can describe the measurement with the new equivalent circuit reported in Figure 6.9.
The previous contact resistances can be considered together with the ammeter's wire's resistances. The two new electrical contacts for the voltage reading add new
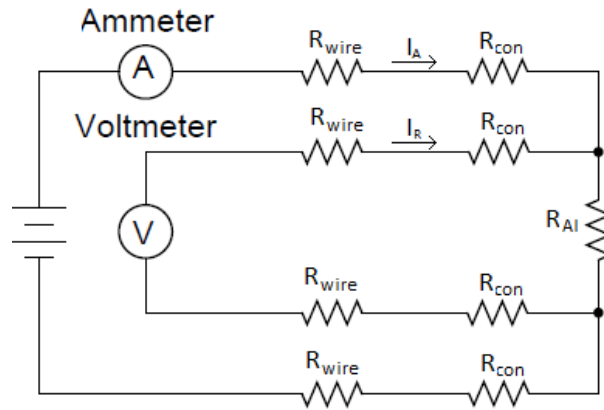
Figure 6.9. Equivalent sketch of the modified measurement: the voltmeter measures only the aluminum resistance.

contact resistances which, however, can be considered with the voltmeter's wire's resistance; hence, the effective measurement is:

$$\Delta V_{meas} = I_A R_{Al} \tag{6.9}$$

6.4 100 μm thickness results

The cryostat with the new experimental setup has been cooled down with a PT to a temperature of $(16.69 \pm 0.02)K$; a little temperature gradient inside the inner chamber of the cryostat can still be found through the upper cover thermometer which measures a temperature of $(15.19 \pm 0.02)K$. The external voltage measurement reports the same value of $255\mu\Omega$: this value can then be considered as an error that neither the enlargement of the end areas nor the changes in the thickness of the specimen can resolve. It can then be connected to other contact problems of the experimental base. The measurement through the new voltage contact, instead, shows the expected trend: the value of the measured resistance for both the temperature of $(295.77 \pm 0.05)K$ (initial temperature) and $(16.69 \pm 0.02)K$ (final temperature) are reported in Table 6.1[2].

Temperature [K]	Resistance [$m\Omega$]
295.77 ± 0.05	44.6905 ± 0.0447
16.69 ± 0.02	0.0313 ± 0.0004

Table 6.1. Resistance measurements of the $100\mu m$ thick specimen.

Since we can consider that the dimensions of the specimen remain the same at cryogenic temperature, we can use the value reported above to compute the RRR (see Equation 6.6):

---

[2]The uncertainties on the resistance values are obtained following [14] and [13].

$$RRR_{16.69} = \frac{\rho_{295.77K}}{\rho_{16.69K}} = \frac{R_{295.77K}}{R_{16.69K}} = 1427.8 \pm 18.4^3. \tag{6.10}$$

This value is lower than that reported by Yamada[35] but it is still acceptable because it's computed at $\sim 16K$. The RRR value presented by Yamada is at $4.2K$ and in that temperature range the conductivity, following Woodcraft's value (Figure 4.16), is expected to rise at least by half an order of magnitude with respect to $\sim 16K$. Therefore, considering the Wiedemann-Franz law, the resistivity is expected to drop by the same amount.

Measurements of electrical resistivity at different temperatures on the specimen have been performed by means of the heater described in the previous Sections. Resistivity values from $\sim 16K$ to $\sim 80K$ have been obtained by heating up the cryostat through the heaters (the values have been taken at the new equilibrium temperature); whilst from $\sim 80K$ to room temperature the values have been obtained during the free heating of the cryostat (after the PT was turned off). These last values, then, haven't been taken in an equilibrium temperature. The trend can be seen in Figure 6.10 while the values for each temperature can be found in Appendix A.
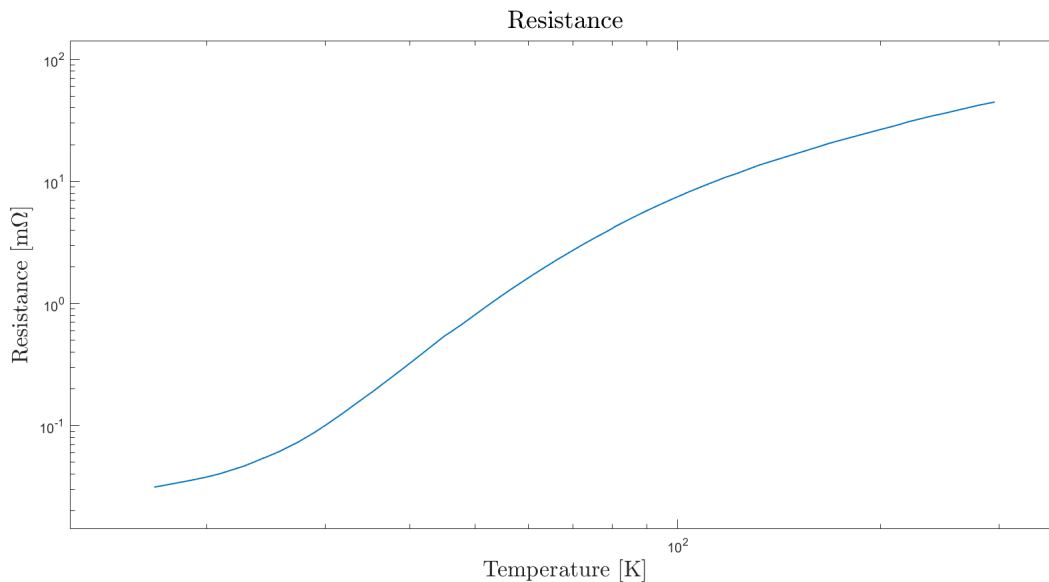
Figure 6.10. Resistance values at different temperatures for the $100\mu m$ thick sample.

We can extend the range of validity for the Wiedemann-Franz law from $T << \theta_D$ to the whole range of temperature ($\sim 16K$ to $\sim 295K$). In this way, we can obtain the trend and absolute values for the conductivity with respect to the temperature. In the computation, we have to consider the length of the specimen, this is different from the value reported above: the length of the sample for the resistivity (and conductivity) computation must be taken between the two new voltage contacts. The specimen is longer than the available length between the two clamping elements

---

[3]All the uncertainties on the derived quantities are obtained following the Equation $\sigma_{f(x_1,x_2,...,x_n)} = \sqrt{\sum_{i=1}^{n} \left(\frac{\partial f}{\partial x_i}\right)^2 \sigma_i^2}$.

in the experimental base, so, the sample must have a little curvature which can be seen in Figure 6.8. The estimated length is $(69.90 \pm 0.01)mm$. Following Equations 6.6 and 6.2, we can obtain the values for conductivity that are reported in Figure 6.11.
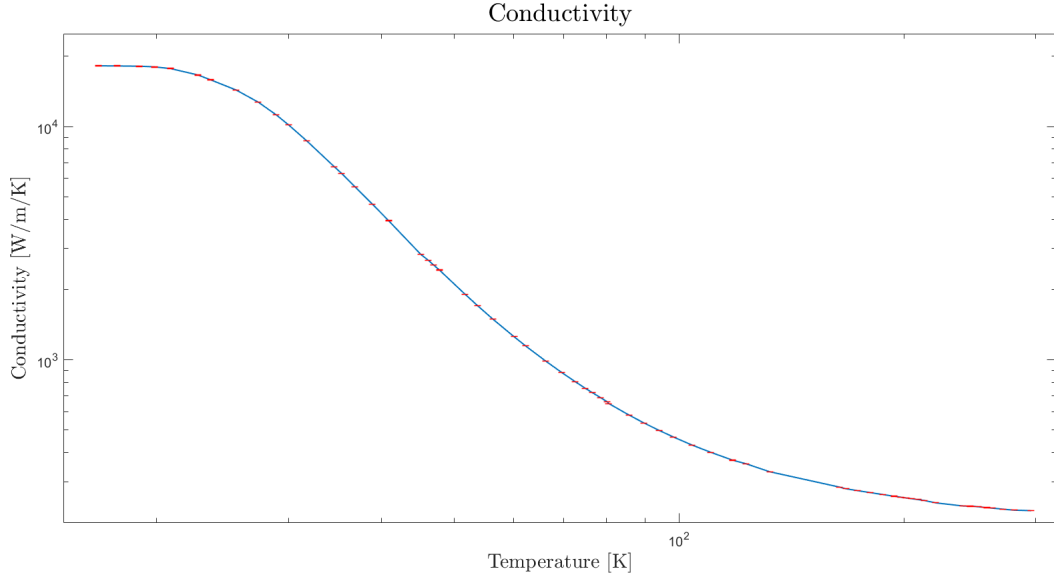
Figure 6.11. Conductivity values at different temperatures for the $100\mu m$ sample. The values are obtained by extending the validity range for the Wiedemann-Franz law.

Appendix A reports all the values used for the computation.
Since the Wiedemann-Franz law holds in the low temperature regime ($T << \theta_D$), we can just compare the value of conductivity obtained with the lowest temperature reached with the Woodcraft trend. Figure 6.12 shows the upper and lower limit curve for Al 6N conductivity value reported by Woodcraft (see complete reference graphic in Figure 4.16); the black circle represents the estimated value for conductivity for the $100\mu m$ thick sample. The value is within the expected range and it approaches the upper limit curve.

The result obtained doesn't take into account the thin films' correction; if we consider the free mean path reported by T.Yamada[35] ($\lambda_0 = 0.7mm$) and the size effect correction reported in Equation 6.5, we obtain:

$$\frac{\sigma}{\sigma_0} \sim 0.208(1 - \epsilon), \tag{6.11}$$

so the thermal conductivity for the bulk material is expected to rise by a factor ~ 5.
Anyway, we need further measurements to be able to use such value. Different thickness for the sample, in fact, must be measured to validate the trend given by Equation 6.5. The characterization of the bulk aluminum 6N must start, then, from new thickness measurements.
In the real application, heat links will be $50-100\mu m$ thick; hence, the value obtained in the measurement can be used in the simulations of the model. Anyway, the
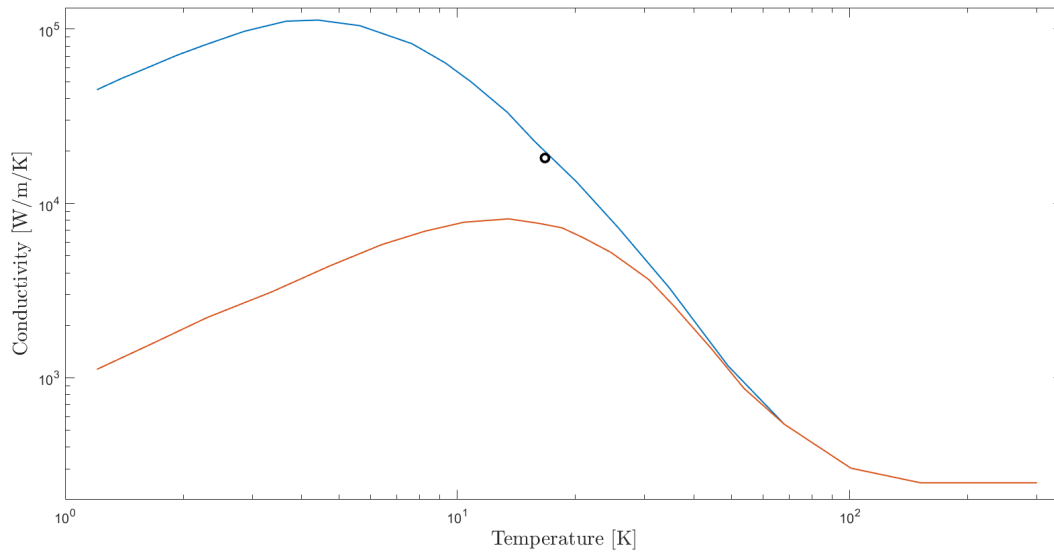
Figure 6.12. Upper and lower limit curve for conductivity value reported by A. Wood-craft [33]. The black circle represents the estimated value for the conductivity of the $100\mu m$ thick sample.

study of the size effect can be useful to understand the different effects on the two thickness. Among all the simulations performed in Chapter 5, we can consider that the ones performed with the upper limit curve for the conductivity values are the ones we have to take into account for the real application; in that situation, however, contact resistances will have crucial role in the effective thermal conductivity. Hence, a complete characterization of such type of resistances will be necessary.

Chapter 7

Conclusion

After the first detections of GWs, several upgrades have been implemented in present interferometers to increase the GWs' observation range. ET will be a third-generation GWs' observatory based on the combination of a room temperature Michelson interferometer and a cryogenic temperature one. The thesis focuses on the cryogenic interferometer, whose mirrors will be cooled to $10 - 15K$: PT cryocoolers can be used to provide the needed refrigeration power. Vibrations coming from the refrigeration cycles have to be reduced because they could inject vibrational noises affecting mirror position dynamics. PTs have, then, to be located away from the mirrors: a cooling line has to be designed to reduce the vibrations while efficiently transferring heat. Inspired by KAGRA, ET's cooling line will be designed with different parts connected together with heat links composed of three thin foil. Just upon such a base, we optimize the mechanics by adopting high purity soft links along the section of the cooling line. A first prototype of the whole cooling line, from the PTs to the cryostat, with such heat links will be soon tested in Amaldi Research Center, a laboratory located at Sapienza University, Rome. Only the soft heat links are still missing and motivated a part of this work.

Before the tests, thermal simulations can be performed on a simplified model to understand the asymptotic temperatures reachable with respect to the parameters chosen. The model used in the simulations can be resumed with an external vacuum chamber whose temperature would be $\sim 300K$, an internal heat path that will be connected to the mirror suspension system and a radiation shield, designed to reduce the incoming radiation from room temperature to the inner path. Two different typologies of simulations have been performed: the steady-state ones, which are useful to understand the equilibrium temperature of the facility and the transient ones, used to study the time dependence of the temperature gradient and the cooling time of the structure.

Starting from the steady-state ones, the thesis shows, first, the simulations performed on a test model where no super-insulation system has been considered. These simulations are useful to understand the relevance of parameters such as emissivity chosen for the surfaces and materials' thermal conductivities. The emissivity chosen for the simulations is $\epsilon = 0.15$ which is the expected typical emissivity for the materials but simulations with a value of $\epsilon = 0.25$ were performed too to study the worst-case scenario. Both the emissivities have been tested with different thermal

conductivity values obtained in the literature: a large range of values has been found, so the upper and lower limits of such a range can be checked through simulations. As expected, since no insulation system has been considered, the temperature of the radiation shield irradiated by the $300K$ vacuum chamber reached a value above $150K$ at the end of the cooling, supposed to be connected to a test chamber. However, the shield is effective: the inner heat path has a temperature variation on the furthest part of the model of less than 2%, for the upper limit case of the thermal conductivity, and less than 10% for the lower limit one. Without the radiation shield, a much higher temperature difference between the PTs' side and the furthest part would be expected.

The same parameter configurations have been tested considering a variation in the heat links number. As expected, the less the number of heat links is, the higher the temperature gradient. Simulations for the vibration contribution are, then, indispensable in this case to obtain a reasonable number of heat links that will be a good trade-off for both the vibrational and thermal points of view.

The simulated model has been, then, upgraded to consider a super-insulation system such as Mylar. It can be located on the external surfaces of the radiation shield to block further the radiation coming from the room temperature vacuum chamber. From different studies, a value of $\sim 2W/m^2$ (instead of $\sim 100W/m^2$) can be considered as the input power when ~ 50 layers of Mylar are inserted between the temperature of $300K$ and $40K$ (which is the expected equilibrium temperature for the radiation shield): this value can be converted, for the simulations, in an effective emissivity of $\epsilon_{eff} = 0.0043$ accounted for the external surfaces of the radiation shield. The same parameter configurations can be considered (emissivity of $\epsilon = 0.15$ and $\epsilon = 0.25$, upper and lower limit curves for thermal conductivities); Mylar allows the radiation shield to reach a lower temperature, that approaches the expected $40K$ for all the configurations, and the temperature difference on the furthest part of the model, with respect to the PTs location, reduces to $\sim 0.2\%$ for the upper limit case and to $\sim 2.5\%$ for the lower limit one.

Considering now the transient simulations, the thesis shows the results obtained by taking into account the variation with temperature of the PTs' refrigeration power, provided by the producer. The simulations performed considered the upper limit curve for conductivity; the worst-case scenario has been first tested (with an emissivity of $\epsilon = 0.25$ and without the super-insulation system), then the Mylar and $\epsilon = 0.15$ case has been simulated. Two additional models have been tested, one with a reduction of the inner heat links and the other with an increase in the outer connections. Transient simulations' results are reported in Table 5.12; an typical cooling time of $1.5 - 2$ days are needed to cool down the system. With the simulation performed with more heat links in the radiative shield, we realize that the shield's temperature and the cooling time are critically limited by the number of heat links; hence, a new model of the cooling line that allows the presence of more external heat links is required.

The last Chapter of the thesis shows the results of an indirect measurement of the thermal conductivity of Al 6N sample to be adopted by heat links. High purity materials have a high thermal conductivity in the low-temperature regime but they have a large range of possible values (see the upper and lower limit curve considered in the simulations) that depend upon the history of the material; hence, an estimation

of the thermal conductivity of the material used in the application is required to have a complete characterization of the model. We measure the Residual Resistivity Ratio (RRR) of the material; this resistivity can be used to derive the thermal conductivity value through the Wiedemann-Franz law (Equation 6.2) that holds in the low-temperature regime. The value obtained is $RRR_{16.69} = 1427.8 \pm 18.4$ where $16.69(K)$ represents the lowest temperature reached in the experimental setup. We can compare the estimated thermal conductivity (at $16.69K$) with the upper and lower limit curves used in the simulation (see Figure 6.12); the value obtained is within the range of the possible values and it approaches the upper limit curve. Hence, we can consider that the simulations performed with the upper limit curve are the ones we can use for the real application.

7.1 Future prospects and improvements of the results

Throughout the thesis, different hints can be found to improve some results and to extend the study of the whole model. We can briefly resume some of them.

7.1.1 Simulation cycles

Both the steady-state and the transient simulations are based on cycles and steps that can be improved. In the steady-state case, the starting equilibrium temperature of the PTs' bases can be obtained with higher accuracy by iterating more time the cycle described. In the transient simulations, instead, we can reach the asymptotic equilibrium temperature by reducing at every step the next time step. The real simulation time would increase by a large number but this will allow us to study the cooling of the model in the temperature regime where both the thermal conductivity and specific heat of the materials have their maximum slope (see Section 5.3).

7.1.2 Modification in the geometry

As explained in the thesis, we found two different problems in the geometry of the whole cooling line. First, we need to design a new additional shield. It will be used as support for the super-insulation system in the radiative shield's heat links' location while it efficiently blocks the radiation passing through the separations of the heat links. This will reduce the room temperature radiation contribution in the internal heat path. Second, we need to increase the possible number of radiative shield's heat links to allow the shield to cool down faster. In this way, the inner heat path will cool down faster too. The new configuration needs, then, to be tested with new steady-state and transient simulations.

7.1.3 Measurement of the capacity curve for the Pulse Tube

Transient simulations are based upon a capacity curve for the PTs obtained by rescaling another model's curve on the basis of the certified performance (see Section 5.3). To obtain better results, that can be considered as expectation value for the real tests, we need to measure the effective capacity curve for the PTs' model that will be used.

7.1.4   Measurement of the parameters

Simulations have a high number of free parameters such as emissivity, conductivity and specific heat. The measure presented in Chapter 6 is useful to reduce the free parameters for the choice of conductivity for the heat links: since the value approaches the upper limit curve, we can consider for next simulations that value for conductivity. The same can be done by measuring all the possible parameters' values for the other components of the model: this allows us to reduce the free parameters in the simulations obtaining, in this way, a result that can approach the performance of the real system.

7.1.5   Characterization of the size effect and mechanical contacts

Chapter 6 introduces the concept of the size effect that modifies the electrical conductivity of a thin specimen with respect to the bulk one. In the real prototype of the cooling line, there will be heat links formed by three foils of Al 6N whose thickness will be $50 - 100 \mu m$. Hence, the size effect will be relevant for both the thickness and will have a different contribution for the two. Other measures performed with the same experimental setup on different thickness samples are then required to study both the trend of the size effect with respect to the thickness and the mean free path of the conduction electrons. A lower temperature measurement would, also, be useful to better characterize the expected thermal conductivity. We expect to dedicate a significant effort to diminish the thermal resistance at the mechanical interfaces. We already experienced its relevance during the RRR measurements (see Section 6.3).

7.1.6   Design of the payload and cryostat

At last, we have to mention the relevance of the design of the payload and cryostat. The Amaldi Research Center laboratory will host a first prototype of cryostat, designed to cool down a 1:1 payload prototype. When the design of both structures will be completed, we will extend the cooling line thermal simulation modeling in order to consider the whole system.

Appendix A

100 μm thickness results

Length [mm]	Cross-sectional area [mm^2]
69.90 ± 0.01	0.05

Table A.1. Dimension of the $100\mu m$ thick specimen.

T_{mean} [K]	R [$m\Omega$]	ρ [Ωm] $\times 10^{-11}$	κ [$W/m/K$]	RRR
16.69±0.02	0.03±4.02E-04	2.24±0.03	18216.25±234.80	1427.812±18.387
17.70±0.02	0.03±4.02E-04	2.37±0.03	18180.65±221.04	1346.099±16.356
18.94±0.02	0.04±4.02E-04	2.55±0.03	18143.13±205.85	1255.351±14.241
19.87±0.02	0.04±4.03E-04	2.69±0.03	18021.78±193.71	1188.577±12.779
20.88±0.02	0.04±4.03E-04	2.88±0.03	17713.22±178.24	1111.704±11.195
22.69±0.02	0.05±4.04E-04	3.33±0.03	16644.80±145.17	961.086±8.398
23.59±0.02	0.05±4.04E-04	3.63±0.03	15871.46±127.20	881.469±7.083
25.55±0.02	0.06±4.06E-04	4.35±0.03	14334.56±96.29	735.041±4.961
27.34±0.02	0.07±4.08E-04	5.24±0.03	12723.06±71.47	609.693±3.449
28.89±0.02	0.09±4.11E-04	6.27±0.03	11234.91±53.28	509.584±2.443
30.00±0.02	0.10±4.14E-04	7.19±0.03	10182.45±42.56	444.682±1.887
31.74±0.02	0.12±4.21E-04	8.91±0.03	8689.32±29.92	358.672±1.265
34.55±0.02	0.18±4.40E-04	12.53±0.03	6730.68±17.38	255.228±0.690
35.35±0.02	0.19±4.47E-04	13.70±0.03	6296.77±15.15	233.371±0.593
36.82±0.02	0.23±4.64E-04	16.26±0.03	5524.87±11.70	196.615±0.447
38.86±0.02	0.28±4.96E-04	20.37±0.04	4653.76±8.47	156.919±0.315
40.85±0.02	0.35±5.39E-04	25.21±0.04	3952.54±6.37	126.782±0.232
45.13±0.02	0.54±6.82E-04	38.93±0.05	2828.81±3.85	82.121±0.132
46.19±0.02	0.59±7.20E-04	42.22±0.05	2669.31±3.54	75.721±0.119
46.91±0.02	0.63±7.51E-04	44.83±0.05	2553.31±3.32	71.311±0.111
47.77±0.02	0.67±7.89E-04	48.01±0.06	2427.73±3.10	66.583±0.103
51.72±0.02	0.92±1.01E-03	66.06±0.07	1910.19±2.28	48.393±0.072
53.78±0.02	1.08±1.16E-03	77.00±0.08	1703.98±1.99	41.515±0.061
56.36±0.02	1.29±1.36E-03	92.13±0.10	1492.63±1.70	34.698±0.050
60.13±0.02	1.63±1.69E-03	116.70±0.12	1257.09±1.40	27.392±0.039
62.27±0.03	1.85±1.90E-03	132.18±0.14	1149.47±1.29	24.184±0.035

66.28±0.03	2.29±2.33E-03	163.63±0.17	988.29±1.09	19.537±0.028
69.71±0.03	2.70±2.74E-03	193.01±0.20	881.19±0.96	16.562±0.024
72.62±0.03	3.08±3.11E-03	219.96±0.22	805.55±0.87	14.533±0.021
74.89±0.03	3.38±3.42E-03	241.86±0.25	755.48±0.81	13.217±0.019
76.49±0.03	3.60±3.63E-03	257.68±0.26	724.26±0.78	12.406±0.018
78.46±0.03	3.88±3.91E-03	277.55±0.28	689.71±0.74	11.518±0.016
80.17±0.03	4.14±4.17E-03	296.30±0.30	660.15±0.71	10.789±0.015
80.48±0.03	4.22±4.25E-03	302.06±0.31	650.11±0.69	10.583±0.015
85.71±0.03	5.04±5.07E-03	360.59±0.37	579.94±0.61	8.865±0.013
89.66±0.03	5.69±5.72E-03	407.32±0.41	537.10±0.57	7.848±0.011
93.99±0.03	6.43±6.45E-03	459.82±0.47	498.72±0.52	6.952±0.010
98.23±0.03	7.17±7.19E-03	512.81±0.52	467.36±0.49	6.234±0.009
103.93±0.03	8.21±8.23E-03	587.01±0.59	431.98±0.45	5.446±0.008
110.26±0.03	9.37±9.39E-03	670.03±0.68	401.51±0.42	4.771±0.007
117.94±0.03	10.83±1.09E-02	774.71±0.78	371.46±0.39	4.126±0.006
122.75±0.03	11.66±1.17E-02	834.09±0.84	359.09±0.37	3.833±0.005
132.24±0.03	13.61±1.36E-02	973.48±0.99	331.46±0.34	3.284±0.005
164.00±0.03	19.64±1.97E-02	1405.20±1.42	284.76±0.29	2.275±0.003
167.11±0.03	20.33±2.04E-02	1454.57±1.47	280.31±0.29	2.198±0.003
173.30±0.03	21.49±2.15E-02	1537.24±1.55	275.06±0.28	2.080±0.003
180.17±0.03	22.78±2.28E-02	1629.38±1.65	269.80±0.28	1.962±0.003
187.37±0.03	24.15±2.42E-02	1727.33±1.75	264.68±0.27	1.851±0.003
193.91±0.03	25.41±2.54E-02	1817.92±1.84	260.26±0.27	1.758±0.002
197.80±0.03	26.15±2.62E-02	1870.77±1.89	257.98±0.26	1.709±0.002
201.18±0.03	26.81±2.68E-02	1917.79±1.94	255.95±0.26	1.667±0.002
204.66±0.03	27.48±2.75E-02	1965.45±1.99	254.07±0.26	1.626±0.002
208.65±0.03	28.25±2.83E-02	2021.01±2.04	251.91±0.26	1.582±0.002
212.79±0.04	29.07±2.91E-02	2079.39±2.10	249.69±0.26	1.537±0.002
220.32±0.04	30.81±3.08E-02	2204.10±2.23	243.89±0.25	1.450±0.002
239.48±0.04	34.53±3.46E-02	2470.16±2.50	236.56±0.24	1.294±0.002
241.42±0.04	34.84±3.49E-02	2491.90±2.52	236.39±0.24	1.283±0.002
245.02±0.04	35.44±3.55E-02	2535.03±2.56	235.84±0.24	1.261±0.002
247.85±0.04	35.89±3.59E-02	2566.94±2.60	235.59±0.24	1.245±0.002
251.45±0.04	36.57±3.66E-02	2615.92±2.65	234.54±0.24	1.222±0.002
256.07±0.04	37.45±3.75E-02	2678.88±2.71	233.23±0.24	1.193±0.002
258.07±0.04	37.83±3.79E-02	2705.67±2.74	232.73±0.24	1.181±0.002
262.30±0.04	38.65±3.87E-02	2764.83±2.80	231.48±0.24	1.156±0.002
271.44±0.04	40.41±4.05E-02	2890.74±2.92	229.12±0.23	1.106±0.002
280.76±0.05	42.21±4.22E-02	3019.16±3.05	226.90±0.23	1.059±0.001
295.77±0.05	44.69±4.47E-02	3196.75±3.23	225.75±0.23	1.000±0.001

Table A.2. Value for average temperature on the experimental base (T_{mean}) with an uncertainty that varies following the calibration in [18]; resistance with uncertainty that varies following [13] and [14]; resistivity, conductivity and RRR for the 100μm thickness measurement.

Acronyms

5N 99.999% purity.

5N5 99.9995% purity.

6N 99.9999% purity.

AdV Advanced Virgo.

Al aluminum.

aLIGO Advanced LIGO.

BH Black Hole.

BS Beam Splitter.

CE Cosmic Explorer.

Cu copper.

DE Dark Energy.

DECIGO DECi-Hertz Interferometer Gravitational-wave Observatory.

DM Dark Matter.

EMF ElectroMotive Force.

EPTA European Pulsar Timing Array.

ET Einstein Telescope.

ET-HF ET High Frequency.

ET-LF ET Low Frequency.

ETM End Test Mass.

FEA Finite Element Analysis.

FEM Finite Element Method.

FP Fabry-Pérot.

GW Gravitational Wave.

GWB Gravitational Wave Background.

IPTA International Pulsar Timing Array.

ITM Input Test Mass.

KAGRA Kamioka Gravitational Wave Detector.

LIGO Laser Interferometry Gravitational-Wave Detector.

LISA Laser Interferometer Space Antenna.

NS Neutron Star.

O1 First Observing Run.

O2 Second Observing Run.

O3 Third Observing Run.

O4 Fourth Observing Run.

O5 Fifth Observing Run.

PCB Printed Circuit Board.

PDE Partial Differential Equation.

PSD Power Spectral Density.

PT Pulse Tube.

PTA Pulse Timing Array.

QNM Quasi-Normal Mode.

RRR Residual Resistivity Ratio.

SKA Square Kilometer Array.

Ti Titanium.

TT Transverse-Traceless.

V Vanadium.

Bibliography

[1] B. P. ABBOTT ET AL., *Prospects for observing and localizing gravitational-wave transients with advanced LIGO, advanced virgo and KAGRA*, Living Reviews in Relativity, 23 (2020).

[2] T. AKUTSU ET AL., *Overview of KAGRA: Detector design and construction history*, Progress of Theoretical and Experimental Physics, 2021 (2020). 05A101.

[3] D. BERSANETTI ET AL., *Advanced virgo: Status of the detector, latest results and future prospects*, Universe, 7 (2021).

[4] P. E. BRADLEY AND R. RADEBAUGH, *Properties of Selected Materials at Cryogenic Temperatures*, CRC Press, Boca Raton, FL, 2013-06-17 2013.

[5] R. H. COLE, C. J. MOORE, AND C. P. L. BERRY, *Gravitational wave detectors and sources*. `http://gwplotter.com`.

[6] A. DE WAELE, *Basic operation of cryocoolers and related thermal machines*, Journal of Low Temperature Physics, 164 (2011), pp. 179–236.

[7] R. B. DINGLE, *The electrical conductivity of thin wires*, Proceedings of the Royal Society of London. Series A, Mathematical and Physical Sciences, 201 (1950), pp. 545–560.

[8] S. R. DOMEN, *Emissivity of aluminized mylar*, International Journal of Radiation Applications and Instrumentation. Part C. Radiation Physics and Chemistry, 37 (1991), pp. 199–201.

[9] ET STEERING COMMITTEE, *ET Design report update 2020*. `https://apps.et-gw.eu/tds/?content=3&r=17245`.

[10] V. FERRARI, L. GUALTIERI, AND P. PANI, *General Relativity and its Applications: Black Holes Compact Stars and Gravitational Waves*, Boca Raton: CRC Press, 1 ed., 2021.

[11] K. FUCHS, *The conductivity of thin metallic films according to the electron theory of metals*, Mathematical Proceedings of the Cambridge Philosophical Society, 34 (1938), p. 100–108.

[12] M. GREEN ET AL., *Second stage cooling from a cryomech pt415 cooler at second stage temperatures up to 300 K with cooling on the first-stage from 0 to 250 W*, IOP Conference Series: Materials Science and Engineering, 101 (2015), p. 012002.

[13] KEITHLEY INC., *Model 2182 and 2182A Nanovolt-meter Data Sheet.* https://www.tek.com/en/products/keithley/low-level-sensitive-and-specialty-instruments/nanovoltmeter-model-2182a.

[14] KEITHLEY INC., *Model 6221 AC and DC Current Source Data Sheet.* https://www.tek.com/en/products/keithley/low-level-sensitive-and-specialty-instruments/series-6200.

[15] KEITHLEY INC., *Model 2182 and 2182A Nanovoltmeter User's Manual*, Keithely Instrument, 1 ed., 2004.

[16] KEITHLEY INC., *Model 6221 AC and DC Current Source Reference Manual*, Keithely Instrument, 2 ed., 2005.

[17] T. R. KUPHALDT, *Lessons In Electric Circuits*, vol. I - DC, 2006.

[18] LAKE SHORE CRYOTRONICS INC., *Cernox RTDs.* https://www.lakeshore.com/products/categories/specification/temperature-products/cryogenic-temperature-sensors/cernox.

[19] LIGO, *Sources and types of gravitational waves.* https://www.ligo.caltech.edu/page/gw-sources.

[20] C. J. MOORE, R. H. COLE, AND C. P. L. BERRY, *Gravitational-wave sensitivity curves*, Classical and Quantum Gravity, 32 (2014), p. 015014.

[21] I. NAKAMICHI AND T. KINO, *Deviations from matthiessen's rule on the surface scattering in aluminum*, Journal of the Physical Society of Japan, 49 (1980), pp. 1350–1357.

[22] G. F. NATERER, *Advanced Heat Transfer*, Boca Raton: CRC Press, 2 ed., 2018.

[23] M. PITKIN ET AL., *Gravitational wave detection by interferometry (ground and space)*, Living Reviews in Relativity, 14 (2011).

[24] F. RICCI AND M. BASSAN, *Experimental Gravitation*, Springer Cham, 1 ed., 2022.

[25] K. RILES, *Gravitational waves: Sources, detectors and searches*, Progress in Particle and Nuclear Physics, 68 (2013), pp. 1–54.

[26] R. G. ROSS, *Quantifying mli thermal conduction in cryogenic applications from experimental data*, IOP Conference Series: Materials Science and Engineering, 101 (2015), p. 012017.

[27] Y. SAKAKIBARA, *A study of cryogenic techniques for gravitational wave detection*, PhD thesis, Department of Physics, University of Tokyo, 2014.

[28] E. SONDHEIMER, *The mean free path of electrons in metals*, Advances in Physics, 1 (1952), pp. 1–42.

[29] M. K. Thompson and J. M. Thompson, *ANSYS mechanical APDL for finite element analysis*, Butterworth-Heinemann, 1 ed., 2017.

[30] T. Tomaru et al., *Thermal lensing in cryogenic sapphire substrates*, Classical and Quantum Gravity, 19 (2002), pp. 2045–2049.

[31] G. Ventura and L. Risegari, *The Art of Cryogenics*, Elsevier, 1 ed., 2008.

[32] A. L. Woodcraft, *Predicting the thermal conductivity of aluminium alloys in the cryogenic to room temperature range*, Cryogenics, 45 (2005), pp. 421–431.

[33] A. L. Woodcraft, *Recommended values for the thermal conductivity of aluminium of different purities in the cryogenic to room temperature range, and a comparison with copper*, Cryogenics, 45 (2005), pp. 626–636.

[34] T. Yamada, *Low-Vibration conductive cooling of KAGRA cryogenic mirror suspension*, PhD thesis, Department of Physics, University of Tokyo, 2020.

[35] T. Yamada et al., *High performance thermal link with small spring constant for cryogenic applications*, Cryogenics, 116 (2021), p. 103280.